DEVELOPING HIGH-PERFORMANCE GeTe AND SnTe-BASED THERMOELECTRIC MATERIALS

DEVELOPING HIGH-PERFORMANCE GeTe AND SnTe-BASED THERMOELECTRIC MATERIALS

By

Zan Yang, B.Eng.

A Thesis Submitted to the School of Graduate Studies in Partial Fulfillment of the Requirements for the Degree Master of Science

MASTER OF SCIENCE (2022) McMaster University

Hamilton, Ontario (Chemistry)

TITTLE: Developing High-performance GeTe and SnTe-based Thermoelectric Materials

AUTHOR: Zan Yang, B.Eng. (McMaster University)

SUPERVISOR: Dr. Yurij Mozharivskyj

NUMBER OF PAGES: xix, 133

Lay Abstract

Thermoelectric materials can generate energy from temperature gradient, making them potential solutions for the escalating energy crisis. The state-of-the-art thermoelectric material is PbTe which shows outstanding performance and high stability. However, the toxicity of Pb element limits its practical application.

It is the purpose of this work to develop high-performance GeTe and SnTe-based thermoelectrics to reduce the usage of PbTe. Combining theoretical calculations and experimental characterizations, detailed investigation on the transport properties, crystal structure and microstructure were performed on both GeTe and SnTe. Relations between their thermoelectric properties and their composition, synthesis method and microstructure were revealed. This work paves the path for the development of environmentally friendly and high-performance thermoelectric systems.

Abstract

This dissertation covers the study of the thermoelectric properties of GeTe and SnTe. The goal of this research is to develop high-performance lead-free thermoelectric materials that can replace PbTe-based systems so that thermoelectric technology could be bring into real application. During the study, extensive investigations on the electrical and thermal transport behaviors were conducted both experimentally and theoretically.

In **Chapter 1 ~ 3**, the origin of thermoelectricity, modelling and characterization methods are discussed in detail. In **Chapter 4**, study on the thermoelectric properties of Bi, Zn and In co-doped GeTe was presented. Initial doping with Bi enhanced the performance by tuning the electronic properties and bringing down the thermal conductivity. Subsequent Zn doping permitted to maintain the high power factor by increasing carrier mobility and reducing carrier concentration. Subsequent In doping boosted the density of state effective mass. A peak zT value of 2.06 and an average zT value of 1.30 have been achieved in $(Ge_{0.97}Zn_{0.02}In_{0.01}Te)_{0.97}(Bi_2Te_3)_{0.03}$. In **Chapter 5**, we thoroughly investigated the transport properties of SnTe-Sb_2Te_3 alloying system, provided useful insight of the mechanism of the enhanced Seebeck coefficient. To also overcome the poor carrier mobility, Pb compensation was performed which effectively optimized the carrier mobility. Meanwhile, Pb compensation broke the charge balance, allowing Sb to precipitate out of the structure. These second-phase particles provided additional source of phonon scattering, effectively suppressing the lattice thermal conductivity. As a result, a peak zT of 1.1 at 778K and an average zT of 0.56 from 300K to 778K was achieved in

$(Sn_{0.98}Ge_{0.05}Te)_{0.91}$ $(Sb_2Pb_{0.5}Te)_{0.09}$, which is one of the best SnTe-based thermoelectric systems.

Acknowledgements

This project would not have been possible without the support of many people. I would like to thank my supervisor Dr. Yurij Mozharivskyj, who generously shared his knowledge and in-depth insight in the field of scientific research. I would also like to thank my committee members Dr. John Greedan and Dr. Oleg Rubel for pointing out my short comes and the flaws of my research. I am grateful to the support from Dr. Yu-Chih Tseng, Dr. Kuei-Hsien Chen, Dr. Jan Kycia and Dr. Eric Toberer for allowing me to get access to their essential instruments. I would also like to express my thanks to the members in the CCEM: Hui Yuan, Jhoynner Martinez and Christopher Butcher, their professionalism in material characterization are admirable.

Many thanks to my friends and colleagues: Evan Smith, Yuyang Huang, Sergei Novikov, Kamil Ciesielski, Sunessh Meledath Valiyaveettil and Tianze Zou for contributing to the current work. My special thanks to Evan, who sacrificed his personal time to help me develop python codes for the theoretical simulations.

Last but not the least, I am thankful to my family members, my parents, my sister and my aunts, who supported me spiritually. My achievements would not have been possible without their support.

Table of Contents

List of Figures

List of all Tables

List of all Abbreviations and Symbols

Symbol	Description
E	Energy level
$F(E)$	Electron flow
μ	Chemical potential
T	Temperature
V	Voltage
$f(E)$	Fermi-Drac distribution
$N(E)$	Total number of electrons
$\tau(E)$	Relaxation time
I	Current
$D^*(E)$	Effective density of states
$\gamma(E)$	Energy broadening caused by electron scattering
q	Electron charge
h	Plank's constant
$\hbar$	Reduced Plank's constant
n_s	Area charge density
W	Width of 2D sheet
L	Length of 2D sheet
$\langle v_x^+(E)\rangle$	Average electron group velocity along the positive x direction
$M(E)$	Number of conduction channels
$\lambda_B(E)$	De Broglie wavelength
$M_{1D}(E)$	1D number of conduction channels
$M_{2D}(E)$	2D number of conduction channels
$M_{3D}(E)$	3D number of conduction channels
$M_C(E)$	Conduction band number of conduction channels
$M_V(E)$	Valence band number of conduction channels
$D_{1D}(E)$	1D density of states
$D_{2D}(E)$	2D density of states
$D_{3D}(E)$	3D density of states
m^*	Effective mass
$T(E)$	Transmission term
$\lambda(E)$	Mean free path of electron
k_B	Boltzmann constant
G_E	Electric conductance
G_S	Seebeck effect conductance

ΔT	Temperature gradient
A	Cross-section
σ	Conductivity
ρ	Resistivity
$\sigma'(E)$	Derivative conductivity
I_Q	Heat current induced by carrier transport
G_{P}	Peltier thermal conductance
R	Resistance
S	Seebeck coefficient
π	Peltier coefficient
K_e	Electric thermal conductance
K_0	Short circuit thermal conductance
L	Lorenz number
κ_e	Electric thermal conductivity
$B(E)$	Bose-Einstein distribution
Q	Heat current
ω	Phonon frequency
$T_{\mathrm{ph}}(\hbar\omega)$	Transmission term of phonon
$M_{\mathrm{ph}}(\hbar\omega)$	Number of conductance channels of phonon
$\lambda_{\mathrm{ph}}(\hbar\omega)$	Mean free path of phonon
K_{L}	Lattice thermal conductance
κ_{L}	Lattice thermal conductivity
r	Internal resistance
T_h	Hot side temperature
T_c	Cold side temperature
P	Output power of a thermoelectric device
R_{L}	Load resistance
Q_{in}	Injected thermal flux
η	Efficiency of thermoelectric device
m	Ratio between load resistance and internal resistance
Z	Figure of merit
$U^{ion}(\vec{r})$	Periodic potential provided by the lattice
$\rho(\vec{r})$	Electron density
$\psi_i(\vec{r})$	Eigenfunctions of Schrödinger equation
$\psi_i^*(\vec{r})$	Complex conjugate
$\vec{r}$	Spatial vector
ε_i	Eigenstates of Schrödinger equation

$U^{el}(\vec{r})$	Hartree potential
Ψ	Wave function
$\hat{s}_i$	Spin operator
$U^{ex}(\vec{r})$	Exchanging energy
$U^{ex}_{\mathrm{IEG}}(\vec{r})$	Exchanging energy ideal electron gas
$U^{c}_{\mathrm{IEG}}(\vec{r})$	Correlation energy of ideal electron gas
$U^{ex}_{\mathrm{LDA}}(\vec{r})$	Exchanging energy of localized density approximation
$U^{xc}_{\mathrm{GGA}}(\vec{r})$	Exchanging-correlation energy of generalized gradient approximation
Ω_{BZ}	Volume of the first Brillouin zone
$f_{i\vec{k}}$	Occupation factor
$\vec{k}$	Wave number
E_{total}	Total energy
$[\vec{R}]$	A set of nuclei coordinates
$\psi(\vec{r})$	Electron part of the wavefunction
$\chi(\vec{R})$	Nuclei part of the wavefunction
E_R	Total energy under certain nuclei coordinate set
ψ_R	Electron part of the wavefunction under certain nuclei coordinate set
ε_R	Energy eigenvalues under certain nuclei coordinate set
U	Total potential energy of the system
$\widehat{H}_N$	Nuclei Hamiltonian
M_I	Nuclei mass
Z_I	Nuclei charge
$\vec{R}_I$	Nuclei spatial vector
P_I	Nuclei momentum
t	Time
$\vec{F}_I$	Force applied onto nuclei
ξ	Reduced Fermi level
ε	Reduced energy
F_s	Parabolic band Fermi-Dirac Integral
s	Integration constant for parabolic band
${}^{n}F_k^m$	Kane band Fermi-Dirac Integral
n, m, k	Integration constant for Kane band
n	Carrier concentration
A_H	Hall coefficient
m^*_{d}	Density of states effective mass
m^*_{b}	Single band effective mass

N_V	Band degeneracy
α	Non-parabolicity
E_g	Band gap
ΔE	Energy offset between principal and lower energy band
$\vec{v}_D$	Debye velocity
ω_D	Debye frequency
N	Number of atoms per unit cell
Ω	Volume of the unit cell
T_D	Debye temperature
x	Reduced energy of phonon
τ_{total}	Total relaxation time of phonon
τ_U	Umklapp relaxation time
τ_N	Normal process relaxation time
τ_B	Grain boundary scattering relaxation time
τ_{PD}	Point defect scattering relaxation time
τ_P	Precipitation relaxation time
τ_{SF}	Stacking fault relaxation time
$\Delta\rho$	Density difference between matrix and secondary phase particle
v_s	Bulk sound velocity
v_l	Longitudinal sound velocity
v_t	Transverse sound velocity
v_p	Poisson ratio
γ	Grüneisen parameter
Γ	Structure contrast parameter
Γ_M	Mass contrast
Γ_S	Size contrast
$\bar{\bar{M}}$	Average atomic mass
$\bar{r_i}$	Average size
$\bar{\bar{r}}$	Average atomic mass
m_j^i	Atomic mass of the j^{th} atom
r_j^i	Atomic size of the j^{th} atom
$\vec{a}_1, \vec{a}_2, \vec{a}_3$	Unit cell vectors
$\hat{n}, \hat{n}'$	Unit vector of the incident and scattered X-ray
d	Interplanar distance
λ	X-ray wavelength
$\vec{G}$	Reciprocal vector
$\vec{b}_1, \vec{b}_2, \vec{b}_3$	Reciprocal cell vectors

θ	Diffraction angle
ρ_{G}	Electron distribution function in the reciprocal space
S_{G}	Structure factor
h, k, l	Miller indexes
F_{hkl}	Scattering intensity of the plan (hkl)
$\hat{g}$	Reciprocal operator
$\hat{r}$	Rotational matrix
φ	Aperture of the incident beam
K_{β}, $\mathrm{K}_{\alpha 1}$, $\mathrm{K}_{\alpha 2}$	Characteristic X-ray series
S_{sample}	Sample Seebeck coefficient
S_{wire}	Wire Seebeck coefficient
$\vec{p}(t)$	Electron momentum
$\vec{B}$	Magnetic field
$\vec{E}$	Electric field
E_x	Electric field along x direction in Hall geometry
E_y	Electric field along y direction in Hall geometry
p_x	Electron momentum along x direction in Hall geometry
p_y	Electron momentum along y direction in Hall geometry
R_{H}	Hall coefficient
μ_{H}	Hall mobility
$\vec{J}$	Current density
t	Sheet thickness
D	Thermal diffusivity
C_{P}	Constant pressure heat capacity
NCB	Non-charge balanced
CB	Charge balanced
$\mathrm{Ge}_{\mathrm{Ge}}^{\times}$	A Ge atom on the Ge site with no extra charges
$\mathrm{Bi}_{\mathrm{Ge}}^{\prime}$	A Bi atom on the Ge site with a charge of -1
$\mathrm{V}_{\mathrm{Ge}}^{\cdot\cdot}$	A Ge vacancy with a charge of +2
μ_{W}	Weighted mobility
CP	Pb compensation process where a vacancy is being filled by Pb element
SP	Pb substitution process where Pb substitute one Sb on the cation site
r	Scattering factor
$\mathrm{V}_{\mathrm{Sn}}^{\cdot\cdot}$	A Sn vacancy with 2 positive charges
$\mathrm{Sb}_{\mathrm{Sn}}^{\prime}$	A Sb atom on the Sn site with one negative charge

Chapter 1: Thermoelectricity

1.1 Introduction

In 1821, German Physicist Johann Seebeck (Tallin, April 9, 1770 - Berlin, December 10, 1831) observed that a compass magnetic needle was deflected by a closed circuit made of two dissimilar metals (today known as thermocouple) whose junctions were at different temperatures, and the deflection angle was related to the temperature difference between the two junctions. The theory behind this phenomenon was latter established by the scientific community and named as ***Seebeck effect***[1]. The reverse effect was observed in 1834 by a French physicist Jean Charles Athanase Peltier (Ham, February 22, 1785– Paris, October 27, 1845). He discovered that, depending on the direction of the passing current, the junction between two dissimilar metals can be heated or cooled. This observation was then explained by the Russian physicist Heinrich Friedrich Emil Lenz (Dorpat, February 12, 1804 - Rome, February 10, 1865) in the same year. Today, this physical effect is known as ***Peltier effect***[2]. Eventually, after 20 years, British mathematical physicist and engineer William Thomson (Belfast, June 26, 1824 – Largs, December 17, 1907) provided a comprehensive thermodynamic interpretation, which explained both Seebeck effect and Peltier effect under one theoretical framework. Thomson also observed that when a current flows through an unequal heated conductor, heat was released or absorbed along the length of the conductor, depending on the direction of current flow, and this phenomenon is known as ***Thomson effect***[3]. These findings form the cornerstone of the theory of thermoelectricity.

Nowadays, with the ever-increasing demand for energy in human society, the resulting environmental problem is escalating globally. Therefore, there is an urgent need to develop energy harvesting technology to increase the total energy conversion efficiency during daily production and transportation. In various human activities, waste heat is the main form of energy loss. In this light, researchers from different fields are working together to develop advanced thermoelectric energy harvesters (TEH) to harvest energy from various heat sources in our daily life, such as human body and car exhaust, etc. The development of modern quantum mechanics provided many new insights regarding transport properties. In this chapter, electron and phonon transport model will be derived via Landauer's approach. Then, the working principle, device structure and performance criteria of TEH will be introduced.

1.2 Landauer's Approach for Near-Equilibrium Transport

1.2.1 Electron Transport

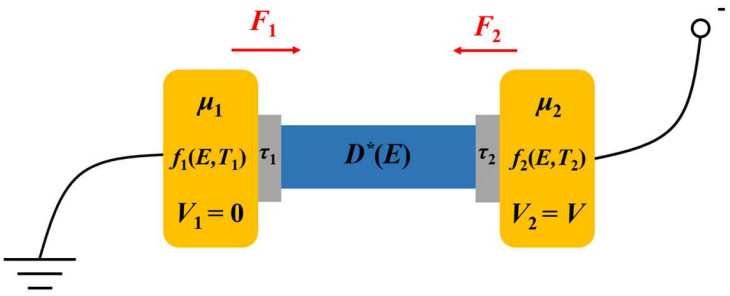

Figure 1.1 Configuration of a simplified semiconductor device.

Figure 1.1 shows a simplified device structure, consisting of contacts 1 and 2 and a uniform conductor between the two contacts. A voltage of V applied to this device induces an electric current flowing from contact 2 to contact 1. To simplify the mathematical model, the following assumptions are made[4]:

1) The band structure of the device is known.
2) The inelastic scattering only happens at two contacts and the scattering is strong enough to always maintain thermal equilibrium.
3) The electron-electron interaction is ignored.
4) Electrons flow within independent energy channels.
5) No reflections on both sides of the contacts.

The Fermi-Dirac distribution for contacts 1 and 2 are given by:

Contact 1: $$f_1(E) = \frac{1}{1+\exp(\frac{E-\mu_1}{k_B T_1})}, V_1 = 0 \quad (1.1)$$

Contact 2: $$f_2(E) = \frac{1}{1+\exp(\frac{E-\mu_2}{k_B T_2})}, V_2 = V \quad (1.2)$$

Where f_1 and f_2, μ_1 and μ_2, T_1 and T_2, V_1 and V_2 are the Fermi-Dirac distribution function, chemical potential, temperature, and voltage of contacts 1 and 2, respectively. k_B is Boltzmann's constant. After combining contact 1 and 2 with the conductor, electrons from two contacts will start to fill up the device which induces two flows:

Contact 1: $$F_1(E) = \frac{dN(E)}{dt} = \frac{N_1^0(E) - N(E)}{\tau_1(E)} \quad (1.3)$$

Contact 2: $$F_2(E) = \frac{dN(E)}{dt} = \frac{N_2^0(E) - N(E)}{\tau_2(E)} \quad (1.4)$$

Where F_1 and F_2, N_1^0 and N_1^0, τ_1 and τ_2 are the electron flow, total number of electrons and relaxation time of contacts 1 and 2, respectively. N is the number of electrons inside the device. With the information of band structure, N_1^0 and N_1^0 can be given as: $N_i^0(E) = D^*(E)f_i(E)$ (i = 1,2) where $D^*(E)$ is the effective density of states (in the unit of number of states per unit energy) of the device including the spin degeneracy. Under steady state, the total electron flow $F_{tot} = 0$:

$$F_{tot}(E) = F_1(E) + F_2(E) = \frac{N_1^0(E) - N(E)}{\tau_1(E)} - \frac{N_2^0(E) - N(E)}{\tau_2(E)} = 0 \quad (1.5)$$

If we assume contact 1 and 2 are made of the same material, then we have $\tau_1(E) = \tau_2(E)$. With this assumption, we have:

$$N(E) = \frac{1}{2} D^*(E)[f_1(E) + f_2(E)] \quad (1.6)$$

Under electric field, the electric current is given as:

$$I(E) = qF_1(E) = -qF_2(E) = \frac{q}{2} D^*(E)[f_1(E) - f_2(E)] \quad (1.7)$$

Define $\gamma(E) = \frac{\hbar}{\tau(E)}$ as the energy broadening caused by electron scattering, $\hbar$ is the reduced Plank's constant and $\tau(E)$ is the transit time which will be explained latter. The negative sign in front of F_2 indicates that the electrons are being extracted at contact 2. Integrating **Eq.**(1.6) and **Eq.**(1.7) through the whole energy, we get:

$$N = \int \frac{D^*(E)}{2}[f_1(E) + f_2(E)]dE \quad (1.8)$$

$$I = \frac{2q}{h} \int \gamma(E)\pi \frac{D^*(E)}{2}[f_1(E) - f_2(E)]dE \quad (1.9)$$

When the length of the conductor L is comparable with the electron mean free path $\lambda(E)$, we can assume that there is no scattering happened during the transition of the electrons, this is known as ballistic transport. Now, we explain the physical meaning of transit time. Assuming a 2D conductor sheet with width of W and length of L, as shown in **Figure 1.2** (a). When applying a strong electric field such that $f_2 << f_1$, then:

$$\frac{qN(E)}{I(E)} = \frac{\hbar}{\gamma(E)} \frac{f_1(E) + f_2(E)}{f_1(E) - f_2(E)} \approx \frac{\hbar}{\gamma(E)} = \tau(E) \tag{1.10}$$

In the meantime, in a 2D system,

$$N = n_S W L \tag{1.11}$$

$$I = qW n_S \langle v_x^+(E) \rangle \tag{1.12}$$

n_s is the area charge density of the 2D sheet, $\langle v_x^+(E) \rangle$ is the average electron group velocity along the positive x direction, W and L are the width and length of the sheet, respectively. which is given by an angle integration: $\langle v_x^+(E) \rangle = v(E) \langle \cos\theta \rangle = \frac{2}{\pi} v(E)$. Substituting **Eq.**(1.11) and (1.12) into (10), we have:

$$\tau(E) = L / \langle v_x^+(E) \rangle \tag{1.13}$$

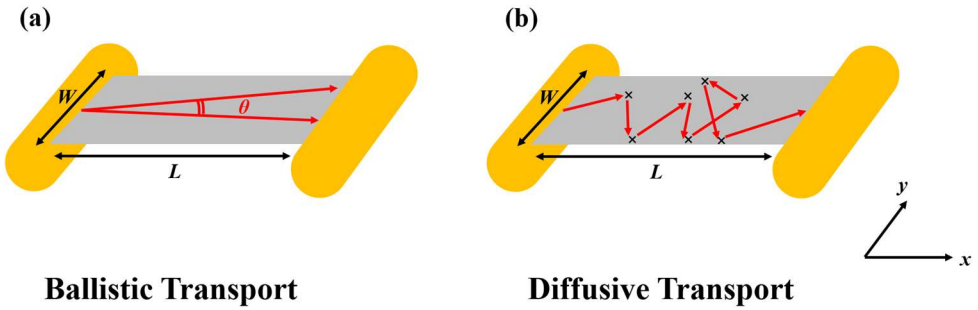

Figure 1.2 (a) Ballistic transport and (b) diffusion transport in a 2D semiconductor device.

The above equation indicates that $\tau(E)$ is the average time for electron travel through the conductor. Now we introduce $M(E) = \gamma(E)\pi\frac{D^*(E)}{2}$; under parabolic picture, it is given by:

$$M(E) = W\frac{h}{4}\langle v_x^+(E)\rangle D_{2\mathrm{D}}(E) = \frac{Wk}{\pi} = \frac{W}{\lambda_{\mathrm{B}}(E)/2} \tag{1.14}$$

$$D_{2\mathrm{D}}(E) = \frac{m^*}{\pi\hbar^2} \tag{1.15}$$

Where $D_{2\mathrm{D}}(E)$ is the effective 2D density of states, m^* is the effective mass of electrons, k is the wave number and λ_{B} is the wavelength of electrons. Based on **Eq**.(15), $M(E)$ is the number of the half wavelengths confined inside the conductor, named as number of conduction channels. Expand this concept to 1D and 3D, we have:

$$M_{1D}(E) = N_{\mathrm{V}}H(E - E_{\mathrm{C}})$$

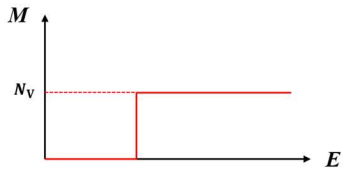

$$M_{2D}(E) = N_{\mathrm{V}}W\frac{\sqrt{2m^*(E - E_{\mathrm{C}})}}{\pi\hbar}$$

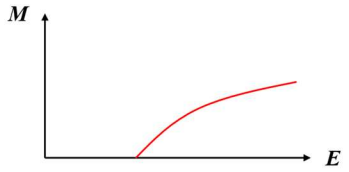

$$M_{3D}(E) = N_{\mathrm{V}}A\frac{m^*}{2\pi\hbar^2}(E - E_{\mathrm{C}})$$

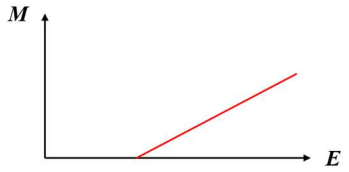

Figure 1.3 Number of channels in different directions (conduction band only).

Here $H(E - E_C)$ is a step function, $H = 0$ when $E < E_C$, $H = 1$ when $E > E_C$. A is the cross section of a 3D semiconductor, N_v is the band degeneracy. When dealing with a macroscopic system, the mean free path of the carriers becomes negligible in comparison with the length of the device, and multiple scattering may happen during the transfer, which is known as diffusive transport, **Figure 1.2** (b). In this case, a correction term will need to be introduced which is known as the transmission term $T(E)$, where $T(E)$ is given by[5]:

$$T(E) = \lambda(E)/L \ll 1 \tag{1.16}$$

$T(E)$ could be understood as the possibility of electron to travel from one contact to the other without experiencing any scattering event. Combining the above equations, we eventually obtain the universal transport equation:

$$I = \frac{2q^2}{h} \int T(E)M(E)[f_1(E) - f_2(E)]dE \tag{1.17}$$

If we apply a small electric field and temperature gradient to the device in **Figure 1.1**, the term $f_1(E) - f_2(E)$ can be expressed as:

$$f_1 - f_2 = f_1(E, \mu_1, T_1) - f_2(E, \mu_2, T_2) \approx \frac{\partial f_1}{\partial \mu} qV + \frac{\partial f_1}{\partial T} \Delta T \tag{1.18}$$

Define $x = (E - \mu)/(k_B T)$, we have the following relations:

$$\frac{\partial f_1}{\partial E} = \frac{\partial f_1}{\partial x}\frac{\partial x}{\partial E} = \frac{\partial f_1}{\partial x}\frac{1}{k_B T} \tag{1.19}$$

$$\frac{\partial f_1}{\partial \mu} = \frac{\partial f_1}{\partial x}\frac{\partial x}{\partial \mu} = \frac{\partial f_1}{\partial x}\left(-\frac{1}{k_B T}\right) = -\frac{\partial f_1}{\partial E} \tag{1.20}$$

$$\frac{\partial f_1}{\partial T} = \frac{\partial f_1}{\partial x}\frac{\partial x}{\partial T} = \frac{\partial f_1}{\partial x}\left(-\frac{E - \mu}{k_B T^2}\right) = \left(-\frac{\partial f_1}{\partial E}\right)\frac{E - \mu}{T} \tag{1.21}$$

Eq.(1.20) and (1.21) describes the underlying thermodynamic driven force that is induced by electric field and temperature gradient, respectively. The qualitative graph for **Eq.**(1.20) and (1.21) are shown in **Figure 1.4**. As can be seen, the driven force induced by electrical field is a delta function, only exists in a narrow energy window of few $k_B T$ (which is known as Fermi window). It indicates that only the electrons in the vicinity of the Fermi level can contribute to the conductivity. Interestingly, when the driven force is provided by a temperature gradient, two opposite fluxes are produced.

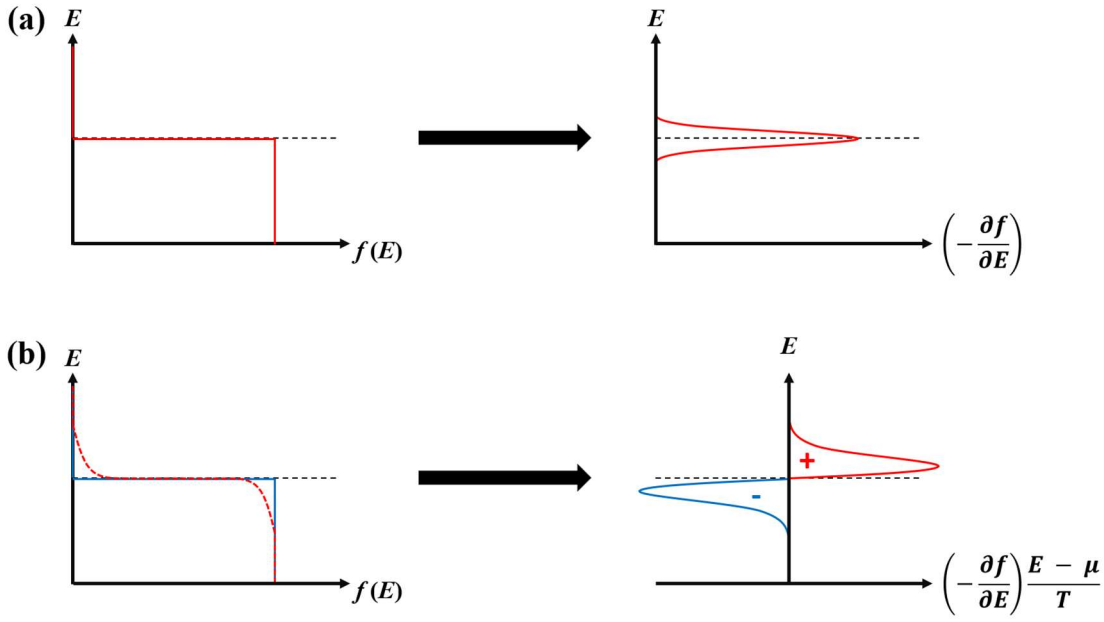

Figure 1.4 Thermodynamic driven force induced by (a) electric field induced and (b) temperature gradient. As can be seen, under a temperature gradient, there are two opposite electron fluxes at two sides of the Fermi energy level.

Substitute Eq.(1.25) ~ (1.28) into Eq.(1.17), we get:

$$I = G_{\mathrm{E}}V + G_{\mathrm{S}}\,\Delta T \tag{1.22}$$

$$G_{\mathrm{E}} = \frac{2q^2}{h}\int T(E)M(E)\left(-\frac{\partial f_1}{\partial E}\right)dE \tag{1.23}$$

$$G_{\mathrm{S}} = \frac{2q^2}{h}\int T(E)M(E)\frac{E-\mu}{qT}\left(-\frac{\partial f_1}{\partial E}\right)dE \tag{1.24}$$

Where G_{E} is the electrical conductance and G_S is the Seebeck effect conductance. The electrical conductivity is defined as:

$$\sigma = G_{\mathrm{E}}(L/A) = \int \sigma'(E)\,dE = \frac{2q^2}{h}\int \lambda(E)\frac{M(E)}{A}\left(-\frac{\partial f_1}{\partial E}\right)dE \tag{1.25}$$

$\sigma'(E)$ is the derivative conductivity. Under open circuit condition, we have:

$$I = G_{\mathrm{E}}V + G_S\Delta T = 0 \rightarrow V = -\frac{G_S}{G_{\mathrm{e}}}\Delta T = S\Delta T \tag{1.26}$$

$$S = -\frac{G_S}{G_{\mathrm{E}}} = -\frac{\frac{2q^2}{h}\frac{A}{L}\int T(E)\frac{M(E)E-\mu}{A\quad qT}\left(-\frac{\partial f_1}{\partial E}\right)dE}{\frac{2q^2}{h}\frac{A}{L}\int T(E)\frac{M(E)}{A}\left(-\frac{\partial f_1}{\partial E}\right)dE} = -\frac{\int\frac{E-\mu}{qT}\sigma'(E)dE}{\sigma} \tag{1.27}$$

Where S is the voltage induced by a unit energy gradient, which is known as the Seebeck coefficient. Depending on the direction of the net flux, S can be positive or negative. As shown in **Figure 1.5**, When the Fermi level is close to the bottom of the conduction band, the net flux points to the positive direction, S is negative, electrons flow from the hot side to the cold side, and the material is a *n*-type conductor. When the Fermi level is close to the top of the conduction band, S is positive, the net flux points to the negative direction, electrons flow from the cold side to the hot side, the material is a *p*-type conductor.

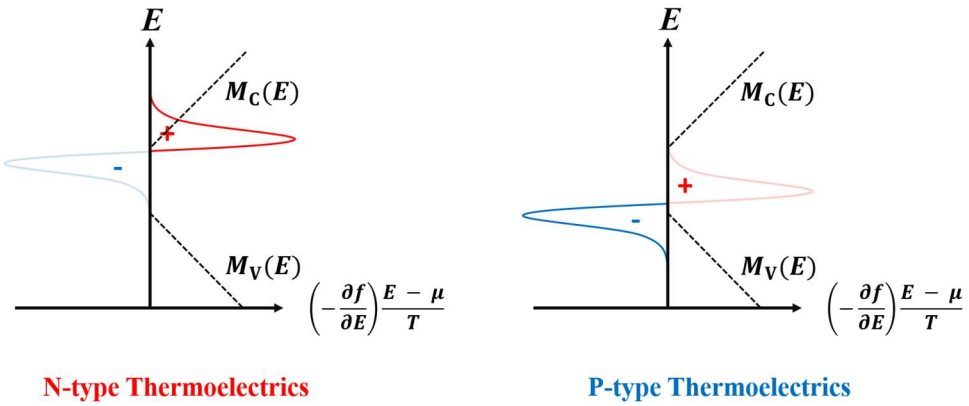

Figure 1.5 A demonstration of the physical interpretation of *n*- and *p*-type thermoelectric materials. The dashed lines are the number of channel functions for both conduction ($M_C(E)$) and valence ($M_V(E)$) bands, respectively.

In addition to charges, carriers can also conduct thermal energy. The heat current induced by the carrier transport can be given by

$$I_Q = \frac{2q}{h}\int (E-\mu)T(E)M(E)[f_1(E) - f_2(E)]dE \tag{1.28}$$

Compared with **Eq**. (1.17), **Eq**. (1.28) changes the charge q that each electron carries to $(E-\mu)$ which is the thermal energy each electron absorbs. By inserting **Eq**. (1.20) and (1.21) into (1.28), we have:

$$I_Q = -G_P V - K_0 \Delta T \tag{1.29}$$

$$G_P = \frac{2q}{h}\int T(E)M(E)\frac{E-\mu}{q}\left(-\frac{\partial f_1}{\partial E}\right)dE \tag{1.30}$$

$$K_0 = \frac{2q}{h}\int T(E)M(E)\left(\frac{E-\mu}{q}\right)^2\frac{1}{T}\left(-\frac{\partial f_1}{\partial E}\right)dE \tag{1.31}$$

G_P is the Peltier thermal conductance induced by the Peltier effect, K_0 is the short circuit thermal conductance. Define π as the Peltier coefficient, it is given by

$$\pi = -\frac{G_P}{G_E} = -\frac{\int T(E)M(E)\frac{E-\mu}{q}\left(-\frac{\partial f_1}{\partial E}\right)dE}{\int T(E)M(E)\left(-\frac{\partial f_1}{\partial E}\right)dE} = TS \tag{1.32}$$

This is known as the Kelvin's relation. From **Eq**. (1.22), we can have:

$$V = IR - S\Delta T \tag{1.33}$$

Where R is the resistance of the device, $R = 1/G_E$. Substitute **Eq**. (1.33) into (1.29):

$$I_Q = -\pi I - (K_0 - \pi S G_E)\Delta T = -\pi I - K_e \Delta T \tag{1.34}$$

$$\kappa_e = K_e \frac{L}{A} = \left\{\left[\frac{\int \frac{(E-\mu)^2}{qT^2}\sigma'(E)dE}{\sigma}\right] - \left[\frac{\int \frac{E-\mu}{qT}\sigma'(E)dE}{\sigma}\right]\left[\frac{\int \frac{E-\mu}{qT^2}\sigma'(E)dE}{\sigma}\right]\right\}\sigma T = L\sigma T \tag{1.35}$$

K_e is the electric thermal conductance, κ_e is the thermal conductivity, L is the Lorenz number. **Eq**. (1.35) is known as the Wiedemann-Franz law[6].

1.2.2 Phonon Transport

The derivation of phonon transport is similar to that of electron transport. Instead of using Fermi-Dirac distribution, we now use Bose-Einstein distribution $B(E)$ to describe phonon distribution:

$$B(E) = \frac{1}{\exp(\hbar\omega/k_B T_L) - 1} \tag{1.36}$$

Where ω is the phonon frequency and T is the lattice temperature. The heat current Q that carried by phonon is then given by:

$$Q = \frac{1}{h}\int_0^\infty \hbar\omega T_{ph}(\hbar\omega) M_{ph}(\hbar\omega)[B_1(\hbar\omega) - B_2(\hbar\omega)]d(\hbar\omega) \tag{1.37}$$

Where T_{ph} and M_{ph} are the transmission term and number of conduction channels of phonon, respectively. Similarly, $T_{\mathrm{ph}}(\hbar\omega) = \lambda_{\mathrm{ph}}(\hbar\omega)/L$. B_1 and B_2 are the Bose-Einstein distribution of two contacts. Under near-equilibrium approximation, $B_1 - B_2$ is given by:

$$B_1(\hbar\omega) - B_2(\hbar\omega) \approx -\frac{dB_1}{dT}\Delta T \tag{1.38}$$

$$-\frac{dB_1}{dT} \approx -\frac{\hbar\omega}{T_{\mathrm{L}}}\left[-\frac{dB_1}{d(\hbar\omega)}\right] \tag{1.39}$$

Substituting **Eq.**(1.21) into **Eq.**(1.19), we have:

$$Q = -K_{\mathrm{L}}\,\Delta T \tag{1.40}$$

$$K_{\mathrm{L}} = \frac{\pi^2 k_{\mathrm{B}}^2 T_{\mathrm{L}}}{3h}\int_0^{\infty} T_{\mathrm{ph}}(\hbar\omega) M_{\mathrm{ph}}(\hbar\omega)\left\{\frac{3}{\pi^2}\left(\frac{\hbar\omega}{k_{\mathrm{B}}T_{\mathrm{L}}}\right)^2\left[-\frac{dB_1}{d(\hbar\omega)}\right]\right\} d(\hbar\omega) \tag{1.41}$$

$$\kappa_{\mathrm{L}} = K_{\mathrm{L}}\left(\frac{L}{A}\right) = \frac{\pi^2 k_{\mathrm{B}}^2 T_{\mathrm{L}}}{3h}\int_0^{\infty} \lambda_{\mathrm{ph}}(\hbar\omega)\frac{M_{\mathrm{ph}}(\hbar\omega)}{A}\left\{\frac{3}{\pi^2}\left(\frac{\hbar\omega}{k_{\mathrm{B}}T_{\mathrm{L}}}\right)^2\left[-\frac{dB_1}{d(\hbar\omega)}\right]\right\} d(\hbar\omega) \tag{1.42}$$

Where K_{L} and κ_{L} are the thermal conductance and thermal conductivity, respectively. The derivation of number of channels of phonon is beyond the scope of this thesis. More details related to the lattice thermal conductivity model can be found in [7,8].

1.3 From Near-equilibrium Transport to Real Device – Figure of Merit

In the above discussions, we derived all the thermoelectric properties under near-equilibrium condition. This theory can only be applied to nano-devices or systems under weak electrical and thermal perturbation. However, in real life, the device strongly deviates from the equilibrium state. To build a connection between the near-equilibrium transport and a real device, we make the approximation as shown in Figure 1.6.

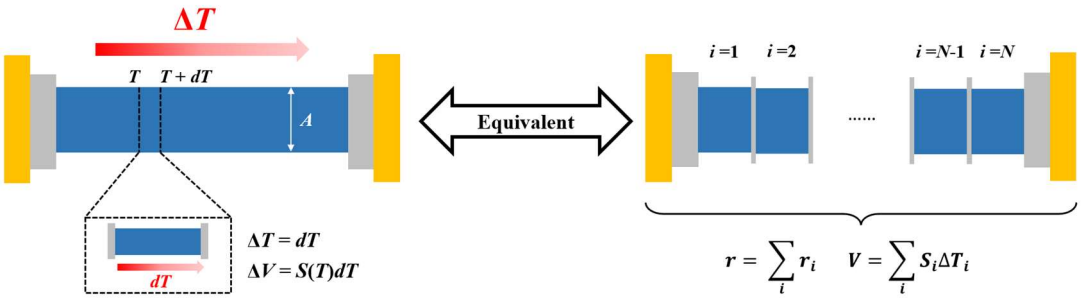

Figure 1.6 From the near-equilibrium approximation to a real device.

Assume a macroscopic bulk device with a length of L, cross section of A and a temperature distribution of $T(x)$. Assume $x = 0$ is the hot source (active cooling) side and $x = L$ is the heat sink side. If we dissect the bulk device into countless infinitesimal elements such that the temperature difference inside this small area is dT, then each element could be treated as a near-equilibrium system. Under this circumstance, the total Seebeck voltage and resistance is given by[9]

$$V = \lim_{N\to\infty} \sum_i^N S_i \Delta T_i = \int_{T_c}^{T_h} S(T) dT \tag{1.43}$$

$$r = \lim_{N\to\infty} \sum_i^n r_i = \int_{T_c}^{T_h} \frac{d}{dT}\left(\frac{1}{G_E(T)}\right) dT = \frac{1}{T_h - T_c} \int_{T_c}^{T_h} R(T) dT \tag{1.44}$$

Where V is the total voltage induced by Seebeck effect, r is the internal resistance of the device and R is the resistance. The subscript i stands for the i^{th} element. On the premise of this approximation, the device performance of thermoelectric generator.

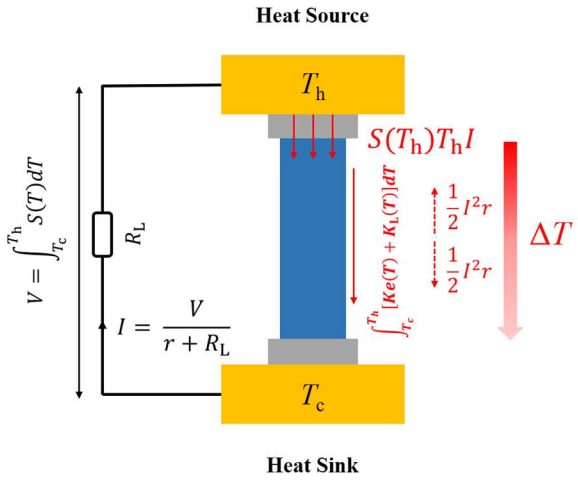

Figure 1.7 Single-leg thermoelectric generator

The structure of a single-leg thermoelectric generator is shown in **Figure 1.7**. If the external load resistance is R_L, then the output power, P, is given by:

$$P = I^2 R_L = \left(\frac{V}{r+R_L}\right)^2 R_L \tag{1.45}$$

r is the internal resistance (resistance of the thermal leg), P is the electric power applied onto the external load resistance R_L, I is the electric current. The thermal flow injected into the system from the hot side is given by[10]

$$Q_{in} = \int_{T_c}^{T_h}[K_e(T) + K_L(T)]dT + IT_hS(T_h) - \frac{1}{2}I^2r \tag{1.47}$$

$$I = \frac{V}{r+R_L} = \frac{\int_{T_c}^{T_h} S(T)dT}{R_L + \frac{1}{T_h - T_c}\int_{T_c}^{T_h} R(T)dT} \tag{1.48}$$

The thermal flow consists of three parts – the heat transfer from the hot contact, Peltier heating (cooling) at the contact interface and the heat reflux induced by the Joule heating in the thermal leg. The efficiency of the device is then given by

$$\eta = \frac{P}{Q} \tag{1.49}$$

Define $m = R_L/r$. The device efficiency is maximized when m is [10]

$$m = \left[1 + Z\left(\frac{T_h+T_c}{2}\right)\right]^{1/2} \tag{1.50}$$

$$Z = \frac{1}{T_h-T_c}\frac{V^2}{r(K_e+K_L)} \tag{1.51}$$

Z is defined as the device figure of merit, *FOM*, with the dimensions of K^{-1}. Substituting **Eq.** (1.44) and (1.46) into (1.51), we have

$$Z = \frac{\left(\int_{T_c}^{T_h} S(T)dT\right)^2}{\int_{T_c}^{T_h}\rho(T)dT\int_{T_c}^{T_h}[\kappa_e(T)+\kappa_L(T)]dT} \tag{1.52}$$

Where ρ is the resistivity. Substituting **Eq.** (1.45) ~ (1.48) and (1.50) ~ (1.53) into (1.49), the device efficiency is finally given by

$$\eta = \frac{\frac{m}{m+1}}{\frac{1+m}{Z(T_h-T_c)}+\frac{S(T_h)T_h}{V}-\frac{1}{2(1+m)}} \tag{1.54}$$

As it can be seen, when $T(0)$ and $T(L)$ are fixed, the device efficiency is determined by *FOM*. Under given T_c and T_h, FOM is completely determined by the intrinsic properties of the material: S, ρ, κ_e and κ_L. Under Landauer's formalism, these values can be calculated via Eq. (1.27), (1.25), (1.35) and (1.42), respectively.

Chapter 2: Modeling of Thermoelectric Materials

2.1 Introduction

In this chapter, based on the Landauer's approach, the modeling method for thermoelectric properties simulation will be introduced. The purpose of modeling is to predict the theoretical optimal zT value of a given material so that it can be used to guide the material design and synthesis. To calculate the number of channels $M(E)$, materials' band structure will need to be obtained. The ground state band structure (electron energy dispersion relation) can be obtained based on the density functional theory (DFT). Here, the elementary concepts of DFT calculations will be introduced following the discussion in[11] Subsequently, simulation strategies for thermoelectric properties will be introduced.

2.2 Fundamentals of Density Functional Theory Calculations

2.2.1 Many-Body Schrödinger Equation

To simply the problem, two approximations are made[11]:

a) Independent electron approximation: no strong electron-electron coupling.

b) Clamped nuclei approximation: ignore the lattice vibration.

Under the above assumptions, the Schrödinger equation is given by

$$\left[-\frac{\hbar^2}{2m^*}\vec{\nabla}^2 + U^{ion}(\vec{r}) + \frac{1}{2}\int\int\frac{e^2}{|\vec{r}-\vec{r}'|}\rho(\vec{r})\rho(\vec{r}')d\vec{r}\,d\vec{r}'\right]\psi_i(\vec{r}) = \varepsilon_i\psi_i(\vec{r}) \tag{2.1}$$

Here $U^{ion}(\vec{r})$ is the periodic potential provided by the lattice, $\psi_i(\vec{r})$ is the eigenfunction and ε_i is the eigenstate. $\rho(\vec{r})$ is the electron density at a spatial vector $\vec{r}$. Under independent electron approximation, it can be given by

$$\rho(\vec{r}) = \sum_i [|\psi_i(\vec{r})|^2] \tag{2.2}$$

In the Hamiltonian, the first term describes the kinetic energy of the electron, the second term is the electron-nuclei interaction, and the third term is a simplified electron-electron interaction. Substituting **Eq**. (2.2) into (2.1), we have

$$\left[-\frac{\hbar^2}{2m^*}\vec{\nabla}^2 + U^{ion}(\vec{r}) + \sum_j \int \frac{e^2}{|\vec{r}-\vec{r}'|}\left|\psi_j(\vec{r}')\right|^2 d\vec{r}'\right]\psi_i(\vec{r}) = \varepsilon_i\psi_i(\vec{r}) \tag{2.3}$$

Define $U^{el}(\vec{r}) = \sum_j \int \frac{e^2}{|\vec{r}-\vec{r}'|}\left|\psi_j(\vec{r}')\right|^2 d\vec{r}'$ as the Hartree potential which treats electron-electron interactions as an average potential field. **Eq**. (2.3) is also known as the Hartree's equation. Because of the independent electron approximation, the total wave function Ψ can be written as

$$\Psi(\vec{r}_1, \vec{r}_2, \vec{r}_3, \dots, \vec{r}_N; \hat{s}_1, \hat{s}_2, \hat{s}_3, \dots, \hat{s}_N) = \prod_i^N \psi_i(\vec{r}_i, \hat{s}_i) \tag{2.4}$$

$\vec{r}_i$ and $\hat{s}_i$ are the coordinate and spin operators of the i^{th} electron. The Pauli exclusion principle requires that each time when two electrons exchange their quantum state, the function changes its sign. This could be mathematically realized by writing the wavefunction as a Slater's determinant[12]:

$$\Psi(\vec{r}_1, \vec{r}_2, \vec{r}_3, \dots, \vec{r}_N; \hat{s}_1, \hat{s}_2, \hat{s}_3, \dots, \hat{s}_N) = \frac{1}{\sqrt{N!}}\begin{bmatrix} \psi_1(\vec{r}_1, \hat{s}_1) & \cdots & \psi_1(\vec{r}_N, \hat{s}_N) \\ \vdots & \ddots & \vdots \\ \psi_N(\vec{r}_1, \hat{s}_1) & \cdots & \psi_N(\vec{r}_N, \hat{s}_N) \end{bmatrix} \tag{2.5}$$

By bringing Eq. (2.5) into (2.3), we obtained the Hartree-Fock equation (H-F equation)[13,14]

$$\left[-\frac{\hbar^2}{2m^*}\vec{\nabla}^2 + U^{ion}(\vec{r}) + U^{el}(\vec{r}) - \sum_j \frac{e^2}{|\vec{r}-\vec{r}'|}\psi_j^*(\vec{r}')\psi_i(\vec{r}')\psi_j(\vec{r})\delta_{\hat{s}_i\hat{s}_j}\right]\psi_i(\vec{r}) = \varepsilon_i\psi_i(\vec{r}) \qquad (2.6)$$

ψ_j^* is the complex conjugate of ψ_j. $\delta_{\hat{s}_i\hat{s}_j}$ is a delta function: $\delta_{\hat{s}_i\hat{s}_j} = 1$ when $\hat{s}_i = \hat{s}_j$, $\delta_{\hat{s}_i\hat{s}_j} = 0$ when $\hat{s}_i \neq \hat{s}_j$. After introducing the Pauli exclusion principle into the Schrödinger equation, an extra term shows up, which is known as the exchange energy $U^{ex}(\vec{r})$. The delta function can be considered as a switch, this term only activates when two electrons with the same spin are approaching each other. The Pauli exclusion principle forbids electrons from overlapping with each other. As a result, these electrons spatially avoid each other and reduce the potential energy of the system. If the crystal structure and electron density function are known, then all terms can be calculated except for the $U^{ex}(\vec{r})$.

Although $U^{ex}(\vec{r})$ of an arbitrary electron distribution function is unsolvable, it is possible to derive the exchanging energy of ideal electron gas. Here, we skip the mathematical derivation process. Interested readers are referred to Ref.[15] and [16]. $U^{ex}(\vec{r})$ of the ideal electron gas (IEG) model is given by

$$U_{\mathrm{IEG}}^{ex}(\vec{r}) = -\frac{3}{4}\left(\frac{3}{\pi}\right)^{\frac{1}{3}}\rho^{\frac{1}{3}} \qquad (2.7)$$

For ideal electron gas, ρ is a constant. Slater proposed that the $U^{ex}(\vec{r})$ of any arbitrary charge density distribution can be calculated by splitting the system into infinitesimal unit volumes and treat these small areas as local ideal electron gasses and integrating through the whole space[17]:

$$U_{\mathrm{LDA}}^{ex}(\vec{r}) = \int U_{\mathrm{IEG}}^{ex}(\vec{r})\,\rho(\vec{r})d^3\vec{r} \qquad (2.8)$$

This approach has been well developed and it is nowadays known as the localized density approximation (LDA). Except for the exchanging term, there is another correction term called correlation energy $U^c_{\mathrm{IEG}}(\vec{r})$. This quantity cannot be calculated analytically. The value of this term has been numerically obtained via quantum Monte Carlo simulations and fitted into a parameterized function. The most popular parameterization is the one proposed by Perdew and Wang in 1992 (PW92)[18]. Further improvements to the approximation were done by considering the local density gradient. This is known as the generalized gradient approximation (GGA):

$$U^{xc}_{\mathrm{GGA}}(\vec{r}) = \int \rho(\vec{r}) U^{ex}_{\mathrm{IEG}}(\vec{r}) F \, d^3\vec{r} + \int \rho(\vec{r}) [U^c_{\mathrm{IEG}}(\vec{r}) + H] \, d^3\vec{r} \qquad (2.9)$$

Where *F* and *H* are correction functions of LDA. The most used correction is given by Perdew-Burke-Ernzerhof (PBE)[19].

2.2.2 Band structure

In the previous discussion, we see that all external interaction terms in the Hamiltonian are functionals of the charge density distribution function. We rewrite Eq. (2.6):

$$\left[-\frac{\hbar^2}{2m^*}\vec{\nabla}^2 + U^{ion}[\rho(\vec{r})] + U^{el}[\rho(\vec{r})] + U^{xc}[\rho(\vec{r})]\right]\psi_i(\vec{r}) = \varepsilon_i \psi_i(\vec{r}) \qquad (2.10)$$

U^{xc} is the exchanging-correlation energy, which is simply the sum of $U^{ex}(\vec{r})$ and $U^c(\vec{r})$. **Eq**. (2.10) is known as the Kohn-Sham (K-S) equation. Bloch theorem states that for a single-particle wavefunction under periodic potential, which is exactly the case for crystals, the wavefunction can be rewritten as

$$\psi_i(\vec{r}) = \psi_{i\vec{k}}(\vec{r}) = e^{i\vec{k}\vec{r}} u_{i\vec{k}}(\vec{r}) \qquad (2.11)$$

Where $u_{i\vec{k}}(\vec{r})$ has the same periodicity of the lattice. By substituting Eq. (2.11) into Eq. (2.10), we have the crystal version of the K-S equation

$$\left[-\frac{\hbar^2}{2m^*}(\vec{\nabla}+i\vec{k})^2+U^{tot}[\rho(\vec{r})]\right]u_{i\vec{k}}(\vec{r})=\ \varepsilon_{i\vec{k}}u_{i\vec{k}}(\vec{r}) \tag{2.12}$$

In the reciprocal space, the electron density can be solved within the first Brillouin zone

$$\boldsymbol{\rho}'(\vec{\boldsymbol{r}})=\sum_i\int\frac{d\vec{\boldsymbol{k}}}{\Omega_{\mathrm{BZ}}}f_{i\vec{\boldsymbol{k}}}\left|u_{i\vec{k}}(\vec{r})\right|^2 \tag{2.13}$$

$f_{i\vec{\boldsymbol{k}}}$ is the occupancy factor; $f_{i\vec{\boldsymbol{k}}}=1$ if the energy state is occupied, and $f_{i\vec{\boldsymbol{k}}}=0$ if it is unoccupied. The eigenvalue of this equation contains the information about the band structure. The Hohenberg-Kohn theorem state that[20]:

a) In a non-degenerate ground state, the electron density determines uniquely the $U^{ion}(\vec{r})$.
b) In any quantum state, the $U^{ion}(\vec{r})$ determines uniquely the many body wavefunction Ψ.
c) In any quantum state, the total energy E is a functional of Ψ, $E=F[\Psi]$.

Assuming that the crystal structure is known, then $U^{ion}(\vec{r})$ could be directly obtained. The K-S equation can be solved by performing self-consistent field calculations (SCF). The flowchart of these calculations is shown in **Figure 2.1**.

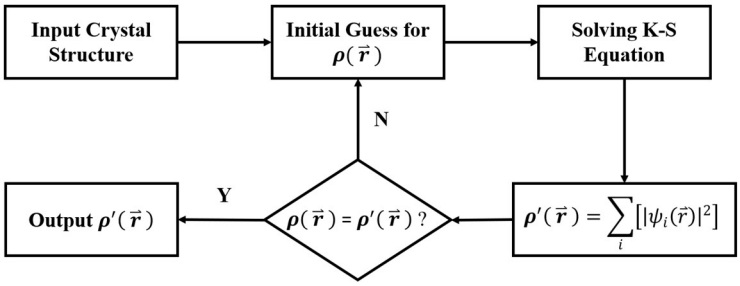

Figure 2.1 Flowchart of the SCF calculation.

Using the provided crystal structure, the initial $\rho(\vec{r})$ is chosen as the superposition of the atomic orbitals. The K-S equation is then solved by the provided electron density. New electron density $\rho'(\vec{r})$ is constructed from the obtained eigenfunctions $\psi_i(\vec{r})$ via **Eq**. (2.2). The new and initial electron density are compared. If the difference is larger than the threshold (set by us), then the loop starts again. If the difference is smaller than the threshold, $\rho'(\vec{r})$ is taken as the result. Using this electron density, the K-S equation is solved and the obtained $\varepsilon_{i\vec{k}} = \varepsilon_i(\vec{k})$ is used to construct the band structure.

2.2.3 Crystal Structure Relaxation

To obtain the correct electron density, it is essential to fully relax the crystal structure to bring the system to the ground state. Although the crystallographic information could be directly obtained from X-ray diffraction (XRD), the result is usually not good enough for direct calculation. The XRD result is a statistical average which may not capture the local distortion caused by impurity atoms. Also, structural analysis is usually done at room temperature, which introduces thermal expansion with respect to the 0K structure. Therefore, a structure relaxation must be done before the calculation of any properties. For

simplicity, we assume that the lattice does not exchange energy with electrons. This is known as the Born-Oppenheimer approximation or adiabatic approximation[21]. The Schrödinger equation can then be rewritten as two separate functions

$$\Psi(\vec{r}_1, \vec{r}_2, \vec{r}_3, \dots, \vec{r}_N; \vec{R}_1, \vec{R}_2, \vec{R}_3, \dots, \vec{R}_M) = \psi(\vec{r}_1, \vec{r}_2, \vec{r}_3, \dots, \vec{r}_N)\chi(\vec{R}_1, \vec{R}_2, \vec{R}_3, \dots, \vec{R}_M) \quad (2.14)$$

ψ and χ correspond to the electron and nuclei parts of the wavefunctions, respectively. For each set of nuclei coordinates $[\vec{R}]$, we have

Electron: $$\left[-\frac{\hbar^2}{2m^*}\sum_i \vec{\nabla}_i^2 + U^{ion}(\vec{r}_i; [\vec{R}]) + \frac{1}{2}\sum_{i\neq j}\frac{e^2}{|\vec{r}_i - \vec{r}_j|}\left|\psi_j(\vec{r}_j)\right|^2\right]\psi_R = \varepsilon_R\psi_R \quad (2.15)$$

Nuclei: $$\left[-\frac{\hbar^2}{2M_I}\sum_I \vec{\nabla}_I^2 + \frac{1}{2}\sum_{I\neq J}\frac{Z_I Z_J}{|\vec{R}_I - \vec{R}_J|}\right]\chi = E_R\chi \quad (2.16)$$

Total: $$\varepsilon_R\psi_R + \left[-\frac{\hbar^2}{2M_I}\sum_I \vec{\nabla}_I^2 + \frac{1}{2}\sum_{I\neq J}\frac{Z_I Z_J}{|\vec{R}_I - \vec{R}_J|}\right]\psi_R\,\chi = E_{\text{total}}\psi_R\,\chi \quad (2.17)$$

M_I, Z_I and $\vec{R}_I$ are the mass, charge and spatial coordinates of the nuclei. After multiplying both sides of **Eq**. (2.17) by ψ_R^*, we have

$$\left[-\frac{\hbar^2}{2M_I}\sum_I \vec{\nabla}_I^2 + \frac{1}{2}\sum_{I\neq J}\frac{Z_I Z_J}{|\vec{R}_I - \vec{R}_J|} + \varepsilon(\vec{R}_1, \vec{R}_2, \vec{R}_3, \dots, \vec{R}_M)\right]\chi = E_{\text{total}}\chi \quad (2.18)$$

For simplicity, define the nuclei Hamiltonian $\hat{H}_N = -\frac{\hbar^2}{2M_I}\sum_I \vec{\nabla}_I^2 + U(\vec{R}_1, \vec{R}_2, \vec{R}_3, \dots, \vec{R}_M)$. Here, $U = \frac{1}{2}\sum_{I\neq J}\frac{Z_I Z_J}{|\vec{R}_I - \vec{R}_J|} + \varepsilon(\vec{R}_1, \vec{R}_2, \vec{R}_3, \dots, \vec{R}_M)$. At the ground state, the nuclei behave classically (except for the hydrogen atom). Therefore, we can adopt classical Newton's mechanics into the Hamiltonian to simplifies the problem:

$$\widehat{H}_N = \sum_I \frac{P_I^2}{2M_I} + U\left(\vec{R}_1, \vec{R}_2, \vec{R}_3, \dots, \vec{R}_M\right) \tag{2.19}$$

The Newton's equation of motion is then given by

$$M_I \frac{d^2\vec{R}_I}{dt^2} = -\frac{\partial U}{\partial \vec{R}_I} \tag{2.20}$$

The right-hand side is the force acting on the nuclei

$$\vec{F}_I = -\frac{\partial U}{\partial \vec{R}_I} \tag{2.21}$$

Based on Hellmann-Feynman theorem[22–25], we finally have

$$\vec{F}_I = Z_I \left[\int \rho(\vec{r}) \frac{r - R_I}{|r - R_I|^3} - \sum_{I \neq J} Z_J \frac{R_J - R_I}{|R_J - R_I|^3} \right] \tag{2.22}$$

Eq. (2.22) directly links the atomic forces with the electron density. If we can determine the electron density of an atomic coordinates set, then the forces onto each atom can be calculated. Although we can now derive the atomic forces, finding the equilibrium positions for the atom is a rather complex task, and this topic is beyond the scope of this thesis. **Eq**. (2.21) indicates that, the process of finding the equilibrium position is the process of finding the local minima on the potential energy surface *U*. **Figure 2.2** shows the flowchart of structure relaxation calculation.

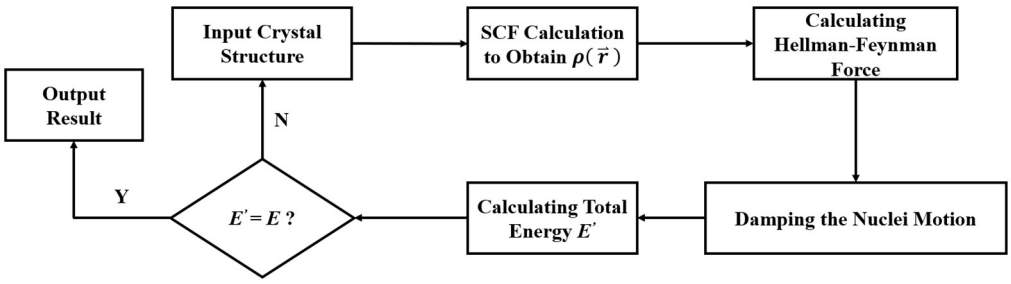

Figure 2.2 Flowchart for structure relaxation.

Instead of tracking the nuclei coordinates to evaluate the convergence, a more convenient way is to look at the total energy of the system. After obtaining the electron density function, the total energy can be given by

$$E = \sum_i \langle \psi_i^*(\vec{r}_i) \left| -\frac{\hbar^2}{2m^*}\vec{\nabla}_i^2 + U^{tot}[\rho(\vec{r})] \right| \psi_i(\vec{r}) \rangle \tag{2.23}$$

2.3 Single (Multi) Band Simulation for Electric Properties

Here, the well-developed modeling methods will be briefly introduced, and their basic calculation frameworks will be presented.

2.3.1 Single Parabolic Band Model

A single parabolic band model is suitable for materials with only one parabolic band or with multiple parabolic bands that converged within a small energy window. For simplicity, here we only discuss the case of a parabolic conduction band and set the bottom of the conduction band as zero energy. The same equation can be easily adopted to the valence band by introducing a negative sign in front of the Seebeck coefficient. If we consider only acoustic phonon scattering, the thermoelectric parameters under this model are given by[26]:

$$S = -\frac{k_B}{e}\left[\frac{2F_1}{F_0} - \xi\right] \tag{2.24}$$

$$L = \left(\frac{k_B}{e}\right)^2 \frac{3F_2(\xi)}{F_1(\xi)} - \left[\frac{2F_1(\xi)}{F_0(\xi)}\right]^2 \tag{2.25}$$

$$n = A_H n_{\mathrm{H}} = \frac{(2m_{\mathrm{d}}^* k_B T)^{3/2}}{3\pi^2 \hbar^3} \frac{2F_0^2(\xi)}{F_{-1/2}(\xi)} \tag{2.26}$$

$$A_H = \frac{3}{2} F_{1/2} \frac{F_{-1/2}}{2F_0^2} \tag{2.27}$$

$$F_s = \int_0^\infty \frac{\varepsilon^s}{1+\exp(\varepsilon-\xi)} d\varepsilon \tag{2.28}$$

Here ξ is the reduced chemical potential $\xi = \mu/(k_{\mathrm{B}}T)$, ε is the reduced energy $\varepsilon = E/(k_{\mathrm{B}}T)$, A_{H} is the Hall factor, n_{H} is the Hall carrier concentration, n is the actual carrier concentration and μ_{H} is the Hall mobility. m_{d}^* is the density of states effective mass and is given by

$$m_{\mathrm{d}}^* = N_{\mathrm{V}}^{2/3} m_{\mathrm{b}}^* \tag{2.29}$$

where m_{b}^* is the single band effective mass.

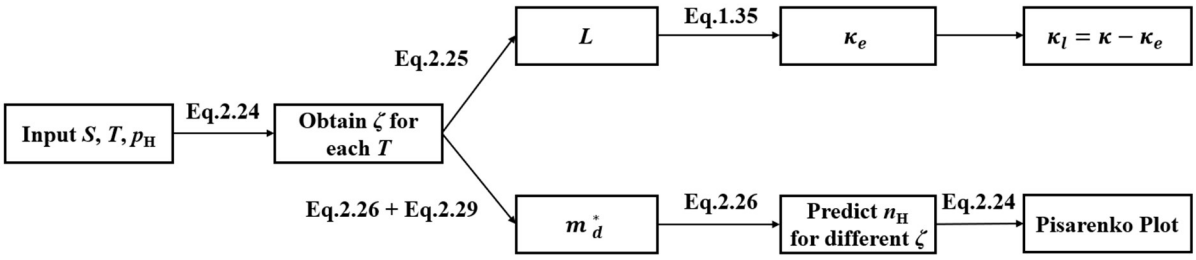

Figure 2.3 Calculation framework for a single parabolic band model.

By using the measured temperature dependent Seebeck coefficient, the position of the chemical potential can be determined via **Eq**. (2.24). Subsequently, the Lorenz number and Hall factor can be calculated via **Eq**. (2.25) and (2.27), respectively. The electrical thermal conductivity κ_{e} can then be calculated by Wiedemann-Franz law, **Eq**. (1.35). By extracting κ_{e} from the total thermal conductivity κ, the lattice thermal conductivity κ_{l} can

then be obtained. Combined with the carrier concentration data from Hall effect measurement, m_{d}^{*} can be calculated via **Eq**. (2.26). Using the obtained m_{d}^{*} as an input, the position of the chemical potential under different carrier concentration can be determined. With this knowledge, the optimal carrier concentration at a given temperature can be determined by the Pisarenko plot (*S* vs. *n* curve).

2.3.2 Single Kane Band Model

Most of the thermoelectric materials are narrow band gap semiconductors (i.e., Bi_2Te_3, PbTe, SnTe etc.). Their conduction and valence bands interact strongly with each other, which makes the band edges highly non-parabolic. Therefore, a correction term called non-parabolic factor α will be introduced into the dispersion relation[27]:

$$E(\vec{k}) = \frac{\hbar^2\vec{k}^2}{2m_b^*} \rightarrow E(\vec{k})\left[1 + \alpha E(\vec{k})\right] = \frac{\hbar^2\vec{k}^2}{2m_b^*} \tag{2.30}$$

$$\alpha = k_{\mathrm{B}}T/E_{\mathrm{g}} \tag{2.31}$$

E_{g} is the direct band gap. When the band gap is large, α will become negligible and the dispersion relationship converges with the parabolic band model. Again, we set the bottom of the conduction band as the zero energy. Under this circumstance, Eq. (2.24) ~ (2.28) will be rewritten as[28]:

$$S' = -\frac{k_{\mathrm{B}}}{e}\left[\frac{{}^{1}F_{-2}^{1}}{{}^{0}F_{-2}^{1}} - \xi\right] \tag{2.32}$$

$$L' = \left(\frac{k_{\mathrm{B}}}{e}\right)^2\left[\frac{{}^{2}F_{-2}^{1}}{{}^{0}F_{-2}^{1}} - \left(\frac{{}^{1}F_{-2}^{1}}{{}^{0}F_{-2}^{1}}\right)^2\right] \tag{2.33}$$

$$n' = A_{\mathrm{H}}n_{\mathrm{H}} = \frac{\left(2m_{\mathrm{d}}^{*}k_BT\right)^{3/2}}{3\pi^2\hbar^3}\,{}^{0}F_0^{3/2} \tag{2.34}$$

$$A_{\mathrm{H}} = \frac{3K(K+2)}{(2K+1)^2}\frac{{}^0F_{-4}^{1/2}\,{}^0F_0^{3/2}}{\left({}^0F_{-2}^{1}\right)^2} \tag{2.35}$$

$${}^nF_k^m = \int_0^\infty \left(-\frac{\partial f}{\partial \varepsilon}\right)\varepsilon^n(\varepsilon+\alpha\varepsilon^2)^m[(1+2\alpha\varepsilon)^2+2]^{k/2}d\varepsilon \tag{2.36}$$

${}^nF_k^m$ is the Fermi-Dirac integral for the Kane band. S', L' and n' are the Seebeck coefficient, Lorenz number and actual carrier concentration of the Kane band model. The introduction of a band gap brings one more complexity into the equation. It is well known that Bi_2Te_3 and SnTe are topological insulators[29–31], and unlike other normal semiconductors whose band gaps increase with energy, the band gaps of Bi_2Te_3 and SnTe decrease with temperature, making the effective mass highly temperature dependent. The calculation framework for the single Kane band model is similar to that of the parabolic band, as shown in **Figure 2.4**.

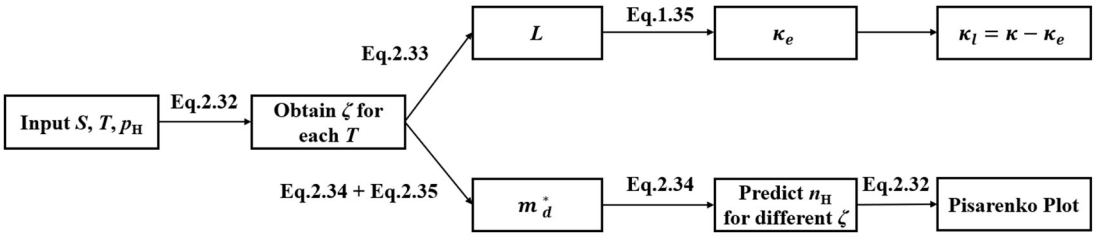

Figure 2.4 Calculation framework for single Kane band model.

2.3.3 Multi-Band Model

Most of the thermoelectric materials have complex Fermi surfaces with large number of carrier pockets in the vicinity of the Fermi level. Consequently, the single band model cannot accurately describe their properties. In this case, a multi-band model needs to be established.

For convenience, here we reproduce **Eq**. (1.25) :

$$\sigma = G_E(L/A) = \int \sigma'(E)\, dE = \frac{2q^2}{h} \int \frac{\lambda(E)}{A} M(E) \left(-\frac{\partial f_1}{\partial E}\right) dE \tag{2.37}$$

A number of channels $M(E)$ can be provided by multiple bands

$$M(E) = \sum_i M_i(E - \Delta E_i) \tag{2.38}$$

M_i is the number of channels of the i^{th} band at a given energy. If we assign a particular band as our principal band, then ΔE_i is the energy offset of the i^{th} band with respect to the bottom (top) of the conduction (valence) band. Substituting Eq. (2.38) into (2.37), we have

$$\sigma = \sum_i \int_0^\infty \frac{\lambda(E-\Delta E_i)}{A} M(E - \Delta E_i) \left[-\frac{\partial f_1(E-\Delta E_i)}{\partial (E-\Delta E_i)}\right] d(E - \Delta E_i) \tag{2.38}$$

The conductivity of the material is simply the sum of the conductivity contributed by each band. Therefore, the total Seebeck and Peltier coefficient are given as

$$S = \frac{\sum_i S_i \sigma_i}{\sum_i \sigma_i} \tag{2.39}$$

$$\pi = TS = \frac{\sum_i \pi_i \sigma_i}{\sum_i \sigma_i} \tag{2.40}$$

The expression for the total Lorenz number, however, is not as clean and tidy as the above two. Recall that from Eq. (1.34), we have

$$\kappa_e = \kappa_0 - TS^2\sigma \tag{2.41}$$

$$\kappa_0 = K_0 \frac{L}{A} = T \frac{2q}{h} \int \lambda(E) \frac{M(E)}{A} \left(\frac{E-\mu}{qT}\right)^2 \left(-\frac{\partial f_1}{\partial E}\right) dE \tag{2.42}$$

For simplicity, we define

$$\varkappa = \frac{\int \lambda(E)\frac{M(E)}{A}\left(\frac{E-\mu}{qT}\right)^2\left(-\frac{\partial f_1}{\partial E}\right)dE}{\int \lambda(E)\frac{M(E)}{A}\left(-\frac{\partial f_1}{\partial E}\right)dE} \tag{2.43}$$

Substituting Eq. (2.43) into Eq. (2.42), we have

$$L = \frac{\kappa_e}{T\sigma} = \varkappa - S^2 = \frac{\sum_i \varkappa_i \sigma_i}{\sum_i \sigma_i} - \left[\frac{\sum_{ij}(S_i\sigma_i)(S_j\sigma_j)}{\sum_{ij}\sigma_i\sigma_j}\right] \tag{2.44}$$

The term $\left[\frac{\sum_{ij}(S_i\sigma_i)(S_j\sigma_j)}{\sum_{ij}\sigma_i\sigma_j}\right]$ indicates that all bands coupled to one another contribute to the Lorenz number. If one directly simulates the Lorenz number in the form, which similar to **Eq**. (2.39), a large deviation may occur even in a two-band model. This issue was thoroughly discussed in Thesberg et al.'s work[32].

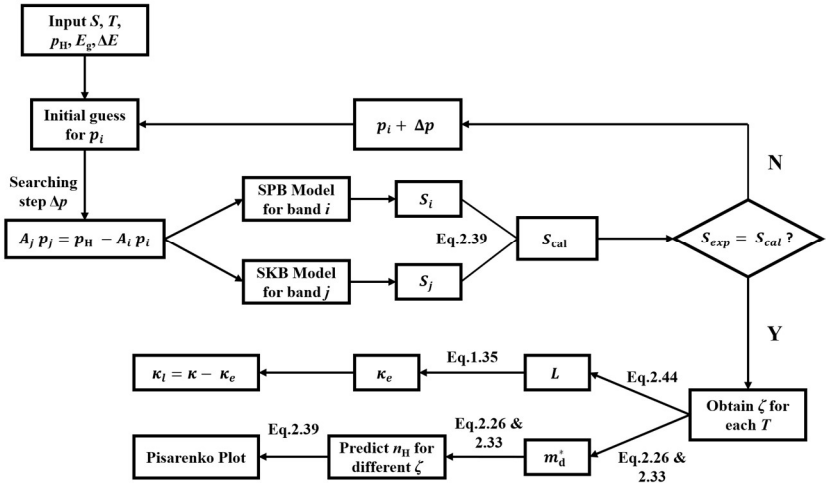

Figure 2.5. Calculation framework for a two-band model with one Kane band and a lower parabolic band.

2.4 Debye – Callaway Model for Lattice Thermal Conductivity

At low temperatures ($\vec{k} \to 0$), the energy dispersion relation for phonons is close to a linear function. If we define the slope (with unit of m/s) of this linear function as a Debye velocity, we have[33]:

$$\omega = \vec{v}_{\mathrm{D}}\vec{k} \tag{2.45}$$

$$D_{\mathrm{ph}}(\hbar\omega) = \frac{3(\hbar\omega)^2}{2\pi^2(\hbar\vec{v}_{\mathrm{D}})^3} \tag{2.46}$$

$$M_{\mathrm{ph}}(\hbar\omega) = \frac{3(\hbar\omega)^2 A}{2\pi^2\hbar\vec{v}_{\mathrm{D}}^2} \tag{2.47}$$

The Debye model can be understood as an analogue of effective mass model for electron dispersion relation where the bottom (top) of the energy band is approximated as a parabola (**Figure 2.6** (a)). The effective mass approximation works well in semiconductor materials, because only electrons a few $k_{\mathrm{B}}T$ away from the band edges determine the transport properties. The typical band width of electron energy dispersion relation can be as high as a few eV, as a result, the variation of the band shape is slow near the band edge, making the effective mass approximation relatively accurate. However, the typical band width for an acoustic phonon branch is around a few $k_{\mathrm{B}}T$, as shown in **Figure 2.6** (b). Consequently, the theoretical curve deviates from the actual dispersion relationship way faster than expected from the effective mass approximation. It is expected that, because of the significant deviation near the Brillouin zone boundary, the calculated total number of states will be much higher than the actual value. To solve this problem, a cutoff frequency ω_{D} is introduced into the integral such that

$$\int_0^{\hbar\omega_D} D_{ph}(\hbar\omega) = \frac{3(\hbar\omega)^2}{2\pi^2(\hbar\vec{v}_D)^3} = 3\frac{N}{\Omega} \tag{2.48}$$

Substituting Eq. (2.45) ~ (2.48) into Eq. (1.42) and assuming acoustic phonon contributes to most of the thermal conductivity, we eventually have

$$k_l = \frac{k_B}{2\pi^2 v_s}\left(\frac{k_B T}{\hbar}\right)^3 \int_0^{\frac{T_D}{T}} \tau_{tot}(x)\frac{x^4 e^x}{(e^x-1)^2}dx \tag{2.49}$$

$$T_D = \left(\frac{6\pi^2}{NV_{av}}\right)^{1/3}\frac{\hbar v_s}{k_B} \tag{2.50}$$

$$x = \hbar\omega/k_B T \tag{2.51}$$

Where T_D is the Debye temperature, v_s is the bulk sound velocity which could be directly measured, x is the reduced energy, N is the number of atoms per unit cell, V_{av} is the average volume for each atom, and $\tau_{tot}(x)$ is the energy dependent phonon relaxation time.

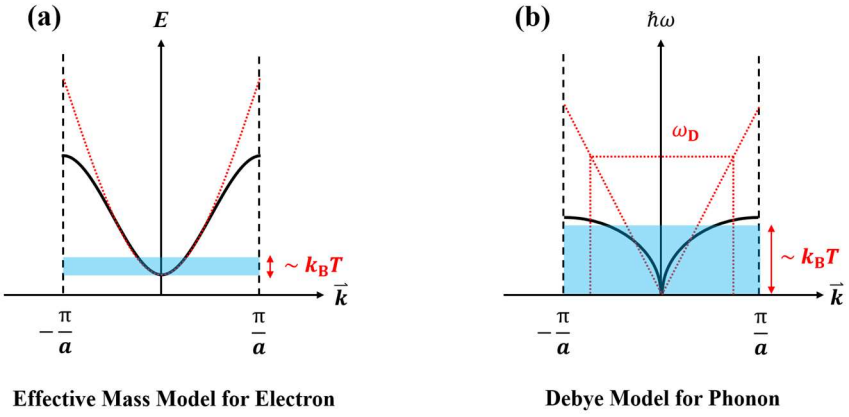

Figure 2.6 (a) Effective mass model. (b) Debye model.

The discussion of phonon scattering is beyond the scope of this thesis, here we directly provide the mostly used equations for various scattering mechanisms:

$$\tau_{\mathrm{tot}}^{-1} = \tau_{\mathrm{U}}^{-1} + \tau_{\mathrm{N}}^{-1} + \tau_{\mathrm{B}}^{-1} + \tau_{\mathrm{PD}}^{-1} + \tau_{\mathrm{P}}^{-1} \tag{2.52}$$

$$\tau_{\mathrm{U}}^{-1} = \frac{2k_B^3 V_{av}^{1/3} \gamma^2 T^3}{(6\pi^2)^{1/3} M_{av} v_s^3 h^2} x^2 exp\left(-\frac{\theta_a}{3T}\right) \tag{2.53}$$

$$\tau_{\mathrm{N}}^{-1} = B_{\mathrm{N}} \tau_{\mathrm{U}}^{-1} \tag{2.54}$$

$$\tau_{\mathrm{B}}^{-1} = \frac{v_{\mathrm{s}}}{D} \tag{2.55}$$

$$\tau_{\mathrm{PD}}^{-1} = \frac{V_{\mathrm{av}} \Gamma}{4\pi v_{\mathrm{s}}^3} \left(\frac{k_{\mathrm{B}} T}{h}\right)^4 x^4 \tag{2.56}$$

$$\tau_P^{-1} = v_{\mathrm{s}} \left[(2\pi R^2)^{-1} + \left(\pi R^2 \frac{4}{9} \left(\frac{\Delta\rho}{\rho}\right)^2 \left(\frac{x k_{\mathrm{B}} T R}{\hbar v_{\mathrm{s}}}\right)^4\right)^{-1}\right]^{-1} N_P \tag{2.57}$$

$$\gamma = \frac{3}{2}\left(\frac{1+v_{\mathrm{p}}}{2-3v_{\mathrm{p}}}\right) \tag{2.58}$$

$$v_{\mathrm{p}} = \frac{1-2(v_{\mathrm{t}}/v_{\mathrm{l}})^2}{2-2(v_{\mathrm{t}}/v_{\mathrm{l}})^2} \tag{2.59}$$

Where τ_{U}^{-1}, τ_{N}^{-1}, τ_{PD}^{-1} , τ_{B}^{-1} and τ_{P}^{-1} are the scattering rate of Umklapp process (U), normal process (N), point defect scattering (PD), grain boundary scattering (B) and precipitation scattering (P), respectively. γ is the Grüneisen parameter, v_{p} is the Poisson ratio, B_{N} is the fitting coefficient (here we assume a simple linear relation between the U and N process), D is the grain size. Γ is the structure contrast parameter, which consists of the mass contrast Γ_{M} and size contrast Γ_{S} between the dopant and host atoms:

$$\Gamma = \Gamma_M + \Gamma_S \tag{2.60}$$

$$\Gamma_M = \sum_i c_i \left(\frac{\bar{M}_i}{\bar{\bar{M}}}\right)^2 \sum_j f_j \left(1 - \frac{m_j^i}{\bar{M}_i}\right)^2 \tag{2.61}$$

$$\Gamma_S = \sum_i c_i \left(\frac{\bar{r}_i}{\bar{\bar{r}}}\right)^2 \sum_j f_j \left(1 - \frac{r_j^i}{\bar{r}_i}\right)^2 \tag{2.62}$$

$\bar{M}_i$ is the average mass for the i^{th} sublattice, $\bar{\bar{M}}$ is the average atomic mass, f_j is the j^{th} atomic fraction, m_j^i is the atomic mass of the j^{th} atom. $\bar{r}_i$ is the average size for the i^{th} sublattice, $\bar{\bar{r}}$ is the average atomic size, and r_j^i is the atomic size of the j^{th} atom.

Chapter 3: Characterization of Thermoelectric Properties

3.1 Crystal Structure

3.1.1 Fundamentals of X-ray Diffraction

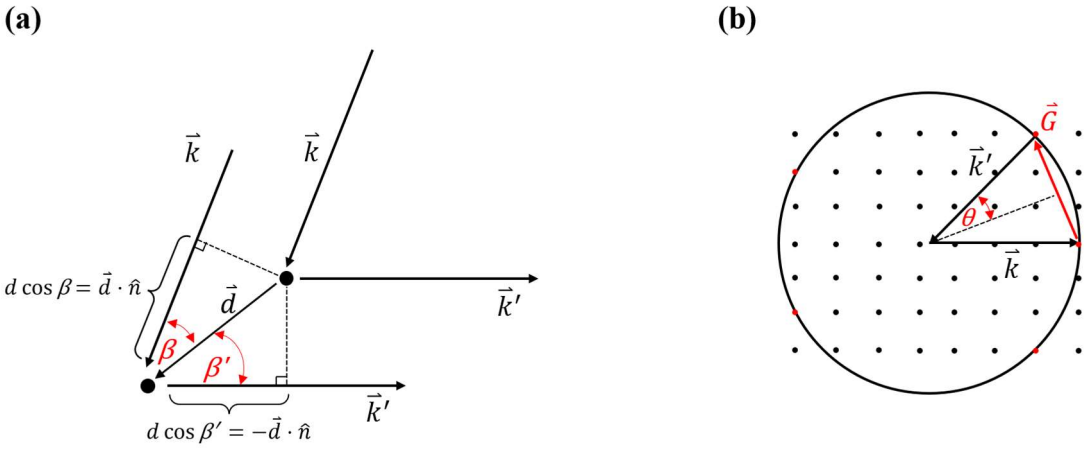

Figure 3.1 (a) The sketch of the X-ray scattering by two points separated by *d*. (b) Ewald's sphere geometry. The sphere has the radius of $|\vec{k}|$. The red spots represent the reciprocal lattice points which satisfy the diffraction condition.

To describe the periodicity of the crystal structure, we first give the definition of ***Bravais lattice***: A Bravais lattice is a collection of points with position vectors $\vec{R}$ in the form of

$$\vec{R} = n_1\vec{a}_1 + n_2\vec{a}_2 + n_3\vec{a}_3 \tag{3.1}$$

Where $\vec{a}_1$, $\vec{a}_2$ and $\vec{a}_3$ are three vectors that are not linear correlated with each other and n_1, n_2 and n_3 are integers. The unit cell vectors, $\vec{a}_i$, of a Bravais lattice are also called primitive vectors. By applying all symmetry operations to a set of primitive vectors, the crystal structure can be generated. Assume a beam with the wavelength λ is incident along a

direction $\hat{n}$, with a wave vector of $\vec{k} = \frac{2\pi\hat{n}}{\lambda}$. After being elastically scattered in the direction $\hat{n}'$, the corresponding wave vector becomes $\vec{k}' = \frac{2\pi\hat{n}'}{\lambda}$, as shown in **Figure 3.1** (a). The path difference between beams that being scattered by two random points separated by *d* is given by

$$d\cos\beta + d\cos\beta' = \vec{d}\cdot(\hat{n} - \hat{n}') \tag{3.2}$$

When the path difference is the integer multiple of the wavelength of the incident beam the scattered beams will constructively interfere with each other this is mathematically given by

$$\vec{d}\cdot(\hat{n} - \hat{n}') = m\lambda \tag{3.3}$$

Multiply both side with $2\pi/\lambda$, we have

$$\vec{d}\cdot(\vec{k} - \vec{k}') = 2\pi m \tag{3.4}$$

If we want to study the interaction between the incident beam and the whole crystal lattice, we simply replace $\vec{d}$ with $\vec{R}$.

$$\vec{R}\cdot(\vec{k} - \vec{k}') = 2\pi m \tag{3.5}$$

Note that $\vec{R}$ is a collection of ***Bravais lattice*** vectors, this equation describes the interference between series of scattered beams. Mathematically, the above equation is equivalent to

$$e^{i(\vec{k}-\vec{k}')\cdot\vec{R}} = 1 \tag{3.6}$$

Define the change in wave vector as $\vec{G} = \vec{k} - \vec{k}'$, the constructive interference only happens when $\vec{G}$ satisfies the above condition, which is known as the von Laue condition. Therefore, it is easier to study the diffraction in a space which generated by $\vec{G}$ vectors. This new vector space is known as the ***reciprocal space***, it has the following relation with the real space:

$$\begin{aligned} \vec{b}_1 &= 2\pi \frac{\vec{a}_2 \times \vec{a}_3}{\vec{a}_1 \cdot (\vec{a}_2 \times \vec{a}_3)} \\ \vec{b}_2 &= 2\pi \frac{\vec{a}_3 \times \vec{a}_1}{\vec{a}_1 \cdot (\vec{a}_2 \times \vec{a}_3)} \\ \vec{b}_3 &= 2\pi \frac{\vec{a}_1 \times \vec{a}_2}{\vec{a}_1 \cdot (\vec{a}_2 \times \vec{a}_3)} \end{aligned} \tag{3.7}$$

Where $\vec{b}_1$, $\vec{b}_2$and $\vec{b}_3$ are reciprocal primitive vectors. Each real space Bravais lattice will have a corresponding Bravais lattice in the reciprocal space (i.e. the FCC real space Bravais lattice has a BCC reciprocal space Bravais lattice. We name $\vec{G}$ as reciprocal lattice vector.

Since we assume elastic scattering, $\left|\vec{k}\right| = \left|\vec{k}'\right|$. Therefore, the incident vector and scattered vector satisfy the Ewald's geometry, which is presented in **Figure 3.1** (b). Intuitively, we have

$$\left|\vec{k}\right| \sin\theta = \frac{1}{2}\left|\vec{G}\right| \tag{3.8}$$

Multiply both side with $\left|\vec{R}\right|$,

$$2\frac{2\pi}{\lambda} d \sin\theta = 2\pi m \rightarrow 2d \sin\theta = m\lambda \tag{3.9}$$

Eq. (3.9) is the Bragg's law. This equation directly connects the diffraction angle with the crystal structure – the interplanar distance *d*. In the meantime, this equation also indicates

that, to capture the crystallographic information, the wavelength of the incident beam must be comparable with d (~ Å). One of such waves is X-ray (0.01 ~ 10nm).

3.1.2 Intensity of X-ray Diffraction

Since X-ray is an electromagnetic wave, apart from being scattered by nuclei, it will also be scattered by the electron cloud. The electrons distribution can be described by the electron density function $\rho(\vec{r})$, where $\vec{r}$ is a real space vector. For a perfect crystal with no defects, the electron density function will have the periodicity of the lattice. Therefore, we only need to study the scattering within one unit cell. For consistency with the previous discussion, we also convert $\rho(\vec{r})$ into reciprocal space. This can be done by performing Fourier transform:

$$\rho(\vec{r}) = \sum_{\vec{G}} \rho_{\mathrm{G}} e^{i\vec{G}\cdot\vec{r}} \rightarrow \rho_{\mathrm{G}} = \frac{1}{\Omega}\int_{\mathrm{cell}} \rho(\vec{r}) e^{-i\vec{G}\cdot\vec{r}} dV \tag{3.10}$$

Where ρ_{G} is the electron distribution function in the reciprocal space, Ω is the volume of the unit cell. Again, $\vec{k}$ is the wave vector of the incident X-ray and $\vec{k}'$ is the wave vector after the scattering. The resulting amplitude from the interference is given by

$$F = \int \left\langle e^{i\vec{k}\cdot\vec{r}} \middle| \rho(\vec{r}) \middle| e^{i\vec{k}'\cdot\vec{r}} \right\rangle dV = \sum_{\vec{G}} \rho_{\mathrm{G}} \int e^{i(\vec{G}-\vec{g})\cdot\vec{r}} \tag{3.11}$$

Notice that, F integrated through the whole space. Based on the von Laue condition, when $\vec{g}$ is also a reciprocal lattice vector, $F = V_{\mathrm{total}}\,\rho_{\mathrm{G}}$, otherwise, $F = 0$. Since the crystal is perfectly periodic, we have

$$F = NS_{\mathrm{G}} \tag{3.12}$$

$$S_{\mathrm{G}} = \int_{\mathrm{cell}} e^{-i\vec{G}\cdot\vec{r}} dV = \Omega\, \rho_{\mathrm{G}} \tag{3.13}$$

Where S_{G} is the amplitude contributed by one unit cell and is known as the structure factor, N is the total number of unit cells. For a basis with s atoms, the electron density can be written as

$$\rho(\vec{r}) = \sum_{j=1}^{s} \rho_j\left(\vec{r} - \vec{r}_j\right) \tag{3.14}$$

Where $\vec{r} - \vec{r}_j$ is the position of the j^{th} atom. Substituting Eq. (3.14) into (3.13), we have

$$S_{\mathrm{G}} = \sum_{j=1}^{s} \int_{\mathrm{cell}} \rho_j\left(\vec{r} - \vec{r}_j\right) e^{-i\vec{G}\cdot\vec{r}} dV \tag{3.15}$$

By defining $\vec{d}_j = \vec{r} - \vec{r}_j$, we rewrite the above equation

$$S_{\mathrm{G}} = \sum_{j=1}^{s} e^{-i\vec{G}\cdot\vec{r}_j} \int_{\mathrm{cell}} \rho_j\left(\vec{d}_j\right) e^{-i\vec{G}\cdot\vec{d}_j} dV = \sum_{j=1}^{s} e^{-i\vec{G}\cdot\vec{r}_j} f_j(\vec{G}) \tag{3.16}$$

Where $f_j(\vec{G})$ only relates to the nature of the j^{th} atom, which is known as the atomic form factor. It describes the scattering effect contributed by the electron cloud of a given element. Now we focus on the first term $\sum_{j=1}^{s} e^{-i\vec{G}\cdot\vec{r}_j}$. For a reciprocal lattice vector $\vec{G} = h\vec{b}_1 + k\vec{b}_2 + l\vec{b}_3$, and for a real space vector $\vec{r}_j = x_j\vec{a}_1 + y_j\vec{a}_2 + z_j\vec{a}_3$, we have

$$\sum_{j=1}^{s} e^{-i\vec{G}\cdot\vec{r}_j} = \sum_{j=1}^{s} e^{-2\pi i(hx_j + ky_j + lz_j)} \tag{3.17}$$

In case of a rock-salt structure consisting of only one element with the basis A (0,0,0) and B(a/2,0,0), we have

$$\sum_{j=1}^{s} e^{-i\vec{G}\cdot\vec{r}_j} = [(-1)^{h+k} + (-1)^{k+l} + (-1)^{h+l}] \tag{3.18}$$

As can be seen, when h, k and l are mixed with even and odd number, the corresponding amplitude $F_{hkl} = 0$. This symmetry induced absence of diffraction is called ***systematic extinction***.

3.1.3 Powder XRD

Assume an orthogonal unit cell, its cell vectors are $\begin{bmatrix} a & 0 & 0 \\ 0 & b & 0 \\ 0 & 0 & c \end{bmatrix}$. Based on **Eq.** (3.7), the corresponding reciprocal lattice vectors are given by

$$\begin{bmatrix} \frac{2\pi}{a} & 0 & 0 \\ 0 & \frac{2\pi}{b} & 0 \\ 0 & 0 & \frac{2\pi}{c} \end{bmatrix} = \begin{bmatrix} \frac{2\pi}{a^2} & 0 & 0 \\ 0 & \frac{2\pi}{b^2} & 0 \\ 0 & 0 & \frac{2\pi}{c^2} \end{bmatrix} \begin{bmatrix} a & 0 & 0 \\ 0 & b & 0 \\ 0 & 0 & c \end{bmatrix} \tag{3.19}$$

Define the matrix $\begin{bmatrix} \frac{2\pi}{a^2} & 0 & 0 \\ 0 & \frac{2\pi}{b^2} & 0 \\ 0 & 0 & \frac{2\pi}{c^2} \end{bmatrix}$ as the reciprocal operator $\hat{g}$. If we now rotate the real space lattice by a random space angle (α, β, γ), the corresponding reciprocal lattice will be given by

$$\hat{g}\left(\begin{bmatrix} a & 0 & 0 \\ 0 & b & 0 \\ 0 & 0 & c \end{bmatrix} \hat{r}\right) = \left(\hat{g}\begin{bmatrix} a & 0 & 0 \\ 0 & b & 0 \\ 0 & 0 & c \end{bmatrix}\right)\hat{r} = \begin{bmatrix} \frac{2\pi}{a} & 0 & 0 \\ 0 & \frac{2\pi}{b} & 0 \\ 0 & 0 & \frac{2\pi}{c} \end{bmatrix} \hat{r} \tag{3.20}$$

Where $\hat{r}$ is the rotational matrix. The above equation indicates that if we rotate the real space lattice, the corresponding reciprocal lattice will also be rotated in the exact same way.

In a powder (or polycrystalline) sample, different grains point at different orientation. When shinning X-ray onto the sample, a huge number of grains will participate

in diffraction. If we assume there is no preferred orientation (texturing), then there is equal possibility for the crystals to point in any directions. Consequently, the 2D Ewald's circle in Figure 3.1 (a) will now become a 3D Ewald's sphere and all the reciprocal lattice points will also form a sphere around the origin (randomly defined). The intersection between the Ewald sphere and all the reciprocal spheres all satisfies the diffraction condition and each reflection ring can be indexed by a particular reflection angle. Combined with previous sections we see that a given crystal structure will exhibits a unique set of diffraction peaks located at different angles with certain diffraction intensity. We call this set of diffraction peaks an ***XRD pattern*** of the crystal. By measuring the pattern for a given sample, we are able to identify its crystal structure and even composition.

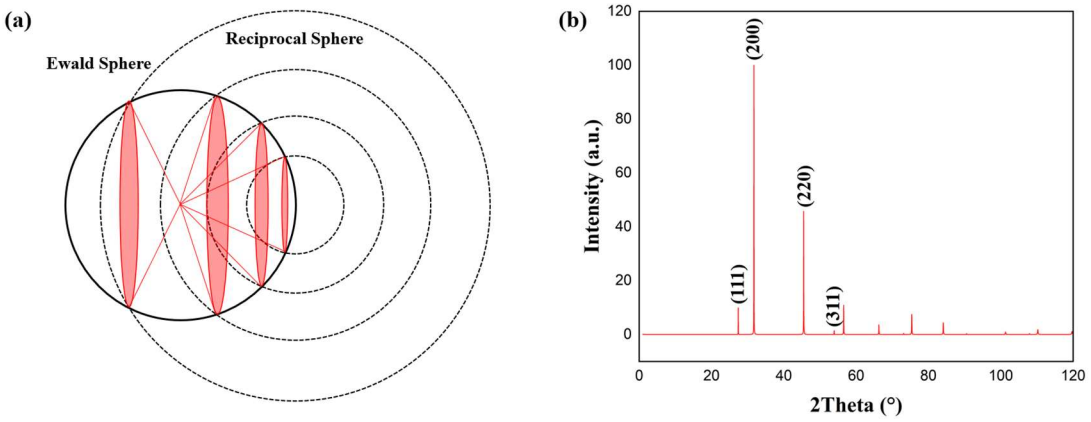

Figure 3.2 (a) Formation of powder diffraction rings. (b) A XRD pattern for the NaCl sample.

3.1.4 Instrumentation

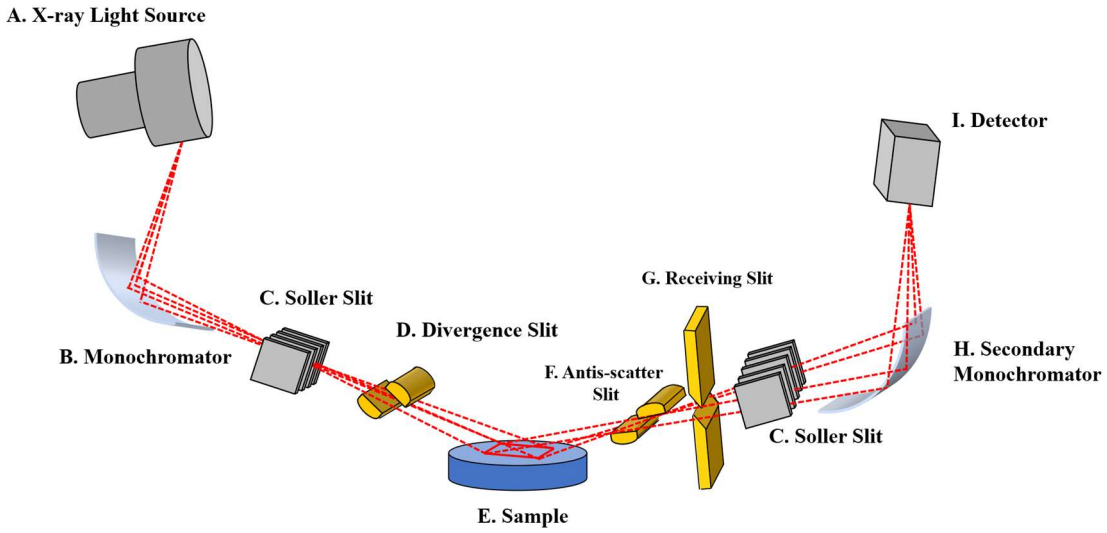

Figure 3.3 Structure of a typical powder XRD instrument. The red dash lines indicate the optical path of the X-ray beam.

To perform XRD, a highly monochromatic X-ray light source is essential. **Figure 3.3** shows the shows the typical structure of a powder X-ray diffraction instrument, each of the components will be briefly introduced.

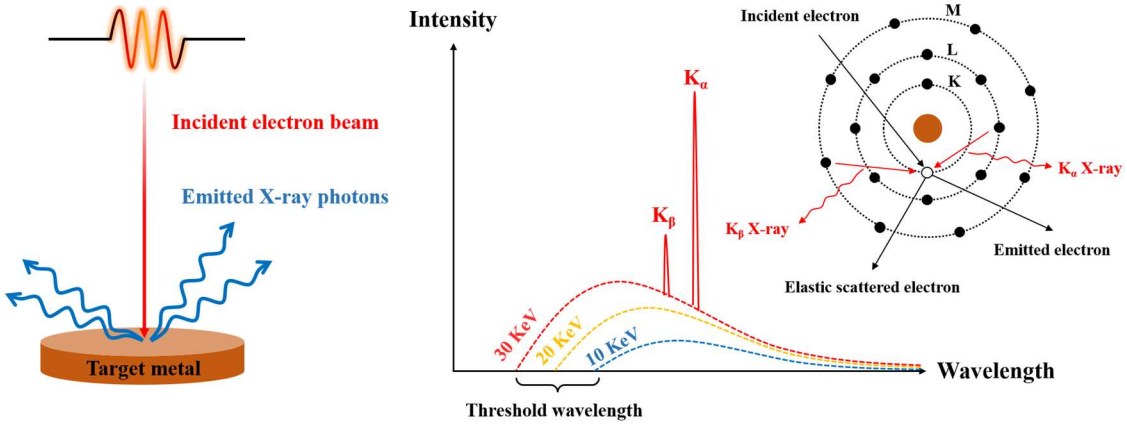

Figure 3.4 The X-ray light source.

X-ray Light Source: When an accelerated electron hit the surface of the target metal, the kinetic energy of the electron will convert into photons or dissipates as heat. Since the energy conversion rate is random, the wavelength of the emitted photons will be a distribution function (white radiation). When the energy of the incident electron is high enough, the inner electrons of the target metal may be "knocked away", leaving an empty energy state behind. The outer shell electrons will spontaneously fill up the empty state and emit X-ray photons. Since the energy for each orbital are constant, these emitted X-ray photons show high monochromaticity and intensity which is known as the characteristic X-ray. By extracting these signals from the background noise, a high-quality X-ray beam can be obtained.

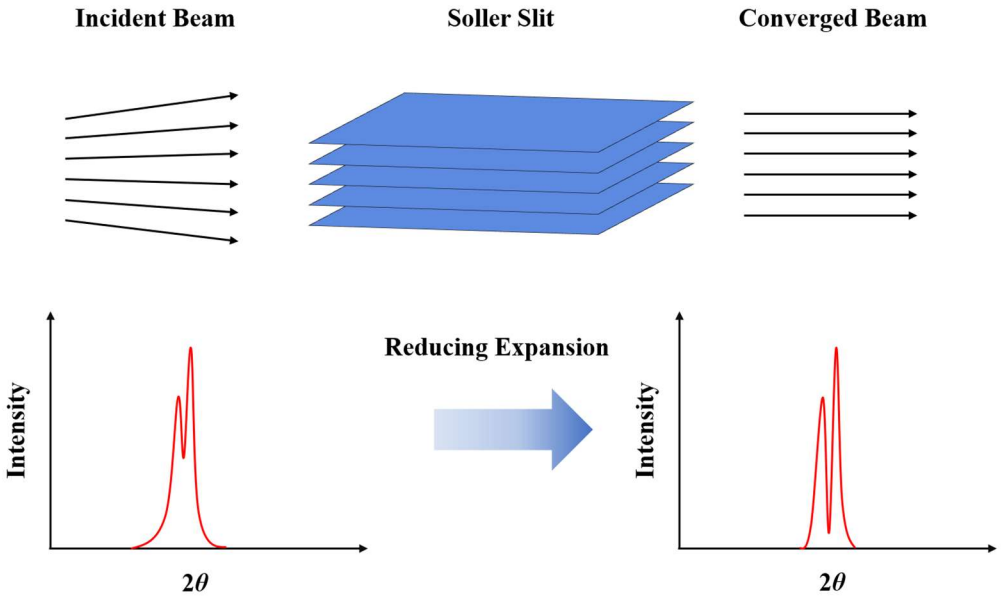

Figure 3.5 Effect of a Soller slit on the diffraction pattern.

Soller Slits: **Figure 3.5** shows the sketch of a Soller slit. It reduces the divergence of the incident beam in the direction normal to the plane, in which the diffraction intensity is

measured. This will reduce the angle expansion of the diffraction peaks, making it easier to distinguish the peaks which are close to each other.

Divergence Slit: The divergence slit, controls the aperture of the incident beam, which limits the illumination area onto the sample. The geometry of the divergence slit is shown in **Figure 3.6** (a). The illumination area L is given by

$$l_1 = \frac{R}{\sin\left(\theta+\frac{\varphi}{2}\right)}\sin\left(\frac{\varphi}{2}\right) \tag{3.21}$$

$$l_2 = \frac{R}{\sin\left(\theta-\frac{\varphi}{2}\right)}\sin\left(\frac{\varphi}{2}\right) \tag{3.22}$$

$$L = l_1 + l_2 \tag{3.23}$$

Where φ is the aperture of the incident beam, which is controlled by the size of divergence slit, θ is the diffraction angle, L is the length of the illumination area, as shown in **Figure 3.6** (b). Increasing the illumination area can improve the signal intensity, but at the same time, when the illumination area goes beyond sample surface and directly acting on the sample holder, extra background noise will be introduced.

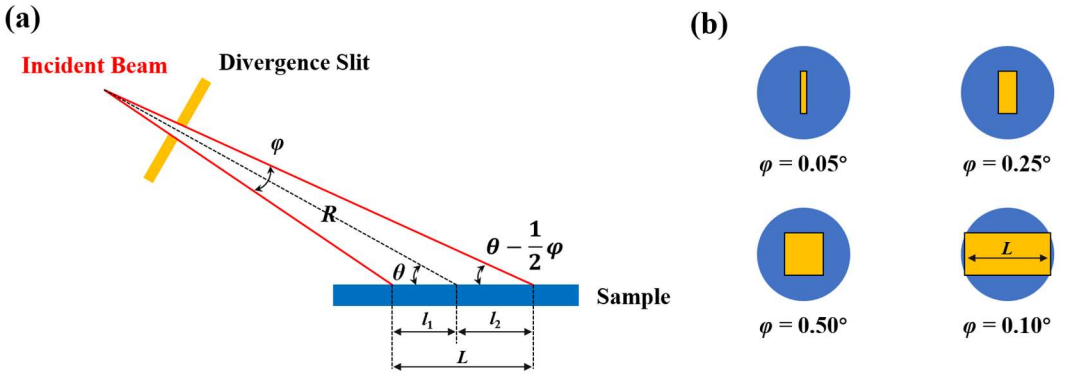

Figure 3.6 (a) Divergence slit geometry. (b) The illumination area from different slit sizes under the same diffraction angle[34].

Monochromator: Although the K_β X-ray can be easily removed by filter, the undesired $K_{\alpha 2}$ is difficult to eliminate, as shown in **Figure 3.7** (a). To further improve the monochromaticity of the X-ray beam, a monochromator is usually added in between the X-ray tube and sample. Nowadays, the most widely used monochromator is the crystal monochromator (CM) which uses Bragg's law to separate X-rays with different wavelength. For a Cu light source, a Ge CM is used. The incident beam ($K_{\alpha 1} + K_{\alpha 2}$) is diffracted by (111) plane of Ge. Due to the different wavelength of $K_{\alpha 1}$ and $K_{\alpha 2}$, only $K_{\alpha 1}$ will satisfy the diffraction condition. Thus, through this process, a highly monochromatic X-ray could be obtained.

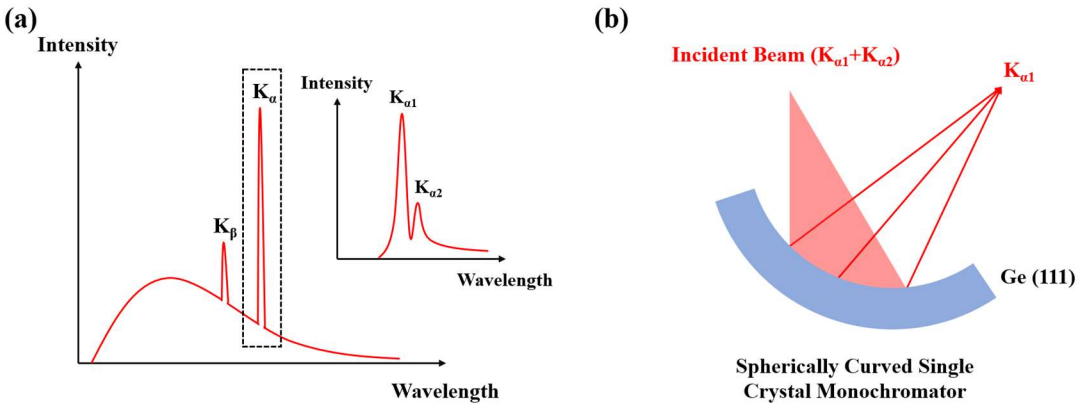

Figure 3.7 (a) K_α and K_β characteristic X-ray. Although K_β is well separated with K_α series in wavelength, $K_{\alpha 1}$ and $K_{\alpha 2}$ are extremely close to each other, making it impossible to directly filter out the undesired $K_{\alpha 2}$. (b) Ge single crystal monochromator.

3.2 Temperature-dependent Resistivity and Seebeck coefficient Measurement

The Seebeck coefficient and electrical resistivity can be measured on a ZEM-3 instrument, following the procedure in patents JSR I 1650-1 and JSR I 1650-2[35]. The measurements setups are presented in **Figure 3.8**. When measuring the Seebeck coefficient, the temperature gradient is established inside the sample by controlling the temperature of the upper and lower furnace. Two pairs of thermocouples are attached to the hot and cold part of the sample, as shown in **Figure 3. 8** (a). The voltage induced by the Seebeck coefficient is given by

$$V = \int_{T_2}^{T_1} (S_{\text{sample}} - S_{\text{wire}}) dT \tag{3.24}$$

Here T_1 is the hot side temperature, T_2 is the cold side temperature, S_{sample} is the Seebeck coefficient of the sample and S_{wire} is the Seebeck coefficient of the wire. Since the temperature difference between the two contacts are normally very small (less than 5K), S_{sample} and S_{wire} are treated as temperature independent. By measuring the voltage between the two contacts, the Seebeck coefficient can be calculated as

$$S_{\text{sample}} = \frac{V}{T_1 - T_2} + S_{\text{wire}} \tag{3.25}$$

The resistivity of the sample is measured by applying a steady electric current through the sample, as shown in **Figure 3.8** (b). After bringing the sample to equilibrium, the voltage between the two contacts is measured again, and the resistivity is given by the following equations

$$R = \frac{V}{I} \tag{3.26}$$

$$\rho = R\frac{A}{d} \tag{3.27}$$

Where A is the intersection of the sample, d is the distance between two contacts.

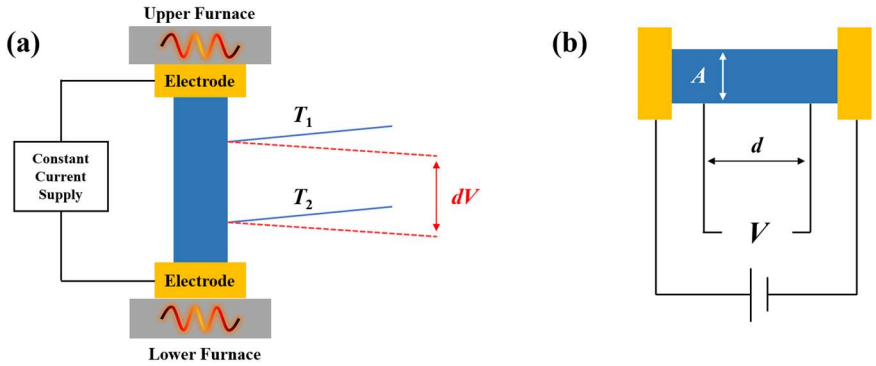

Figure 3.8 Measurements setups of ZEM-3 for (a) Seebeck coefficient and (b) resistivity.

3.3 Determination of the Carrier Concentration

In Chapter 2, we show that the transport properties of the material can be simulated by solving the transport equations. This requires knowledge of the position of the Fermi level. For a material with a simple band structure i.e., SnTe, E_f can be determined by fitting the experimental Seebeck coefficient. However, **Eq**. (2.26) and (2.34) indicates that, to calculate the effective mass, the knowledge of the carrier concentration is required. Moreover, most of the promising TE materials have complex band structures, thus the multi-band model is used to simulate their properties, which also requires the knowledge of their carrier concentration.

3.3.1 Hall Effect

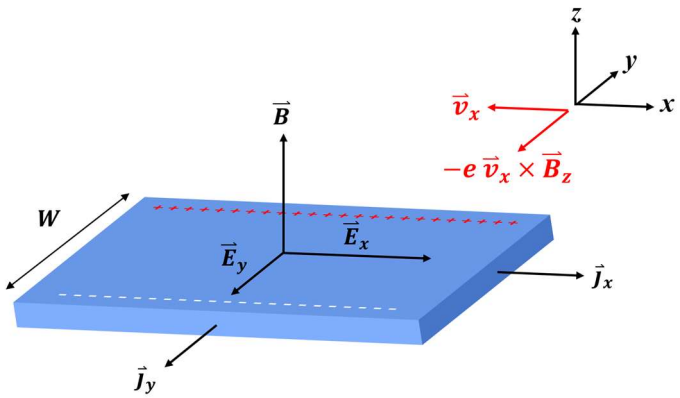

Figure 3.9 Hall effect.

For simplicity, we will use the classical Drude model to derive the Hall effect equations. Under external electric $\vec{E}$ and magnetic $\vec{B}$ fields the equation of motion is given by[16]

$$\frac{d\vec{p}}{dt} = -e\vec{E} - \frac{\vec{p}}{m}e \times \vec{B} - \frac{1}{\tau}\vec{p}(t) \tag{3.28}$$

Where p is the momentum of the electron and τ is the relaxation time. The third term is the damping term caused by collisions. Assuming the electric field is orthogonal with the electric field (as shown in **Figure 3.9**), when the equilibrium is established, we have the following relation

$$\frac{dp_x}{dt} = -eE_x - \frac{eB}{m}p_y - \frac{1}{\tau}p_x = 0 \tag{3.29}$$

$$\frac{dp_y}{dt} = -eE_y + \frac{eB}{m}p_x - \frac{1}{\tau}p_y = 0 \tag{3.30}$$

Multiply both sides by $-ne\tau/m$, (m is the free electron mass) we have

$$\sigma_0 E_x = \frac{eB}{m}\tau j_y + j_x \tag{3.31}$$

$$\sigma_0 E_y = -\frac{eB}{m}\tau j_x + j_y \tag{3.32}$$

Where σ_0 is the Drude DC conductivity, n is the carrier concentration, j_x and j_y are the current density along *x* and *y* direction, respectively. When the equilibrium is established, $j_y = 0$

$$E_y = -\left(\frac{eB\tau}{\sigma_0 m}\right) j_x = -\left(\frac{B}{ne}\right) j_x \tag{3.33}$$

Practically, the voltage which transverse to the inject electric current is measured, which is known as the Hall voltage $V_{\mathrm{H}} = WE_y$. Define Hall coefficient R_{H} as

$$R_{\mathrm{H}} = -\frac{1}{ne} = -\frac{A_{\mathrm{H}}}{n_{\mathrm{H}} e} \tag{3.34}$$

n_{H} is the Hall carrier concentration. It should be noted that the Hall carrier concentration is different with the actual carrier concentration by a factor of A_{H}, which is the Hall constant, determined by Eq. (2.27) and (2.35). The above equation shows that, the carrier concentration of the sample can be directly obtained via Hall effect. To also obtain the mobility μ_{H}, one can use the following equation

$$\mu_{\mathrm{H}} = R_{\mathrm{H}}\sigma_0 = -\frac{1}{ne}\frac{ne^2\tau}{m} = -\frac{e\tau}{m} \tag{3.35}$$

Therefore, the conductivity (or resistivity) of the sample will have to be measured.

3.3.2 van der Pauw Geometry

Assuming an infinite half-plane sheet with thickness of *t*. Four points 1, 2, 3 and 4 are located at the edge of the sheet and the distances are *a*, *b* and *c*, as shown in **Figure 3.10**.

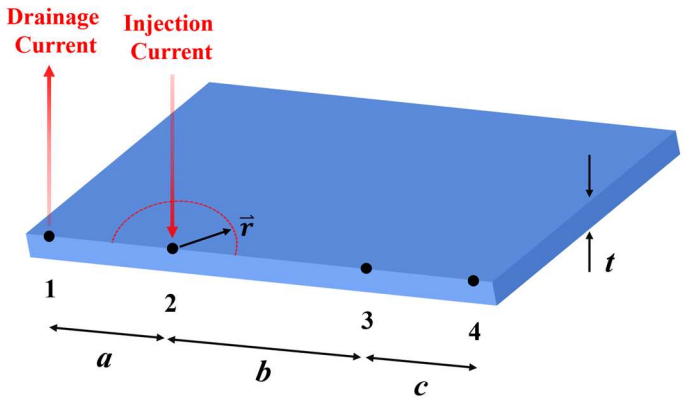

Figure 3.10 Infinite half-plane sheet model[36].

A current *I* inject from point 2, at a distance *r* from point 2, the current density is given by

$$\vec{J} = \frac{I}{\pi r t}\hat{r} \tag{3.36}$$

Where $\hat{r}$ is the radical primitive vector. Based on Ohm's law, the radical electric field is then given by

$$\vec{E} = \rho\vec{J} = \frac{\rho I}{\pi r t}\hat{r} \tag{3.37}$$

Here, ρ is the resistivity of the sheet. The voltage between point 4 and 3 induced by the injection current is

$$(V_3 - V_4)_{\text{in}} = -\int_4^3 \vec{E}\, d\vec{r} = -\frac{\rho I}{\pi t}\ln\left(\frac{a+b+c}{a+b}\right) \tag{3.38}$$

If the current is then drained from point 1, the voltage between point 3 and 4 induced by the drainage current is given by

$$(V_3 - V_4)_{\text{out}} = -\int_4^3 \vec{E}\, d\vec{r} = \frac{\rho I}{\pi t} \ln\left(\frac{b+c}{c}\right) \tag{3.39}$$

The total current is finally given by

$$(V_3 - V_4)_{\text{total}} = (V_3 - V_4)_{\text{in}} + (V_3 - V_4)_{\text{out}} = \frac{\rho I}{\pi t} \ln\left[\frac{(b+c)(a+b)}{b(a+b+c)}\right] \tag{3.40}$$

Define $R_{21,34}$ as the resistance being measured between point 3 and 4, when injecting the current at point 2 and draining the current at point 1.

$$R_{21,34} = \frac{V_{34}}{I_{21}} = \frac{\rho}{\pi t} \ln\left[\frac{(b+c)(a+b)}{b(a+b+c)}\right] \tag{3.41}$$

Similarly, by injecting the current at point 4, draining it at point 1, and measuring resistance between point 2 and 3, we have

$$R_{41,23} = \frac{V_{23}}{I_{41}} = \frac{\rho}{\pi t} \ln\left[\frac{ac}{(b+c)(a+b)}\right] \tag{3.42}$$

Combine **Eq**. (3.40) and (3.41), we then find the relation below

$$\exp\left(-\frac{\pi t}{\rho} R_{21,34}\right) + \exp\left(-\frac{\pi t}{\rho} R_{41,23}\right) = 1 \tag{3.43}$$

This is the famous van der Pauw relation[36]. The van der Pauw theorem states that if:

(1) The sheet is homogenous.

(2) With uniform thickness.

(3) Thin enough (can be treated as 2D system).

Eq. (3.43) will always hold regardless of the shape of the sample or the position of the four points.

By manipulating the equations, we can have

$$\exp\left[-\frac{\pi t(R_{21,34}+R_{41,23})}{2\rho}\right]\cosh\left[\frac{\pi t(R_{21,34}-R_{41,23})}{2\rho}\right]=\frac{1}{2} \tag{3.44}$$

Define the quantity *f* as

$$f=\ln 2\frac{2\rho}{\pi t}\frac{1}{R_{21,34}+R_{41,23}} \tag{3.45}$$

Substituting **Eq**. (3.45) into (3.44) we have

$$\exp\left[-\frac{\ln 2}{f}\right]\cosh\left[\frac{R_{21,34}/R_{41,23}-1}{R_{21,34}/R_{41,23}+1}\frac{\ln 2}{f}\right]=\frac{1}{2} \tag{3.46}$$

Eq. (3.46) shows that the value of *f* is solely related to $R_{21,34}/R_{41,23}$, which could be directly measured. By numerically solving *f*, the resistivity ρ could then be calculated via **Eq**. (3.45). Practically, a square sample is used in the Hall measurement, as shown in **Figure 3.11** (a). Because of the symmetry, $R_{21,34}=R_{41,23}$. Thus, ρ is simply given by

$$\rho=\frac{\pi}{\ln 2}\frac{V}{I} \tag{3.47}$$

Therefore, by forcing current *I* through two contacts and measuring the *V* between the other two contacts, the resistivity of the square sheet can be determined.

Using the same geometry, the Hall effect can be also measured. This time, the current will be injected at point 1 and flow through the diagonal of the square and being drained at point 3, **Figure 3.11** (b). By definition, the Hall voltage is given by

$$V_{\mathrm{H}} = \rho \frac{e\tau}{m} B \int_2^4 \vec{j} \cdot \hat{n}\, d\vec{l} \tag{3.48}$$

Where the integration term is the normal component of the current with respect to the 2-4 line. Due to the square symmetry, we can easily have that this is just the total current *I* that injected into the sample. Therefore, we simply have

$$V_{\mathrm{H}} = \rho \frac{e\tau}{m} BI \tag{3.49}$$

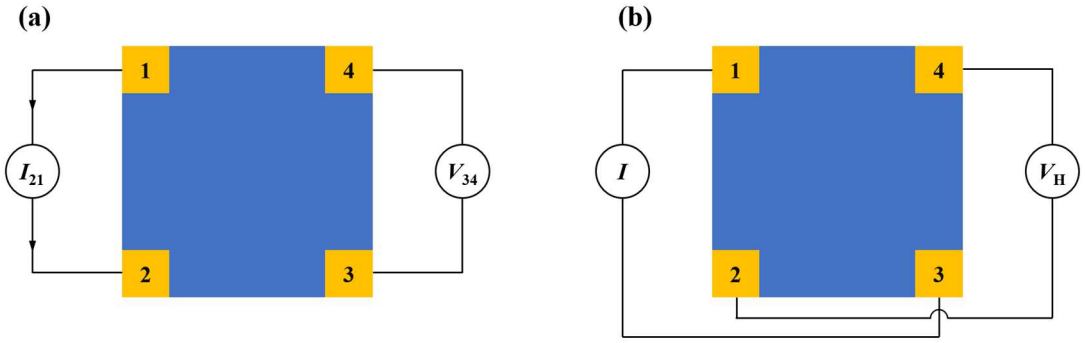

Figure 3.11 van der Pauw geometry. (a) Resistivity measurement setup and (b) Hall effect measurement setup.

During the measurement, the direction of the current will be reversed to eliminate the thermoelectric voltage, and the magnetic field will also be reversed to eliminate the misalignment voltage (resulting from the imperfect contact geometry).

3.4 Total Thermal Conductivity

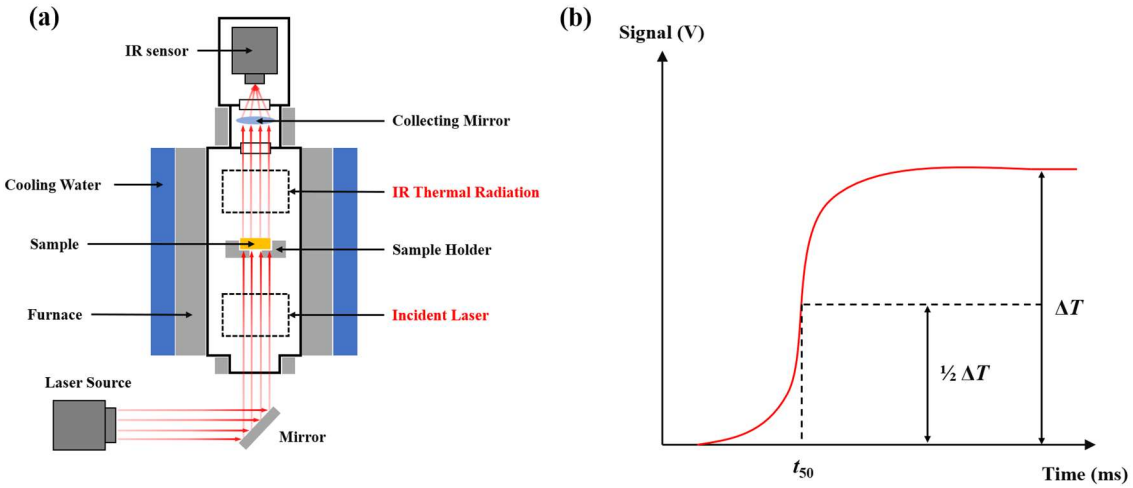

Figure 3.12 (a) Laser flash analysis system. (b) The determination of thermal diffusivity.

The total thermal conductivity can be measured using the laser flash analysis (LFA). A typical LFA system is shown in **Figure 3.12** (a). During the LFA, a laser pulse illuminates the back of the sample and, ideally, uniformly heats up the surface. By measuring the temperature evolution at the opposite side of the sample, the thermal diffusivity can then be measured using the method shown in **Figure 3.12** (b). The thermal diffusivity D is given by

$$D = 0.1388\frac{d^2}{t_{50}} \tag{3.50}$$

Where d is the thickness of the sample, t_{50} is the time which corresponds to the half maximum signal intensity. After obtaining D, the total thermal conductivity is given as[37]

$$\kappa = D\rho C_{\mathrm{P}} \tag{3.51}$$

ρ is the density of the sample, C_P is the constant pressure heat capacity which can be approximated via the Dulong-Petit law.

3.5 Microstructure Analysis

The total thermal conductivity of the material is highly sensitive to its microstructure. To characterize the microstructure, scanning electron microscope (SEM) is commonly used. Unlike the conventional optical microscope which uses visible light for the analysis, SEM uses high energy electron beam. Here, we skip the complex electron optics of the SEM and briefly introduce three widely used imaging techniques – secondary electron (SE) imaging, back scattered electron (BSE) imaging and energy dispersive spectroscopy (EDS), as demonstrated in **Figure 3.13**.

Secondary Electrons: Secondary electrons originate from the inelastic interaction between the host atom and incident electrons. The signal depth of the secondary electrons is ~ 20 nm and is highly sensitive to the surface topography. Due to its small interaction volume, secondary electrons can be used to obtain high-resolution images of the material surface.

Back Scattered Electrons: Back scattered electrons result from the elastic scattering of the incident electrons by the nuclei. The intensity of the BSE is related to the atomic number of the element. The heavier the element, the stronger the BSE signal will be. Thus, BSE image uses atomic number as its contrast. However, due to its relatively large signal depth (~ 0.5 μm) and interaction volume, the resolution of a BSE image is lower than that of an SE image.

Energy Dispersive Spectroscopy: EDS utilizes the characteristic X-ray emission to identify elements. Since each element has a unique electronic configuration, its X-ray emission lines are also unique. Therefore, by collecting the X-ray signal that emitted from the surface, the composition of the sample can be determined. However, it should be noted that the interaction volume of EDS has a diameter of approximately 2 ~ 3 μm, making it less reliable for precise elemental distribution characterization.

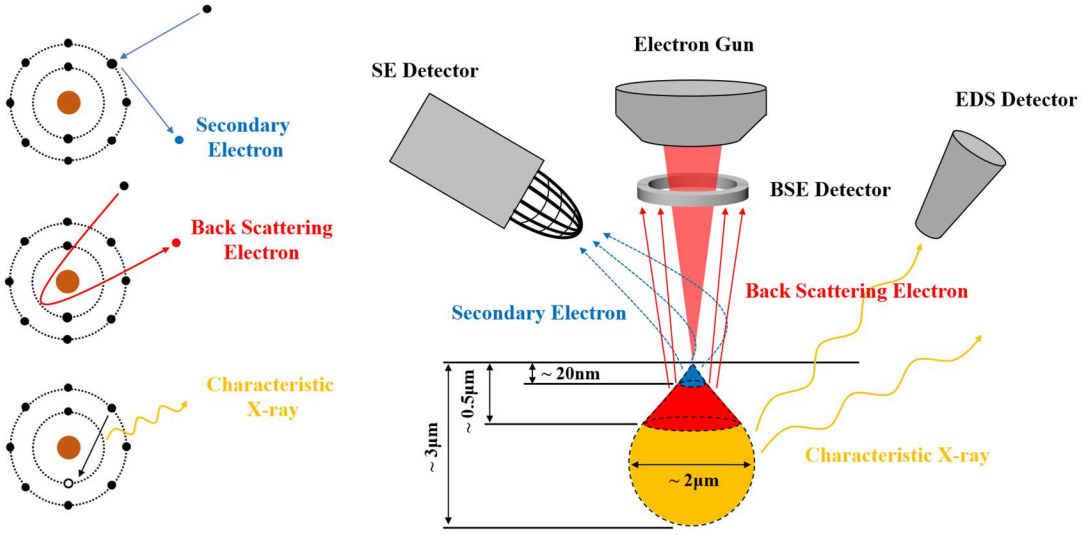

Figure 3.13 Principals of the scanning electron microscope imaging.

Chapter 4 Optimized Electronic Properties and nano-Structural Features for Securing High Thermoelectric Performance in Doped GeTe

4.1 Introduction

Recently, GeTe has received extensive attention in the field of thermoelectrics for its promising TE performance, making it one of the best state-of-the-art TE materials[38–42]. However, due to its high intrinsic carrier concentration and non-ideal electronic band structure, further optimization of its performance has reached a bottleneck. When the temperature reaches 673K or higher, GeTe crystalizes in rock-salt structure *Fm*-3*m* (#225). Upon cooling, the material will undergo a cubic-to-rhombohedral phase transition. As a result, the room-temperature phase of GeTe becomes *R*3*m* (#160). This phase transition is caused by the lone pair effect of the Ge $4s^2$ orbital, which distorted the lattice along the (111) direction and such distortion resulting in low band degeneracy. Based on Mott's equation under degenerate limit and single band picture, the Seebeck coefficient is given by:

$$S = \frac{8\pi^2 k_B^2}{3eh^2} m^* T \left(\frac{\pi}{3n}\right)^{2/3} \quad (4.1)$$

$$m^* = N_V^{2/3} m_b^* \quad (4.2)$$

Where m^* is the density of states (DOS) effective mass, n is the carrier concentration, N_V is the band degeneracy, and m_b^* is the single-band effective mass. The above equations indicate that a material with high band degeneracy in the vicinity of the Fermi energy will be most likely to show a high Seebeck coefficient. The low band degeneracy of

rhombohedral GeTe (R-GeTe) results in poor TE performance in the near-room-temperature range, limiting the overall average zT value of GeTe. **Figure 4.1** (a) shows the Pisarenko plot of R- and C-GeTe at 300K. As can be seen, the curve of R-GeTe is well below C-GeTe, indicating that if the cubic phase could be stabilized to low temperature, the TE performance of GeTe could be improved. Motivated by the above facts, many works have been done to stabilize the cubic phase to room temperature[42–47]. However, those materials are all heavily doped systems with poor carrier mobility, which limits their overall TE performance. An alternative way to increase the band degeneracy is to induce band convergence through doping, but such dopants usually have low solubility in GeTe, resulting in limited performance improvements[45,46,48,49].

In addition to the non-ideal band structure, the lone pair effect also results in the precipitation of Ge atoms which produces a vast amount of Ge vacancies inside the crystal[50]. These vacancies act as acceptor dopants, resulting in a high intrinsic hole carrier concentration of the level of 10^{21} cm^{-3} in pristine GeTe. **Figure 4.1** (b) shows the simulated power factor at room-temperatures based on the relaxation time approximation (here τ was set to be 3.9×10^{-15} s) [51]. The highlighted points belong to pristine GeTe samples which were synthesised by other groups. As can be seen, the intrinsic carrier concentration of GeTe severely deviates from its optimal value.

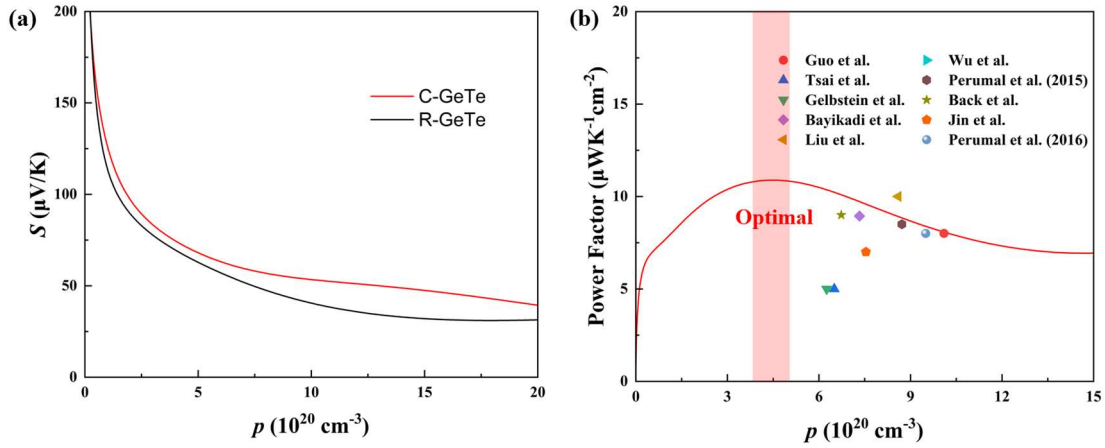

Figure 4.1. (a) Pisarenko plot of C-GeTe and R-GeTe at 300K and (b) Power factor vs. carrier concentration of R-GeTe. Highlighted data points belong to pristine GeTe of previous reports[52–61].

In this work, we optimized the TE performance of GeTe via Bi, Zn and In co-doping. We observed unusual behavior of Zn dopants in the GeTe-based system. The widely studied Bi-doped GeTe was chosen as the base material. Recent works show that doping Bi in different forms (BiTe and Bi_2Te_3) can have very different effects on its thermoelectric properties[57,61]. During the experiment, Zn was doped into the GeTe + 5 mol.% BiTe and GeTe + 3 mol.% Bi_2Te_3, separately. For simplicity, the former will be named as a non-charge balanced (NCB) system and the latter as a charge balanced (CB) system. Hall effect measurement indicates that Zn doping effectively reduces the carrier concentration and density of states (DOS) effective mass in both systems. DFT calculations reveal that such phenomenon originates from the band modification and the relocation of the Fermi level. Meanwhile, the introduction of Zn also suppressed the formation of Ge vacancies (which is also the cause of the reduced carrier concentration), which reduces the carrier scattering

rate and, consequently, secures high carrier mobility. As a result, the power factor of all samples is maintained at a relatively high value. Our powder X-ray diffraction (PXRD) results indicate that the solubility of Zn is less than 4 mol.%, which is lower than the previously reported value of 6 mol.%. Because of such low solubility, nanoscale ZnTe precipitations ranging from 80nm to 500nm were observed in the samples during the STEM analysis. Microstructures including nano twining, defect layers, and "dislocation bands" were also observed. Our geometric phase analysis shows that these defects induce strong strain fluctuations and high lattice anharmonicity, both of which facilitate the suppression of lattice thermal conductivity. Finally, to improve the average *zT* value, 1 mol.% of In was doped onto the Ge site to induce a strong DOS distortion in the vicinity of the Fermi level. As a result, a peak *zT* value of 2.06 and a promising average *zT* value of 1.30 have been achieved in $(Ge_{0.97}Zn_{0.02}In_{0.01}Te)_{0.97}(Bi_2Te_3)_{0.03}$, which is among the state-of-the-art lead-free TE materials.

4.2 Experiment

Sample Preparation: $Ge_{1-x-y-z}Bi_xZn_yIn_zTe$ (non-charge balanced, NCB) and $(Ge_{1-y-z}Zn_yIn_zTe)_{1-x}(Bi_2Te_3)_x$ (charge balanced, CB) were prepared by tube sealing method with pure elements as starting materials. Ge (99.999 wt.%), Bi (99.995 wt.%), Zn (99.99 wt.%), In (99.999 wt.%) and Te (99.999 wt.%) pieces were used without further purification. The elements were weighted according to stoichiometric ratios (total mass 5 grams) and transferred into silica tubes. The tubes were evacuated (10^{-3} Torr) and sealed with an oxygen/natural gas torch. Samples were then transferred into muffle oven and heated to 1000 ℃ in 12h and kept for 12h before quenching in ice water. The obtained ingots were

then grinded for 30min into fine powder in an argon glovebox and then sealed inside a Teflon ball milling jar. Powders were then milled at 200rpm for 30min on a Netzsch PULVERISETTE 6 planetary ball mill machine. The obtained powders were loaded into a graphite die (15 mm in diameter) and sandwiched between two pieces of 0.15 mm thick graphite foils. Pellet samples with thickness of 2~3 mm and high relative density (>95%, see **Table S1**) were obtained via spark plasma sintering. Powders were heated to 500 ℃ in 5min and held for 5 min under a pressure of 40 MPa.

Phase Identification: Powder X-ray diffraction (PXRD) was employed to characterize the samples' purity. PXRD data were collected in the 2θ range from 20 to 80° on a PANalytical X'Pert Pro diffractometer. Linear X'Celerator detector and Cu $K_{\alpha 1}$ (λ = 1.5406 Å) radiation were used during the measurement. Powders were deposited on a zero-background silicon disc to minimize the background scattering. High-temperature powder diffraction data were collected on the same diffractometer using an Anton Paar HTK 2000 chamber and under dynamic vacuum achieved by a turbomolecular pump. For these high-temperature measurements, the powder was deposited on the Pt heating strip.

Thermoelectric Properties Characterization: Seebeck coefficient (S) and electrical conductivity (σ) from 300K to 800K were measured on a ULVAC-RIKO ZEM-3 instrument. During the measurement, samples were kept under helium atmosphere to avoid oxidation. Bar-shaped samples with the dimension of 2 x 2 x 10 mm^3 were used. The surface of each specimen was gently polished using 600 and 1200 grit SiC papers to eliminate surface contamination. The total thermal conductivity, κ, was calculated using the formula $\kappa = DC_p\rho$, where ρ is the sample density, measured using the Archimedes method.

All samples show high relative density of over 95% (**Table S1**). Thermal diffusivity *D* from 300K to 800K was measured using laser flash analysis (LFA) method on a Netzsch LFA-457 instrument. Heat capacity C_p was directly derived using the Dulong-Petit law. The Hall coefficient (R_H) was measured using the Van der Pauw geometry in a reversable magnetic field up to ± 0.5T[62]. Carrier concentration (n_H) and Hall carrier mobility (μ_H) were calculated using $n_H = 1/(eR_H)$ and $\mu_H = \sigma R_H$, respectively. Here, e representing the electron charge.

Microstructure analysis: Secondary and backscattering electron images were captured by a scanning electron microscope (SEM, Tescan Vega II LSU, USA. The samples were prepared by hand polishing using 600 and 1200 grit SiC papers. Elemental distribution was determined via energy dispersive X-ray spectroscopy (EDS). The transmission electron microscopy (TEM) specimen was prepared using a ThermoFisher Scientific Helios G4 UXe dual-beam plasma focused ion beam (PFIB) following in-situ lift-out procedure[63]. Selected area electron diffraction (SAED) and scanning transmission electron microscopy-energy dispersive X-ray spectroscopy (STEM-EDS) were performed on a ThermoFisher Scientific Talos F200X G2 TEM microscope operated at 200kV. High-angle annular dark-field transmission electron microscopy (HAADF-STEM) images were recorded on a double-aberration-corrected FEI (part of ThermoFisher Scientific now) Titan Cubed 80/300 TEM at 200 kV with a semi-convergence angle of ~ 19 mrad and a semi-collection angle in the range from 64 to 200 mrad. The TEM sample has been cleaned with a Gatan low-energy Solarus plasma cleaner for 3 mins before the TEM experiments. Inverse fast Fourier transforms (IFFT) was done via the Gatan Digital Micrograph software.

Theoretical Calculations: Density functional theory calculations were performed via the Quantum Espresso[64–66]. A projector-augmented wave (PAW) method was used to model the electron-ion interaction for the Ge, Bi, Zn, In and Te atoms. The parameterization by Predew, Burke and Ernzerfhof (PBE) based on generalized gradient approximation (GGA)[67–69] was applied to calculate the band structure and the cutoff energy for the wave function was set to 50 Ry. A 3 × 3 × 3 supercell containing 27 Ge and 27 Te sites was constructed, and a 6 × 6 × 6 k mesh was adopted for the Brillouin zone integration. Some of the Ge sites were replaced by Bi, Zn, In, and a vacancy to simulate the doped systems. All the possible configurations were considered and the one with the lowest total energy was chosen as the final supercell structure. Considering that the band morphology of GeTe is highly sensitive to the cell parameters, we directly used the values extracted from our PXRD data. Only the position of the atoms was fully relaxed until the force on each atom is less than 0.001eV/Å. Spin-orbit coupling was included in the calculation.

4.3 Results and Discussion

4.3.1 Phase Identification

A series of Bi/Zn/In co-doped samples were synthesised and their PXRD pattern are presented in **Figure 4.2**. The PXRD patterns for each phase based on their powder diffraction files (PDF) are listed at the bottom of the diagram [70–72]. In this work, Bi was doped in two different ways, in the form of BiTe and Bi_2Te_3 for the NCB and CB systems, respectively. All the samples contained the major phase with the rhombohedral symmetry (*R*3*m*, #160) with trivial Ge precipitates (marked by red asterisks). A ZnTe secondary phase could also be detected in Zn-doped samples as seen in the close-up image in **Figure 4.2 (b)**,

where ZnTe peaks are marked by purple triangles. The formation of ZnTe impurity phase indicates that the solubility of Zn is less than 4 mol.%, which is lower than the previously reported 6 mol.% [52,73]. Cell parameters were extracted through the Rietveld refinement and are listed in **Table S4.2**. Doping with Bi reduces the *c*/*a* ratio, and such phenomenon is more profound in the CB system. Further doping with Zn and In only slightly affects the cell parameters; this can be attributed to the similar atomic size of Zn (0.88 Å) and Ge (0.87 Å) and the low doping levels of Zn and In. SEM analysis was performed on $(Ge_{0.97}Zn_{0.02}In_{0.01}Te)_{0.97}(Bi_2Te_3)_{0.03}$, and the results are presented in **Figure S4.2**. According to our elemental mapping, all elements are distributed uniformly inside the sample, indicating the successful doping of Bi, Zn and In.

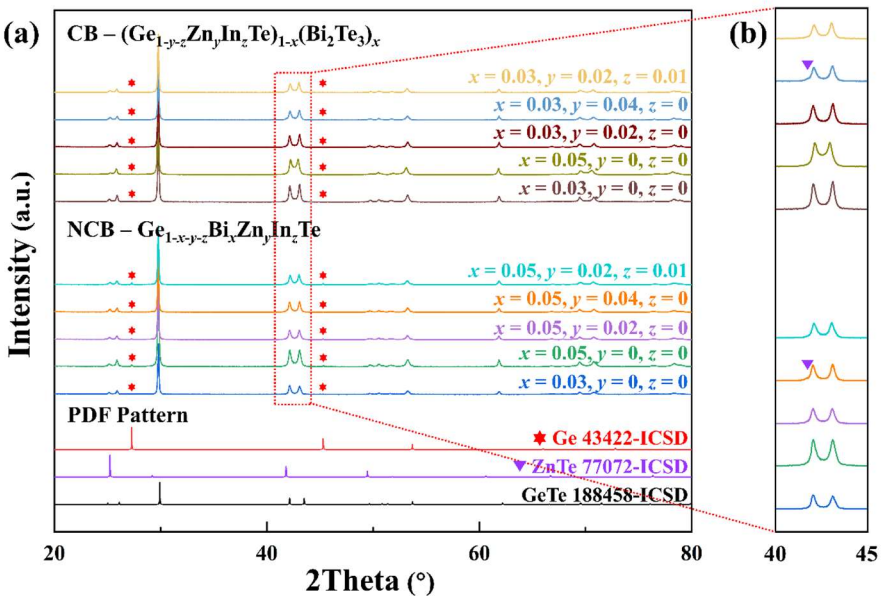

Figure 4.2. (a) PXRD patterns of the Bi/Zn/In co-doped samples synthesised for this work. (b) A close-up between $2\theta = 40°$ and $2\theta = 45°$, showing a peak of the ZnTe impurity.

4.3.2 Electrical Properties

Figure 4.3 shows the measured electric properties. The positive sign of Seebeck coefficient, *S*, indicates a *p*-type conduction nature for all the samples. In both systems, Bi doping improves the Seebeck coefficient significantly; a room-temperature Seebeck coefficient as high as 182 μV/K is achieved in $Ge_{0.95}Bi_{0.05}Te$. Such improvement was caused by two reasons. Firstly, the donor nature of Bi effectively reduced the carrier concentration from 6.10×10^{20} cm^{-3} in pristine GeTe to 1.75×10^{20} cm^{-3} in $Ge_{0.95}Bi_{0.05}Te$ and 3.51×10^{20} cm^{-3} in $(GeTe)_{0.97}(Bi_2Te_3)_{0.03}$. In the NCB system, such reduction is caused by the counter doping; where Bi substitutes for Ge and provide one free electron which neutralizes the intrinsic hole carriers:

$$\mathrm{Bi} + \mathrm{Ge}_{\mathrm{Ge}}^{\times} \rightarrow \mathrm{Ge} + \mathrm{Bi}_{\mathrm{Ge}}' \tag{4.3}$$

However, in the CB system, doping by Bi_2Te_3, yields:

$$2\mathrm{Bi} + 3\mathrm{Ge}_{\mathrm{Ge}}^{\times} \rightarrow 2\mathrm{Bi}_{\mathrm{Ge}}' + \mathrm{V}_{\mathrm{Ge}}^{\cdot\cdot} + 3\mathrm{Ge} \tag{4.4}$$

Here, $\mathrm{Ge}_{\mathrm{Ge}}^{\times}$ is a Ge atom on the Ge site with no extra charges, $\mathrm{Bi}_{\mathrm{Ge}}'$ is a Bi atom on the Ge site with a charge of -1 and $\mathrm{V}_{\mathrm{Ge}}^{\cdot\cdot}$ represents a Ge vacancy with a charge of +2. As can be seen, Bi_2Te_3 doping should not directly affect the carrier concentration. It has been widely reported that Bi_2Te_3 and Sb_2Te_3 doping can effectively increase the formation energy of the cation vacancy defect in both the GeTe and SnTe systems [74–76]. Therefore, the reduction of the carrier concentration in the CB system originates from the suppression of Ge vacancies. Our DFT calculation shows that doping with Bi_2Te_3 increases the Ge vacancy formation energy from 0.62 eV to 0.96 eV (**Figure S4.6**), which agrees well with previous reports. Besides lowering the carrier concentration, Bi doping also reduces the

c/a ratio (enlarges the interaxial angle), which decreases the energy separation between the Σ and L bands ($\Delta E_{L\text{-}\Sigma}$)[42,52]. This can be proved by the increased DOS effective mass upon Bi doping, as shown in **Table S4.3**. Here, the DOS effective mass is calculated based on the developed single Kane band (SKB) model, whose details could be found in **Section 4.5 Supporting Information**.

The subsequent Zn doping impact the Seebeck coefficient and electrical conductivity differently in the two systems. For the NCB system, Zn doping slightly reduces the Seebeck coefficient while improving the electrical conductivity. As a result, the overall power factor is improved throughout the whole working temperature range. However, no obvious trend could be found upon Zn doping in CB system. In both cases, doping Zn effectively reduces the carrier concentration and improves the carrier mobility, which could be explained by the reduced Ge vacancy concentration. Our DFT calculation shows that introducing Zn increases the formation energy of Ge vacancy from 0.62 eV to 0.69 eV, indicating that Zn doping can suppress the formation of Ge vacancy defects, as shown in **Figure S4.7**. In comparison with Bi_2Te_3 doping, which also increases the formation energy of Ge vacancies, Zn atom has the same valency and similar atomic size with respect to the host Ge atoms, which minimizes the scattering caused by itself, making it possible to improve the mobility.

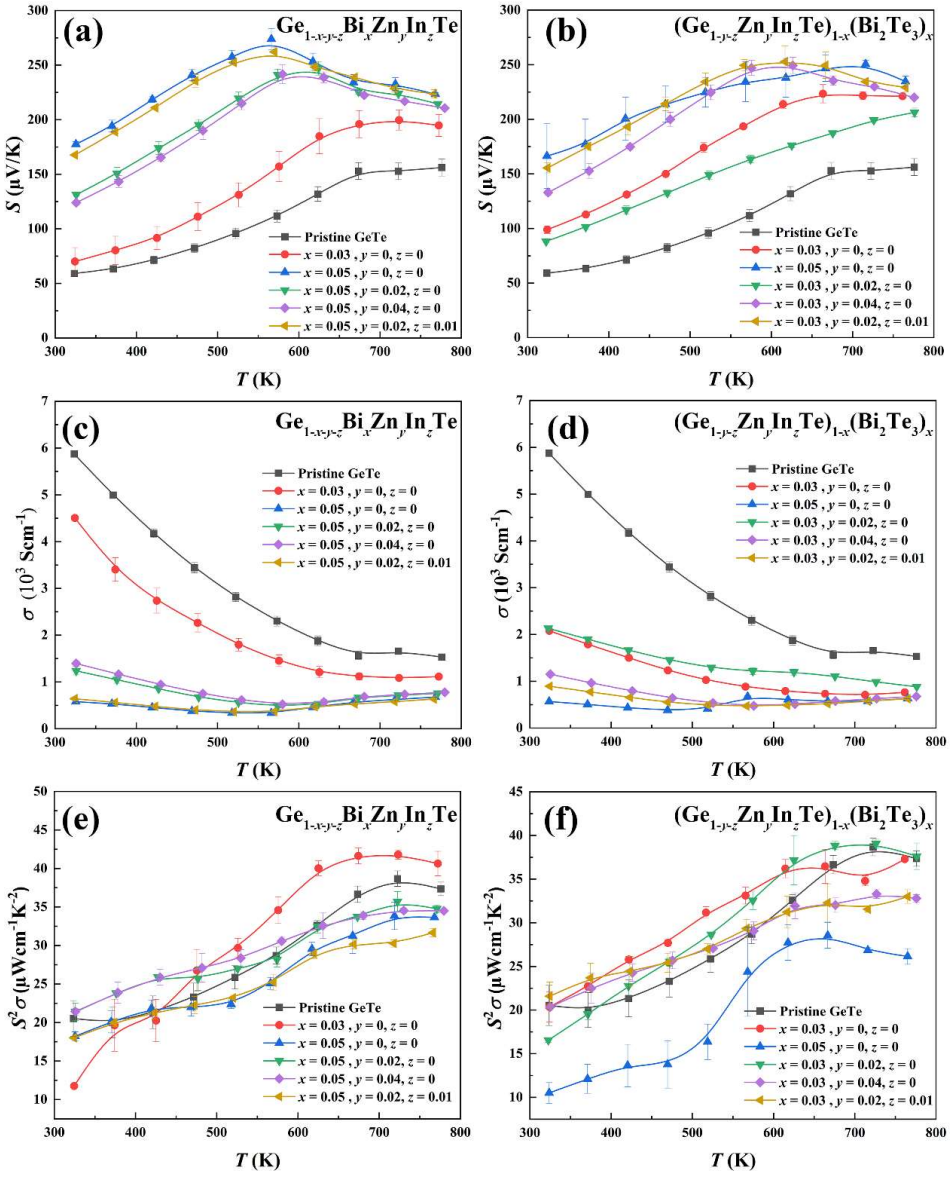

Figure 4.3. (a), (b) Seebeck coefficient, (c), (d) electrical conductivity and (e), (f) power factor. Here (a), (c), (e) belongs to NCB system while (b), (d), (f) belongs to CB system.

Finally, 1 mol. % of In was introduced into both systems to induce DOS distortion in the vicinity of the Fermi level (**Figure S4.5** (d)); such strategy has been shown to be an effective way to improve the average zT value of the GeTe-based systems [77]. The induced

DOS distortion effectively increases the DOS effective mass for both systems (**Table S4.3**) which improves the Seebeck coefficient in the whole temperature range.

4.3.3 DFT Study

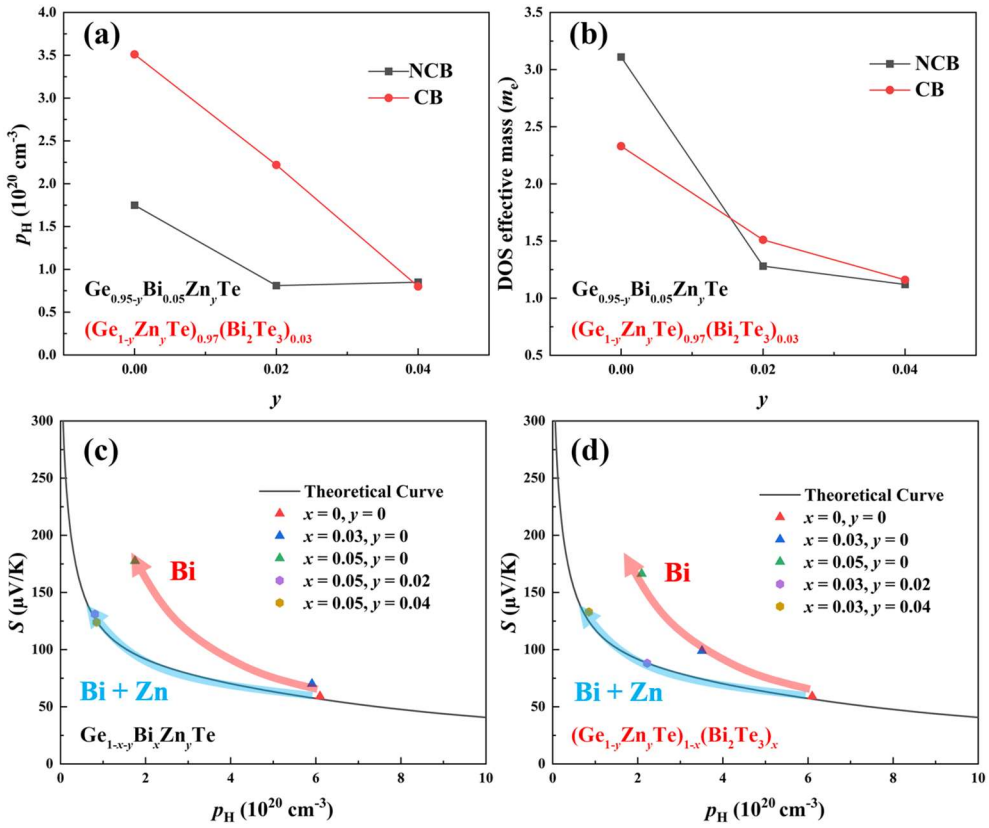

Figure 4.4 (a) Hall carrier concentration for the NCB and CB samples, (b) calculated DOS effective mass for the NCB and CB samples, (c) Room temperature Pisarenko plot for the NCB samples and (d) Pisarenko plot for the CB samples.

Room-temperature Pisarenko plots were calculated based on the semi-classical Boltzmann transport theory using Quantum Espresso and BoltzTraP code[78] (**Figure 4.4**). Non-self consistency calculations were performed on a primitive unit cell of GeTe. During the calculation, a dense *k* mesh of 30 × 30 × 30 was used to sample the first Brillouin zone.

The Hall data points were adapted into the calculated Pisarenko plots (**Figure 4.4** (c) and (d)). As can be seen, in both systems, Bi doping gradually shifts the data points above the theoretical curve, which is due to the reduced $\Delta E_{L\text{-}\Sigma}$. Further Zn doping shifts the data points to the left and places them onto the theoretical curve, indicating that Zn doping enlarges $\Delta E_{L\text{-}\Sigma}$. To verify this assumption, the band structure of the doped systems was calculated, and the results are presented in **Figure 4.5**.

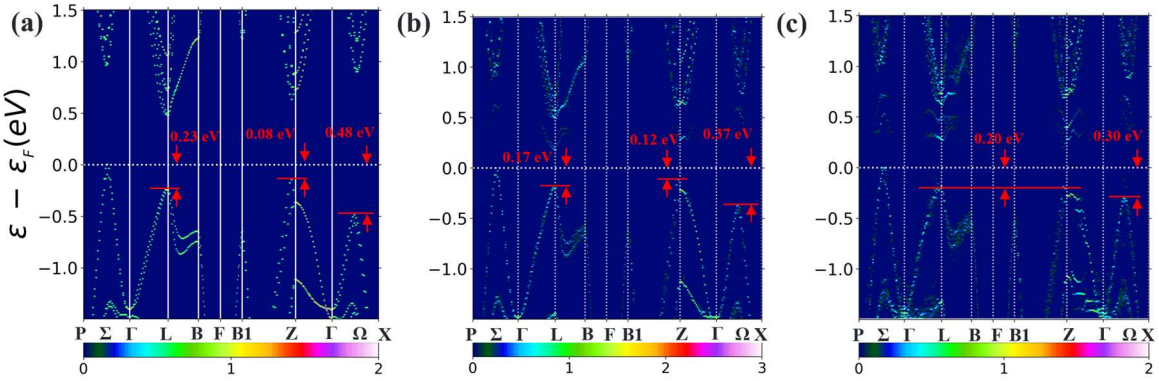

Figure 4.5. Calculated band structure of (a) $Ge_{27}Te_{27}$ (b) $Ge_{26}BiTe_{27}$ and (c) $Ge_{25}BiZnTe_{27}$. The color bars under the band structure represent to the number of primitive cell bands which overlap at a given primitive wave vector. The Fermi level is set to the top of the valence band.

Band unfolding is performed via the BandUP code [79,80]. The Fermi level is set to the top of the valence band. As can be seen, $\Delta E_{L\text{-}\Sigma}$ of is firstly reduced from 0.23 eV in pristine GeTe to 0.17 eV in Bi doped supercell. After introducing Zn element, $\Delta E_{L\text{-}\Sigma}$ was enlarged to 0.20 eV. This result indicates that, when co-doping with Bi, Zn tend to enlarge $\Delta E_{L\text{-}\Sigma}$, which agrees well with our theory. In the meantime, as shown in **Figure S4.5**, introducing In results in a strong DOS distortion near Fermi level. This distortion is caused

by the strong *s-p* hybridization between the Ge $4p^2$, Te $5p^4$, and In $5s^2$ orbitals. Since the size of the supercell was kept small, the simulated In doping level was 3.7 mol.%, which is 3 times higher than the actual doping level of 1 mol. %. While the results for the In-doped systems could be analyzed only qualitatively, the calculated DOS distortion should lead to heavier charge carriers, and that is exactly what is observed experimentally (**Table S3**).

The thermal conductivity was measured via laser flash analysis and the results are displayed in **Figure 4.6**, where the lattice thermal conductivity was calculated by extracting the electrical thermal conductivity from the total thermal conductivity. The electrical thermal conductivity is given by the Wiedemann-Franz law. The Lorenz number *L* was calculated by the SKB model[28]. The total thermal conductivity dropped significantly throughout the whole temperature range upon the Bi doping. As can be seen, the dominant factor in such suppression is the lower electrical thermal conductivity, which can be attributed to the reduced carrier concentration (**Table S4.3**).

4.3.4 Thermal Transport Properties

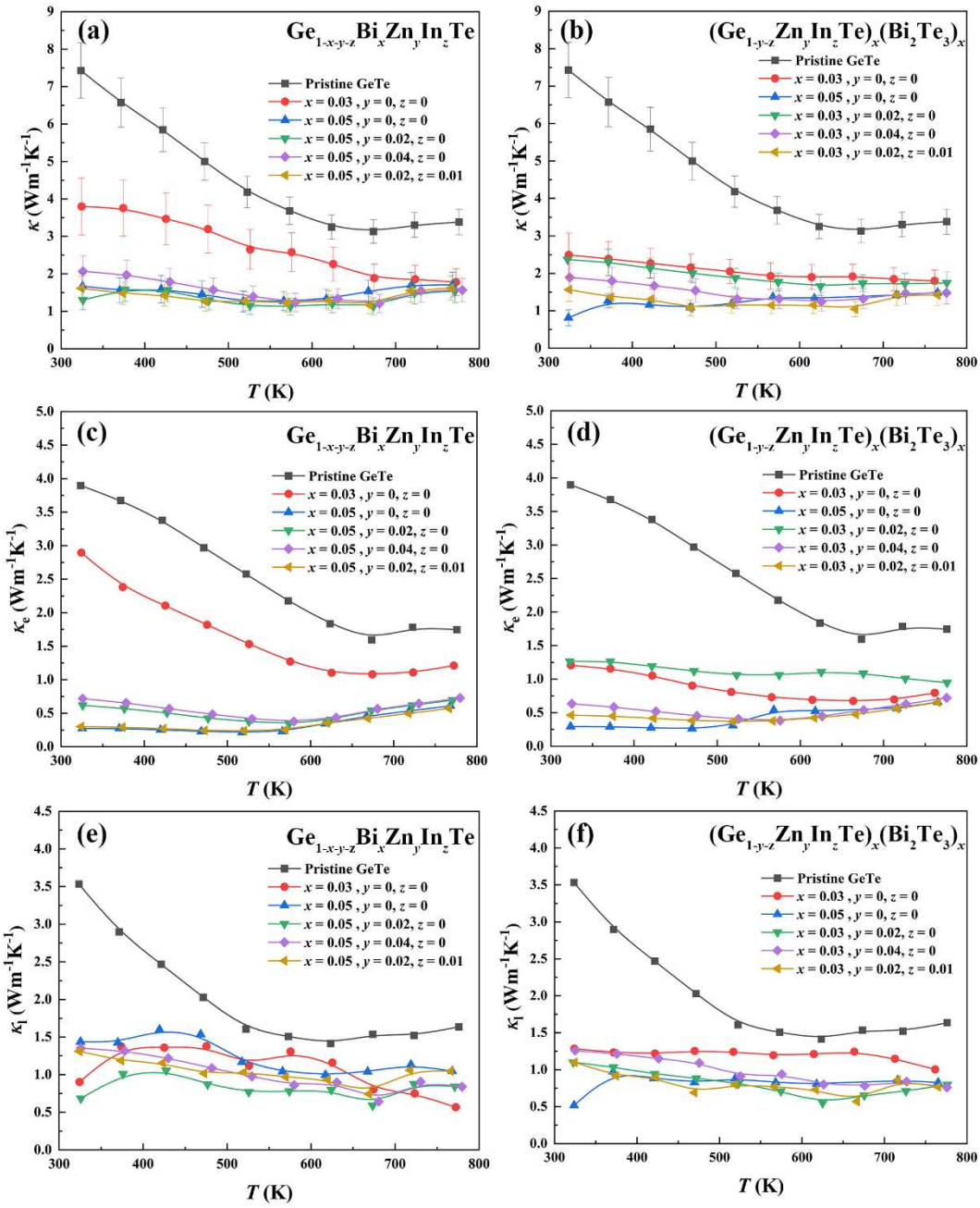

Figure 4.6. (a), (b) Total thermal conductivity, (c), (d) lattice thermal conductivity and (e), (f) electrical thermal conductivity. (a), (c), (e) are for the NCB system; (b), (d), (f) are for the CB system.

The room-temperature electrical thermal conductivity of the NCB and CB systems are reduced from 3.92 $Wm^{-1}K^{-1}$ to 0.31 $Wm^{-1}K^{-1}$ and 1.16 $Wm^{-1}K^{-1}$, respectively. In the NCB system, Zn doping increases the low-temperature electrical thermal conductivity and reduces the lattice thermal conductivity. In the CB system, Zn doping reduces the lattice thermal conductivity systematically, and the reduced carrier concentration effectively suppresses the electrical thermal conductivity for $y = 0.04$. It should be noted that the electrical thermal conductivity is higher for $y = 0.02$ than for $y = 0$ (without Zn doping) in the CB system; this is due to the improved carrier mobility upon Zn doping (51.3 $cm^2/V \cdot s$ vs. 36.5 $cm^2/V \cdot s$). In both systems, In doping reduces the electrical thermal conductivity, which is caused by the relatively poor carrier mobility (**Table S4.3**). Close-up images excluding the pristine GeTe curve can be found in **Figure S4.4** (c) and (d).

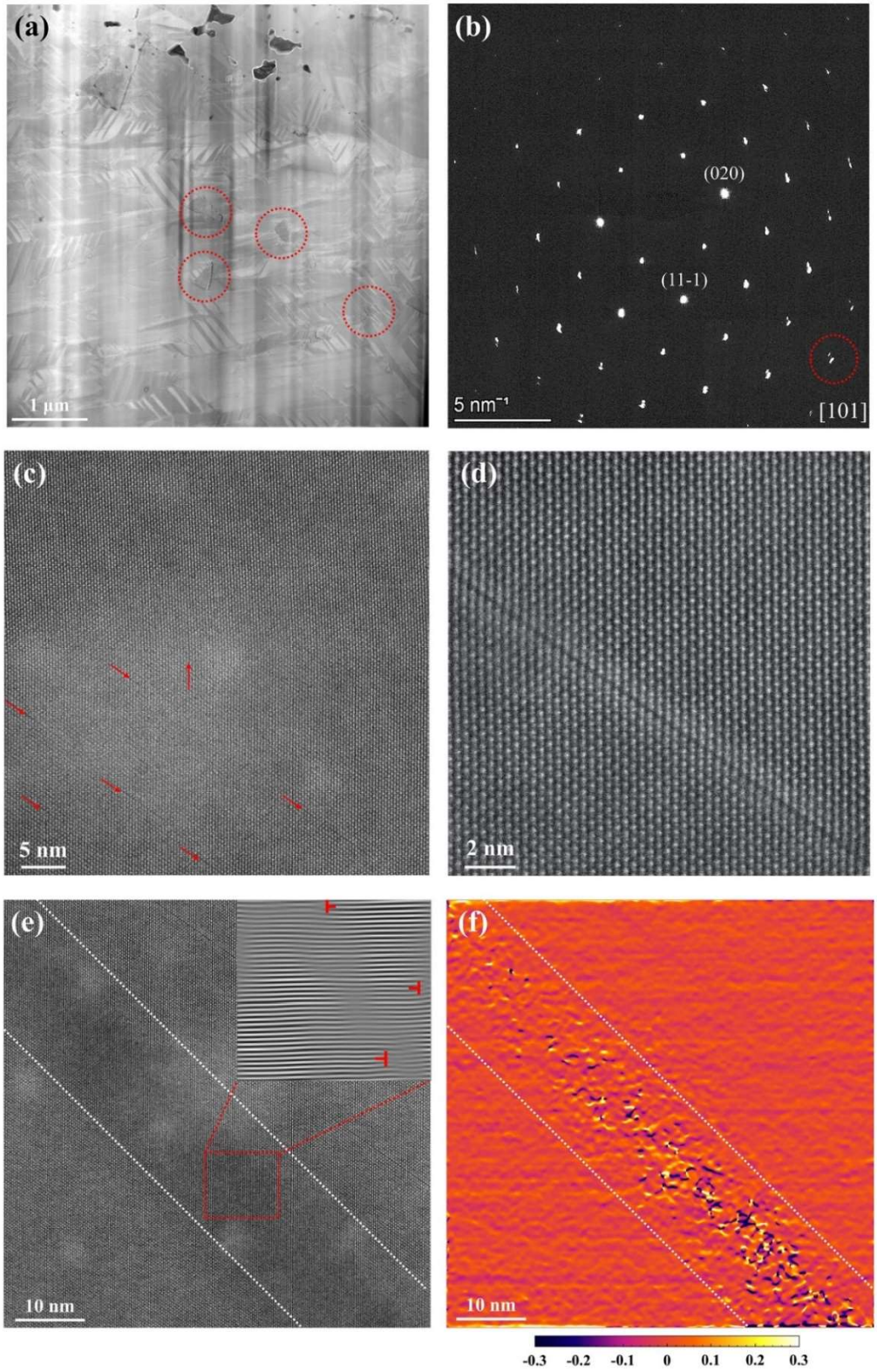
(a)
1 μm
(b)
(020)
(11-1)
5 nm⁻¹
[101]
(c)
5 nm
(d)
2 nm
(e)
10 nm
(f)
10 nm
-0.3 -0.2 -0.1 0 0.1 0.2 0.3

Figure 4.7. STEM and SAED images of $(Ge_{0.97}Zn_{0.02}In_{0.01}Te)_{0.97}(Bi_2Te_3)_{0.03}$. (a) Twin formation inside the matrix. The gray particles marked by red circles are ZnTe nanoprecipitations and the black particles at the top of the image are nano-sized Ge precipitations. (b) Selected area electron diffraction pattern along <101>. (c) STEM-HAADF image; defect layers are marked by red arrows. (d) Close-up image of such defect layer. (e) Dislocation band; the dotted lines are guides for the eye. The inserted image is the IFFT of the selected area, high density of dislocations could be observed. (f) Strain (ε_{yy}) distribution calculated via the geometric phase analysis. The color bar is shown at the bottom of the image.

4.3.5 TEM Analysis

To gain more knowledge of the suppressed lattice thermal conductivity, TEM analysis was performed on $(Ge_{0.97}Zn_{0.02}In_{0.01}Te)_{0.97}(Bi_2Te_3)_{0.03}$. **Figure 4.7**(a) shows the overview of the sample lifted out using the Plasma-FIB. Areas with bright and dark contrast are distributed alternately. This herringbone structure originates from the regular arrangement of twin domains in the rhombohedral GeTe-type phase. Nano-sized particles with gray and black colors are observed. To find out their compositions, EDS analysis was performed, and the results are shown in **Figure S4.7**. As can be seen, the black particles are Ge precipitations while the gray particles are a Zn- and Te- rich phase. Combined with the PXRD pattern (**Figure 4.2**(b)), these particles could be identified as ZnTe precipitations. **Figure 4.7**(b) shows the selected area electron diffraction pattern along <101>, and the diffraction spot splitting indicates the presence of twinning [52,81]. **Figure 4.7** (c) shows the

STEM-HAADF image of the lattice; dark lines (highlighted by red arrows) are seen inside the structure.

A close-up image of such area is shown in **Figure 4.7**(d), and a defect layer is visible. Such phenomenon has been reported in the Bi_2Te_3- and Sb_2Te_3-doped GeTe systems[82–85]. We also observed band-shaped areas with relatively low contrast, and one of them is shown in **Figure 4.7**(e). An IFFT image for the selected area (marked by the red box) is shown in the inserted image in **Figure 4.7**(e). As can be seen, the low contrast is caused by the high-density of dislocation defects that accumulate in this area. Geometric phase analysis [86] was performed via the Strain ++ software and the result is shown in **Figure 4.7**(f). The presence of high-density dislocation creates strong strain fluctuation inside these areas and extra scattering sources of phonons with various wavelengths.

4.3.6 Figure of Merit

Using the above data, *zT* values were calculated and are presented in **Figure 4.8**. With all the uncertainties added up, the error is around 15%. For the NCB system, a peak *zT* value of 2.01 at 673K and an average *zT* value of 1.26 are achieved in $Ge_{0.93}Bi_{0.05}Zn_{0.02}Te$. For the CB system, a peak *zT* value of 2.06 at 667K and an average *zT* value of 1.30 are achieved in $(Ge_{0.97}Zn_{0.02}In_{0.01}Te)_{0.97}(Bi_2Te_3)_{0.03}$, which is slightly higher than that for the NCB sample. As shown in **Figure 4.7**(b), the Bi/Zn/In co-doping improves the average *zT* value by more than 30% in comparison with the solely Bi-doped samples. The TE performance of this work is among the best lead-free system reported so far. The high average *zT* is attributed to the promising low temperature (300K ~ 550K) TE

performance, which is above that of the many state-of-the-art lead-free GeTe systems, as shown in **Figure 4.8**(d).

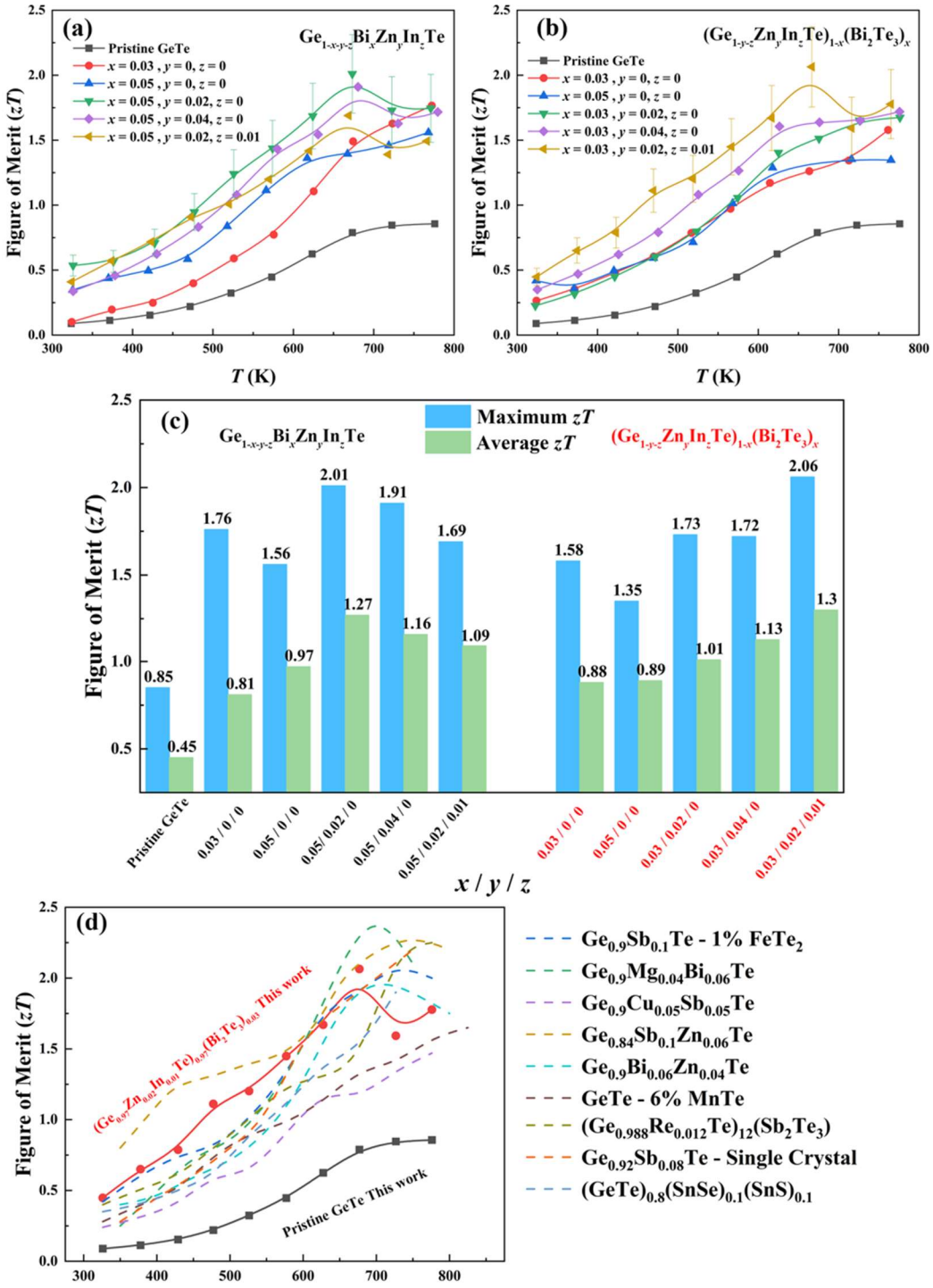

Figure 4.8. (a) and (b) *zT* values of the NCB and CB systems, respectively. (c) Average and peak *zT* values for the different materials in this work. (d) Comparison of our *zT* vs. *T* curves with those for the state-of-the-art lead-free GeTe materials[87–89,73,52,45,90–92]

4.4 Summary

In this work, the thermoelectric behavior of the Bi/Zn/In co-doped GeTe was investigated. During the experiments, Bi was doped in two ways, as BiTe (NCB system) and Bi_2Te_3 (CB system). In both cases, Bi doping positively affects the thermoelectric performance. The subsequent Zn doping reduced the carrier concentration and optimized the mobility, and this effect was not observed in the previous Zn-doped GeTe-based systems. This could be attributed to the suppression of Ge vacancy formation by Zn doping. Further In doping on the Ge site leads to a strong DOS distortion in the vicinity of the Fermi level and also affects the thermal conductivity. In the NCB systems, the resulting high performance is attributed to the improved power factor in the whole temperature range. In the CB systems, the improvements originate from the effectively suppressed thermal conductivity.

Nano twinning, defect layers, “dislocation bands”, and nanosized ZnTe and Ge precipitations (80 ~ 500nm) were observed in the STEM images of $(Ge_{0.97}Zn_{0.02}In_{0.01}Te)_{0.97}(Bi_2Te_3)_{0.03}$. These microstructures induce strong strain fluctuations and high lattice anharmonicity which facilitate the suppression of lattice thermal conductivity. Eventually, a peak *zT* of 2.06 and a promising average *zT* of 1.30 have been achieved in $(Ge_{0.97}Zn_{0.02}In_{0.01}Te)_{0.97}(Bi_2Te_3)_{0.03}$. This work provides new insights into the

thermoelectric behavior of the co-dopants in the GeTe-based system and paves the path for improving the performance of the lead-free GeTe-based thermoelectric materials.

4.5 Supporting Information

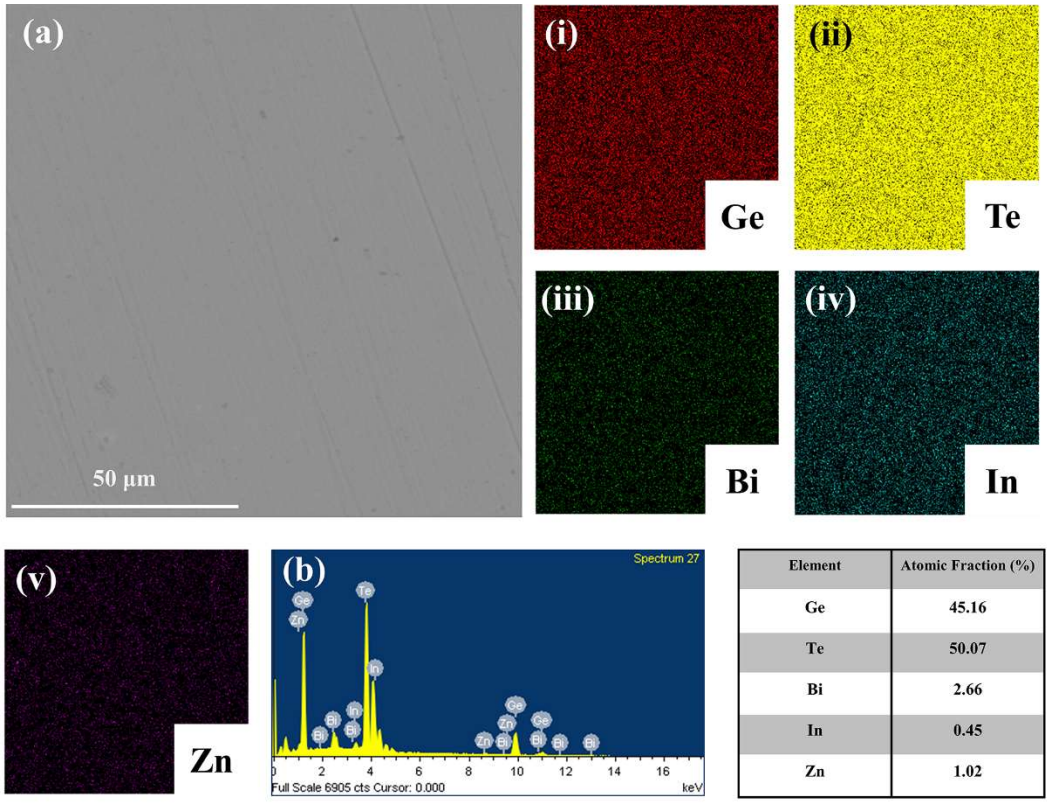

Element	Atomic Fraction (%)
Ge	45.16
Te	50.07
Bi	2.66
In	0.45
Zn	1.02

Figure S4.1. SEM images of $(Ge_{0.97}Zn_{0.02}In_{0.01}Te)_{0.97}(Bi_2Te_3)_{0.03}$. (a) Back scattered electron (BSE) image, (b) energy dispersive spectroscopy (EDS) spectrum and the corresponding elemental concentrations, (i) ~ (v) elemental mappings.

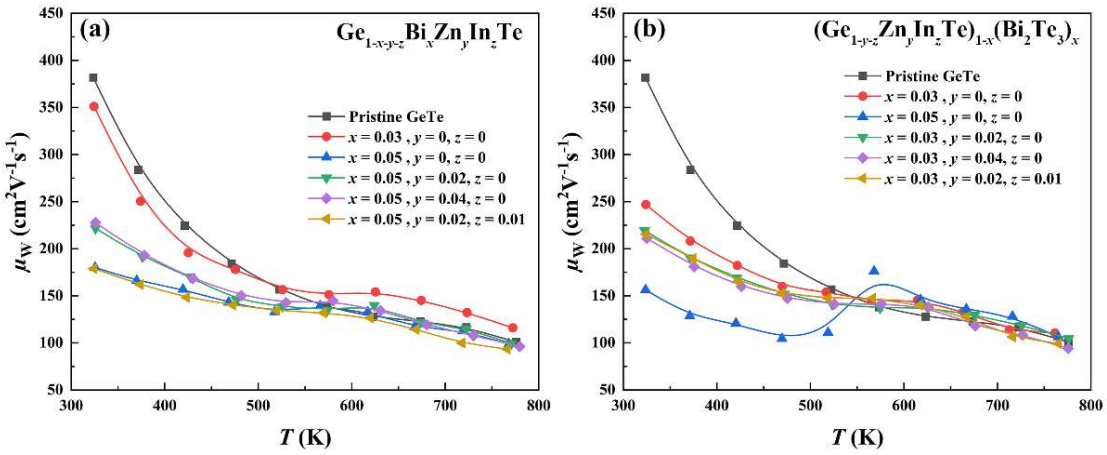

Figure S4.2. Weighted mobility for the (a) NCB and (b) CB samples, respectively.

Here the weighted mobility is given by[93]

$$\mu_{\mathrm{W}} = \frac{3h^3\sigma}{8\pi e(2m_{\mathrm{e}}k_{\mathrm{B}}T)^{3/2}}\left[\frac{\exp\left[\frac{|S|e}{k_{\mathrm{B}}}-2\right]}{1+\exp\left[-5\frac{|S|e}{k_{\mathrm{B}}}-1\right]}+\frac{\frac{3}{\pi^2}\frac{|S|e}{k_{\mathrm{B}}}}{1+\exp\left[5\frac{|S|e}{k_{\mathrm{B}}}-1\right]}\right] \quad \text{(S4.1)}$$

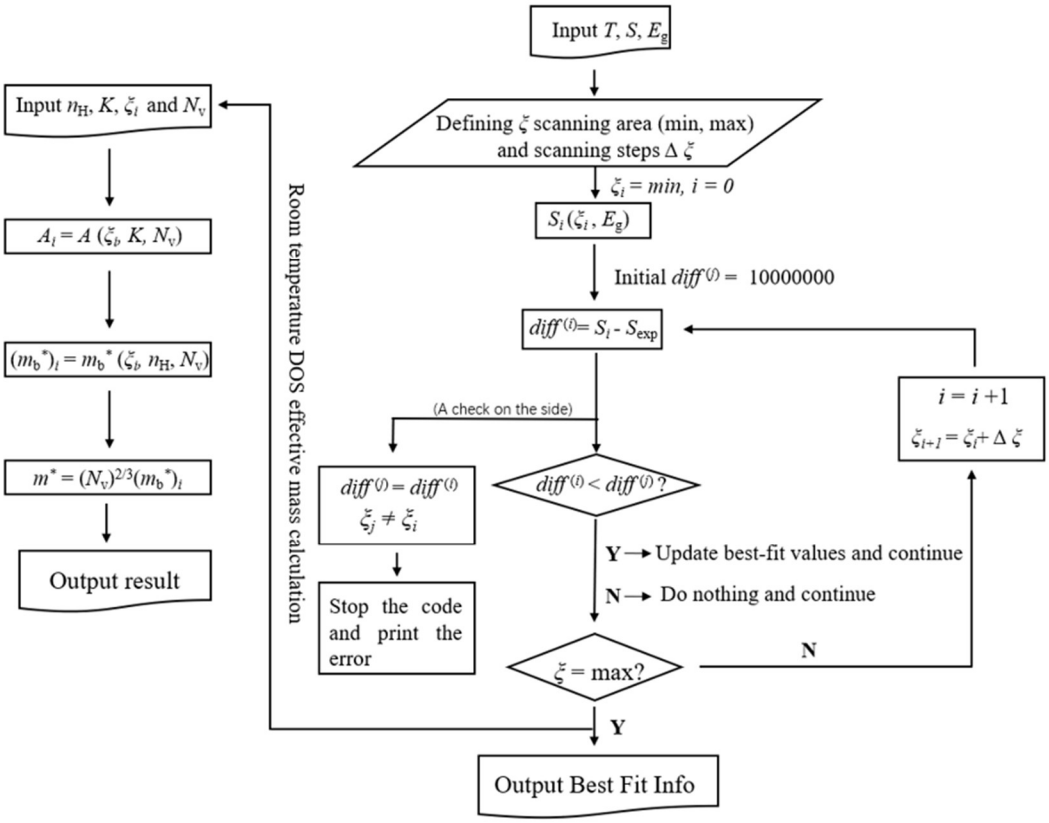

Figure S4.3. (a) Basic logic of the SKB solving code. (b) Carrier concentration obtained by the Hall effect measurements. (c) DOS effective mass calculated by the SKB model. The exact value of both (b) and (c) could be found in **Table S4.4**. Here, *y* is the doping level of Zn.

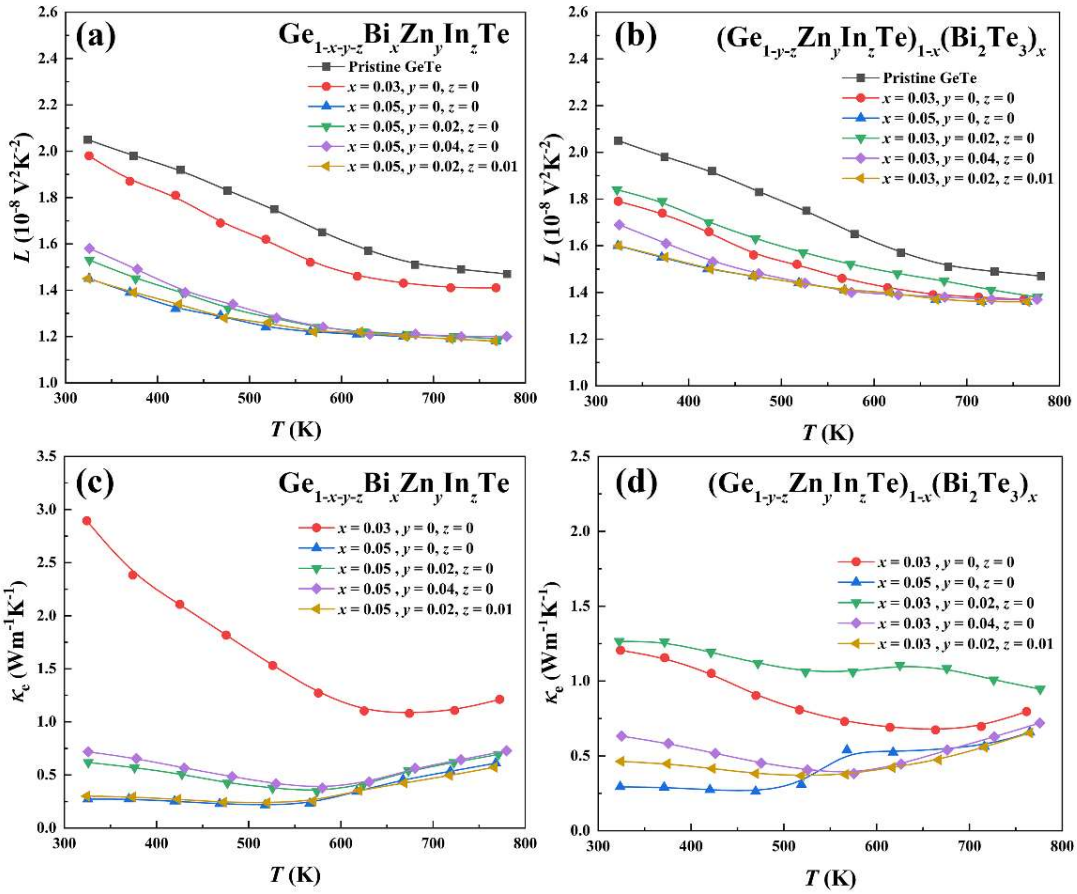

Figure S4.4. (a), (b) Lorenz number, (c), (d) zoom-in image of the carrier thermal conductivity. (a) and (c) belongs to the NCB system, (b) and (d) belongs to the CB system.

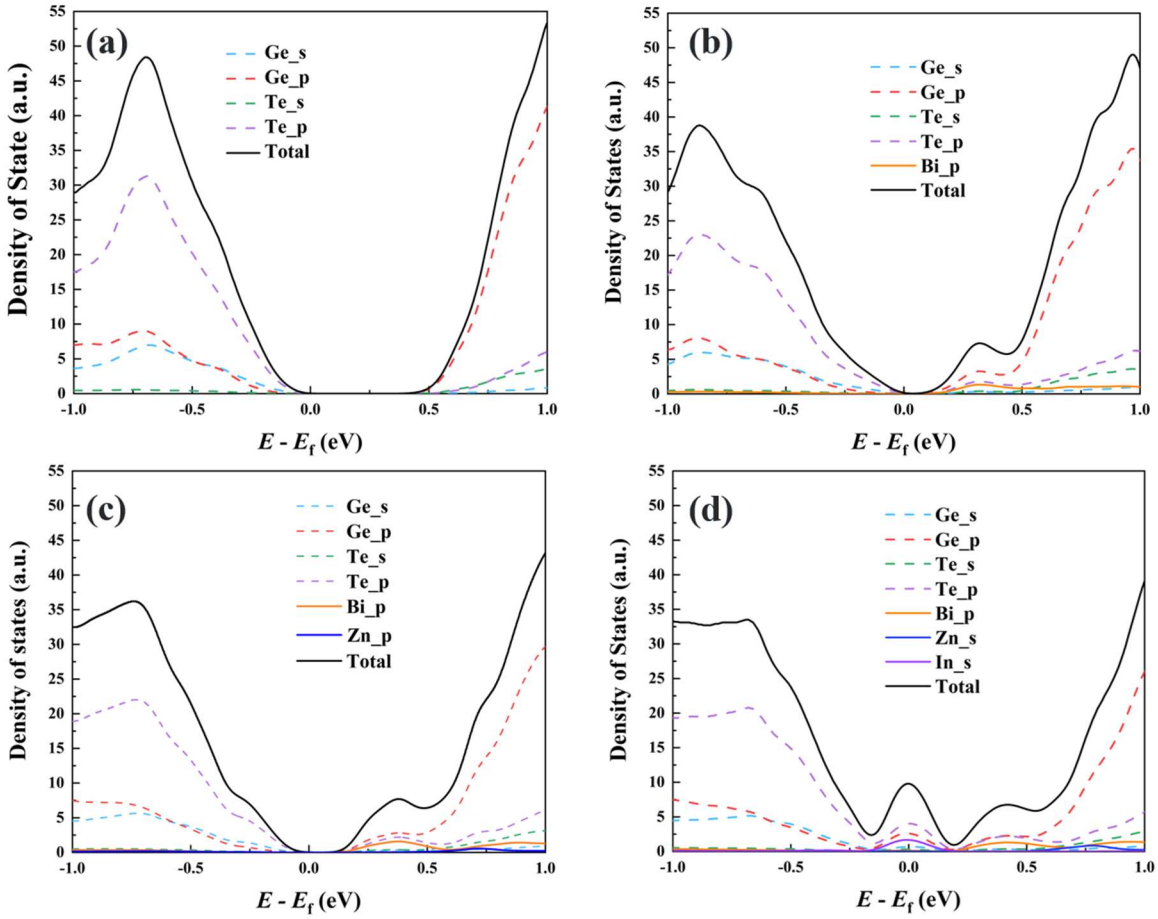

Figure S4.5. Partial density of states of (a)$Ge_{27}BiTe_{27}$, (b) $Ge_{26}BiTe_{27}$, (c) $Ge_{25}BiZnTe_{27}$, (d) $Ge_{24}BiZnInTe_{27}$. The Fermi levels are set to the top of the valence band.

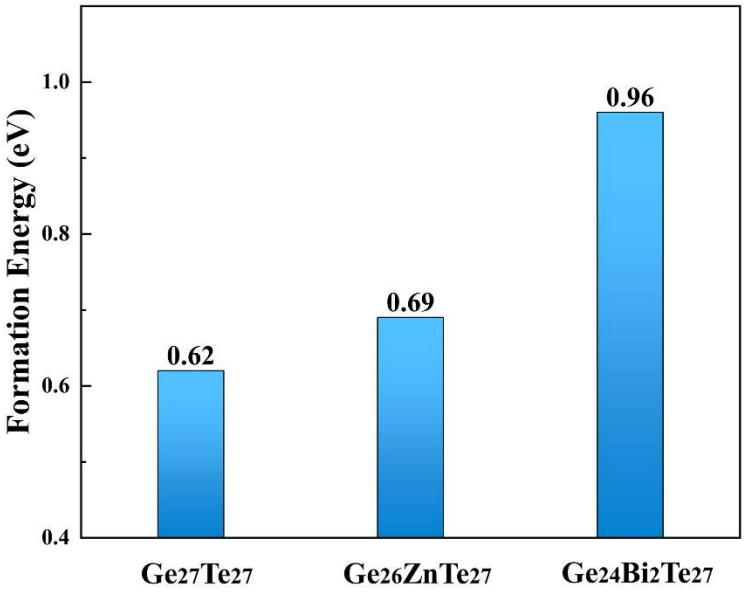

Figure S4.6. Formation energy of a Ge vacancy defect, calculated for $Ge_{27}Te_{27}$, $Ge_{26}ZnTe_{27}$ and $Ge_{24}Bi_2Te_{27}$.

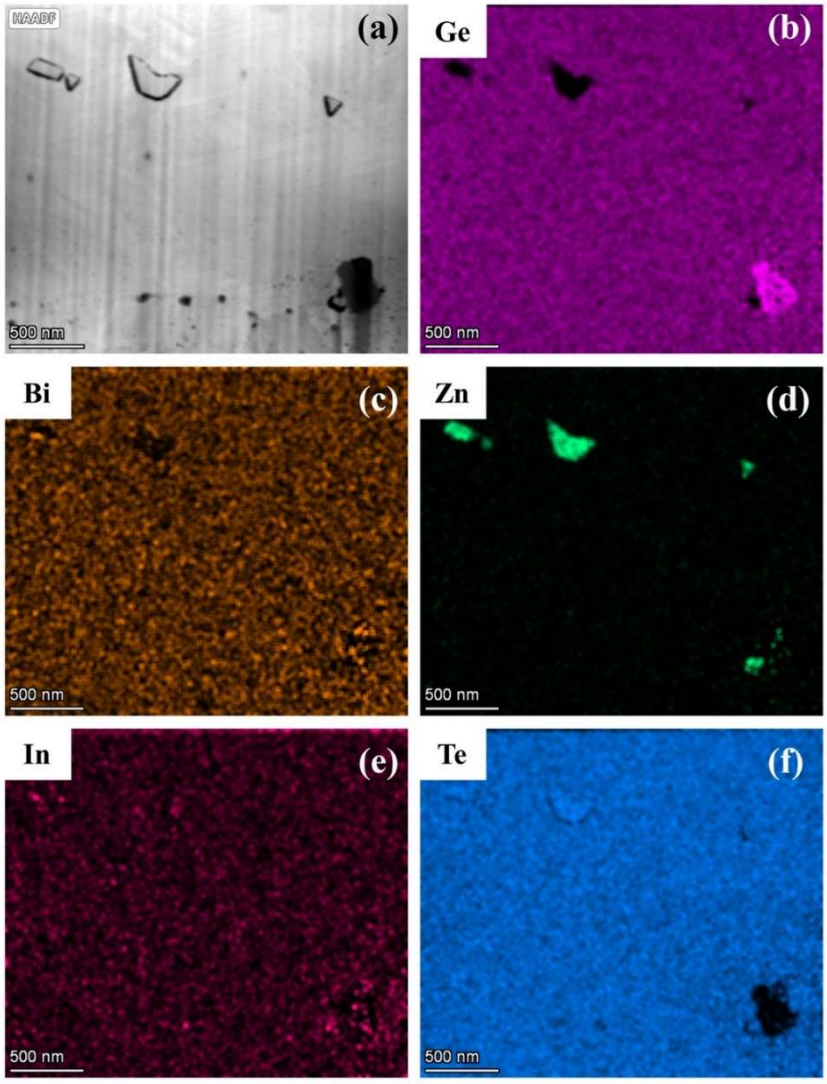

Figure S4.7. (a) STEM image of $(Ge_{0.97}Zn_{0.02}In_{0.01}Te)_{0.97}(Bi_2Te_3)_{0.03}$. This image belongs to another Plasma-FIB lifted sample from the same sample. (b) ~ (f) EDS mapping of Ge, Bi, Zn, In, and Te, respectively. The gray particles are ZnTe precipitations and the black particle at the lower right corner is a Ge precipitation.

Table S4.1. Experimental densities, theoretical densities, and the corresponding relative densities.

x/*y*/*z*	Experimental Density (g/cm^3)	Theoretical Density (g/cm^3)	Relative Density (%)
Pristine GeTe	6.03	6.14	98.17
$Ge_{1-x}Bi_xZn_yIn_zTe$ -- NCB			
0.03/0/0	6.11	6.26	97.60
0.05/0/0	6.10	6.35	96.06
0.05/0.02/0	6.11	6.34	96.37
0.05/0.04/0	6.06	6.34	95.58
0.05/0.02/0.01	6.06	6.35	95.43
$(Ge_{1-y-z}Zn_yIn_zTe)_{1-x}(Bi_2Te_3)_x$ -- CB			
0.03/0/0	6.06	6.31	96.04
0.05/0/0	6.34	6.42	98.75
0.03/0.02/0	6.28	6.31	99.52
0.03/0.04/0	6.10	6.30	96.82
0.03/0.02/0.01	6.06	6.32	95.89

Table S4.2. Cell parameters extracted from the Rietveld refinement.

x/*y*/*z*	*a* (Å)	*c* (Å)	*c* / *a*	*Ω* (Å^3)
Pristine GeTe	4.1660(6)	10.669(2)	2.56	160.36(5)
$Ge_{1-x}Bi_xZn_yIn_zTe$ -- NCB				
0.03/0/0	4.18114(9)	10.643(3)	2.54	161.14(6)
0.05/0/0	4.18999(5)	10.625(1)	2.53	161.54(1)
0.05/0.02/0	4.19689(5)	10.600(1)	2.53	161.70(1)
0.05/0.04/0	4.19640(7)	10.605(1)	2.53	161.73(2)
0.05/0.02/0.01	4.19969(5)	10.582(1)	2.52	161.64(1)
$(Ge_{1-y-z}Zn_yIn_zTe)_{1-x}(Bi_2Te_3)_x$ -- CB				
0.03/0/0	4.19240(2)	10.6152(7)	2.53	161.58(6)
0.05/0/0	4.21100(2)	10.5531(5)	2.51	162.06(8)
0.03/0.02/0	4.19223(3)	10.6004(8)	2.53	161.34(1)
0.03/0.04/0	4.20088(2)	10.5965(5)	2.52	161.95(1)
0.03/0.02/0.01	4.20200(2)	10.5799(5)	2.52	161.780 (8)

Table S4.3. Hall measurement data.

$x/y/z$	μ_H ($cm^2/V \cdot s$)	p_H (10^{20} cm^{-3})	m^* (m_e)
Pristine GeTe	57.6	6.10	1.73
$Ge_{1-x}Bi_xZn_yIn_zTe$ -- NCB			
0.03/0/0	46.6	5.91	2.05
0.05/0/0	34.6	1.75	3.11
0.05/0.02/0	73.0	0.81	1.28
0.05/0.04/0	60.6	0.85	1.12
0.05/0.02/0.01	24.9	2.16	3.59
$(Ge_{1-y-z}Zn_yIn_zTe)_{1-x}(Bi_2Te_3)_x$ -- CB			
0.03/0/0	36.5	3.51	2.33
0.05/0/0	20.5	2.09	3.09
0.03/0.02/0	51.3	2.22	1.51
0.03/0.04/0	61.1	0.80	1.16
0.03/0.02/0.01	23.7	2.28	3.27

* The density of state effective mass is calculated by the developed single Kane band model and is in the unit of free electron mass m_e.

Chapter 5. Band and Vacancy Engineering in SnTe to Improve its Thermoelectric Performance

5.1 Introduction

SnTe is a promising analog of PbTe, is environmentally friendly and with low cost. Although SnTe crystalizes in the highly symmetric rock-salt structure, the large energy separation ($\Delta E_{L\text{-}\Sigma}$) between the light hole L and heavy hole Σ bands (0.31eV) makes the contribution of the underlying Σ band almost neglectable[94]. In the meantime, the narrow band gap at the L point (0.18eV) induces strong interaction between the valence band maxima (VBM) and the conduction band minima (CBM) making the top of the L band extremely sharp[30]. Consequently, the density of states (DOS) effective mass of L band is merely ~ 0.3 m_e, resulting in poor a Seebeck coefficient. To overcome this problem, strategies such as band convergence and band inversion were performed[95–98]. Unfortunately, the overall improvement is very limited. Most recently, it was found that Sb_2Te_3 alloying can increase the density of states (DOS) effective mass of SnTe which effectively improves the performance of SnTe[76]. However, limited works were done to explain the mechanism behind such improvement. In the meantime, like all the other vacancy layered systems, SnTe-Sb_2Te_3 shows poor carrier mobility due to the severe electron-vacancy scattering[99,100], which limits any further improvements.

In this work, we first thoroughly investigated the TE properties of $Sn_{0.98}Ge_{0.05}Te$-Sb_2Te_3 system. Here, excess amount of Ge was doped onto cation site, which has been reported as an effective way in reducing the carrier concentration. Sb_2Te_3 alloying shift the direct band gap at the L point into an indirect band gap between the L and Σ points, which

effectively reduced the interaction between the VBM and CBM. Consequently, the L band was flattened, which effectively improved the Seebeck coefficient. Subsequently, to overcome the poor carrier mobility, Pb compensation was performed to control the cation vacancy concentration, improved the carrier mobility from 33.40 $cm^2V^{-1}s^{-1}$ to 56.38 $cm^2V^{-1}s^{-1}$. Meanwhile, Pb compensation broke the charge balance, allowing Sb to precipitate out of the structure. These second-phase particles provided additional source of phonon scattering, effectively suppressing the lattice thermal conductivity. As a result, a peak *zT* of 1.1 at 778K and an average *zT* of 0.56 from 300K to 778K was achieved in $(Sn_{0.98}Ge_{0.05}Te)_{0.91}$ $(Sb_2Pb_{0.5}Te)_{0.09}$, which is one of the best SnTe-based thermoelectric systems.

5.2 Experimental Methods

Sample preparation: $(Sn_{0.98}Ge_{0.05}Te)_{1-x}(Sb_2Pb_yTe_3)_x$ samples were synthesized with the conventional tube sealing method. Sn (ingot, 99.999 wt.%), Ge (pieces, 99.999 wt.%), Sb (pieces, 99.999 wt.%) Te (lump, 99.999 wt.%) and Pb (droplet, 99.999 wt.%) were used during the synthesis. Sn was purified before use based on Zhou et al.'s work[101]. The elements were weighted according to the stoichiometric ratios and sealed inside silica tubes (10^{-3} Torr). Samples were heated to 1000 ℃ in 12h and kept for 6h before being quenched in ice water. Samples were then annealed for 3 days under 650 ℃. The obtained ingots were hand grounded into fine powder inside an argon glovebox and sealed inside a Teflon ball milling jar. Powders was ball milled at 200rpm for 30min with a Fritsch PULVERISETTE 6 planetary ball mill machine. The obtained powders were then loaded into a graphite die (12.7 mm in diameter) and sandwiched between two pieces of 0.15 mm

thick graphite foils. Pellet samples with a thickness of 2~3 mm were prepared by spark plasma sintering (SPS). During the SPS, powders were heated to 450 ℃ in 5 min and held for 5 min under a pressure of 45 MPa.

Crystallographic Study: Powder X-ray diffraction (PXRD) was employed to characterize the samples' purity. Powder XRD data were collected in the range of 2θ= 20-120° on a PANalytical X'Pert Pro diffractometer equipped with a linear X'Celerator detector and using Cu $K_{\alpha 1}$ (λ = 1.5406 Å) radiation at room temperature. During the analysis, powders were deposited on a zero-background silicon disc to minimize the background scattering.

Crystals of the reported phases were manually picked for single crystal X-ray diffraction study. The room temperature experimental data were collected on STOE IPDS II diffractometer (MoKα radiation) equipped with an image plate detector. The absorption correction was performed by optimization of the crystal shape against equivalent reflection[102]. The structure solution was performed with the SHELXT software[103]. The full-matrix least square refinement of the structure was done with SHELXL[104]. The OLEX2 interface[105] was used to run structure solution and refinement programs. The crystallographic data and some experimental details are summarized in Table 1. According to the single crystal XRD data, in all reported phases the occupancy of the sole Sn crystallographic site is below unity. Thus, the Sn site occupancies for all 7 samples were refined freely and the resulting compositions are shown in **Table S5.3**.

Thermoelectric properties characterization: Seebeck coefficient and electrical resistivity were measured from 300K to 800K on an ULVAC-RIKO ZEM-3 instrument. The

measurements were performed under a helium atmosphere to avoid oxidation. During the measurement, bar samples with the dimension of 2 x 2 x 10 mm^3 were used. The total thermal conductivity, κ was calculated using the formula $\kappa = DC_p\rho$, where ρ is the sample density, measured by the Archimedes method. All samples show a high relative density of over 95%. Thermal diffusivity D was measured from 300K to 800K using the laser flash diffusivity method on a Netzsch LFA-457 instrument. Squares with 10×10×1.5 mm^3 were used for these measurements. Heat capacity C_p was derived using the law of Dulong-Petit. The Hall coefficient (R_H) was measured according to Van der Pauw method. The reversable magnetic field was set to ± 0.5T. Hall carrier concentration (n_H) and Hall carrier mobility (μ_H) were calculated using $n_H = 1/(eR_H)$ and $\mu_H = \sigma R_H$, respectively. Here, e representing the electron charge. Using the obtained n_H, the Lorenz number and DOS effective mass was then derived by the Boltzmann transport equations. Details can be found in the **Supplementary Materials**.

***Sound velocity measurement*:** Sound velocity measurements were carried out using a pulse-echo transducer setup with both longitudinal and transverse transducers (Olympus 5072PR Pulser/Receiver).

Theoretical calculations: Density functional theory calculations were performed via the Quantum Espresso[64,66]. A norm-conserving (NC) technique was chosen to model the electron-ion interaction for the Sn, Sb, Ge, Mn, and Te atoms. The parameterization by Predew, Burke, and Ernzerfhof (PBE) based on generalized gradient approximation (GGA) was applied to calculate the band structure[67,69,106], and the cutoff energy for the wave function was set to 82 Ry. 3 × 3 × 3 supercells containing 27 Sn and 27 Te sites was

constructed and a 6 × 6 × 6 k mesh was adopted for the Brillouin zone integration. Some Sn sites were replaced by Ge, Sb, Pb, and a vacancy to simulate the doped system. Both cell parameters and atomic positions were fully relaxed until the force on each atom was less than 0.0001eV/Å.

5.3 Results and Discussion

5.3.1 Sb_2Te_3 Alloying Effect

5.3.1.1 Crystallographic Study

Series of Sb_2T_3 doped samples, $(Sn_{0.98}Ge_{0.05}Te)_{1-x}(Sb_2Te_3)_x$ ($x = 0$, 0.03, 0.06, 0.09), were synthesised and their PXRD patterns are shown in **Figure 5.1** (a). All samples adopt the rock-salt structure (space group # 225, $Fm\bar{3}m$), and no impurities could be detected. Cell parameters were extracted by the Retived refinement using the Rietica software[107]. **Figure 5.1**(b) shows the cell parameter (a) as a function of doping concentration. The linear trend suggests high solubility of Sb_2Te_3 in $Sn_{0.98}Ge_{0.05}Te$.

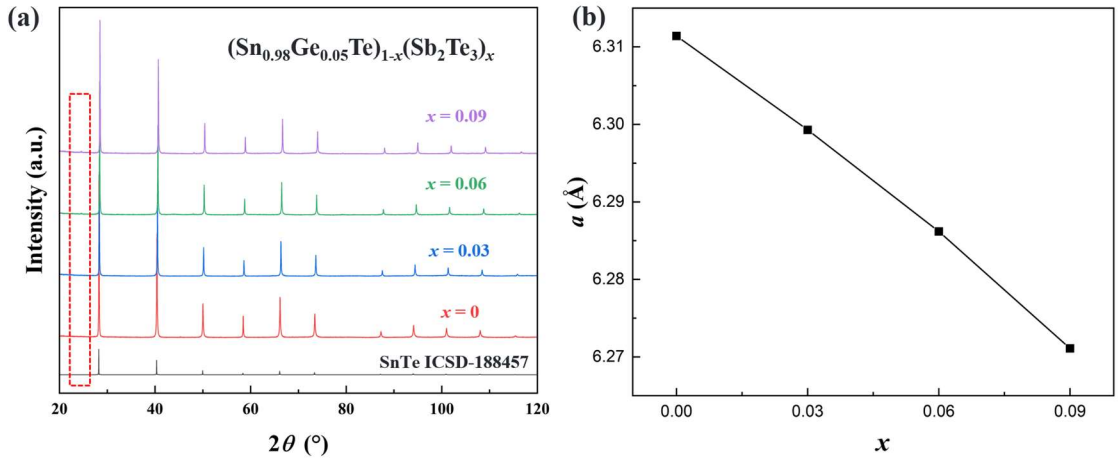

Figure 5.1. (a) XRD pattern[71] and (b) cell parameters of $(Sn_{0.98}Ge_{0.05}Te)_{1-x}(Sb_2Te_3)_x$ ($x = 0$, 0.03, 0.06, 0.09).

It should be noted that a small (111) peak at around 25° emerged after doping with Sb_2Te_3 (highlighted by the red box), and its intensity increases with the alloying. For the face-centered cubic lattice, if we set Sn at origin, then the intensity of the diffraction peak is given as:

$$I_{hkl} = |S_{hkl}|^2 \tag{5.1}$$

$$S_{hkl} = [f_{\mathrm{Sn}} + (-1)^h f_{\mathrm{Te}}][(-1)^{h+k} + (-1)^{k+l} + (-1)^{h+l}] \tag{5.2}$$

$$f_A = \int \rho(r) e^{iqr} d^3r \tag{5.3}$$

Where h, k, and l are Miller indexes, I_{hkl} is the diffraction intensity of the (hkl) crystal plane, S_{hkl} is the corresponding structural factor, f_{Sn} and f_{Te} are the atomic form factor of Sn and Te sites, respectively. The value of the atomic form factor could be determined by equation (3) which is just the Fourier transform of the average electron density of the lattice site A. r is the real space vector, q is the reciprocal lattice vector, ρ is the real space electron density. In our case, the intensity from the (111) plane is

$$I_{111} = 9(f_{\mathrm{Sn}} - f_{\mathrm{Te}})^2 \tag{5.4}$$

For pristine SnTe, the difference between the two atomic form factors is small due to the relatively similar electronic configuration between Sn and Te atom. As a result, the intensity of (111) is extremely weak. After alloying with Sb_2Te_3, a vast amount of Sn vacancies is introduced, which lowers the average electron density of the Sn site. This is justified by the refinement result, which showing the reduced occupation on the Sn site (**Table S5.3**). Based on equation (3), the reduced average electron density will lower the atomic form factor of the Sn site. As a result, the intensity of the (111) peak is increased.

5.3.1.2 Electric Properties Analysis

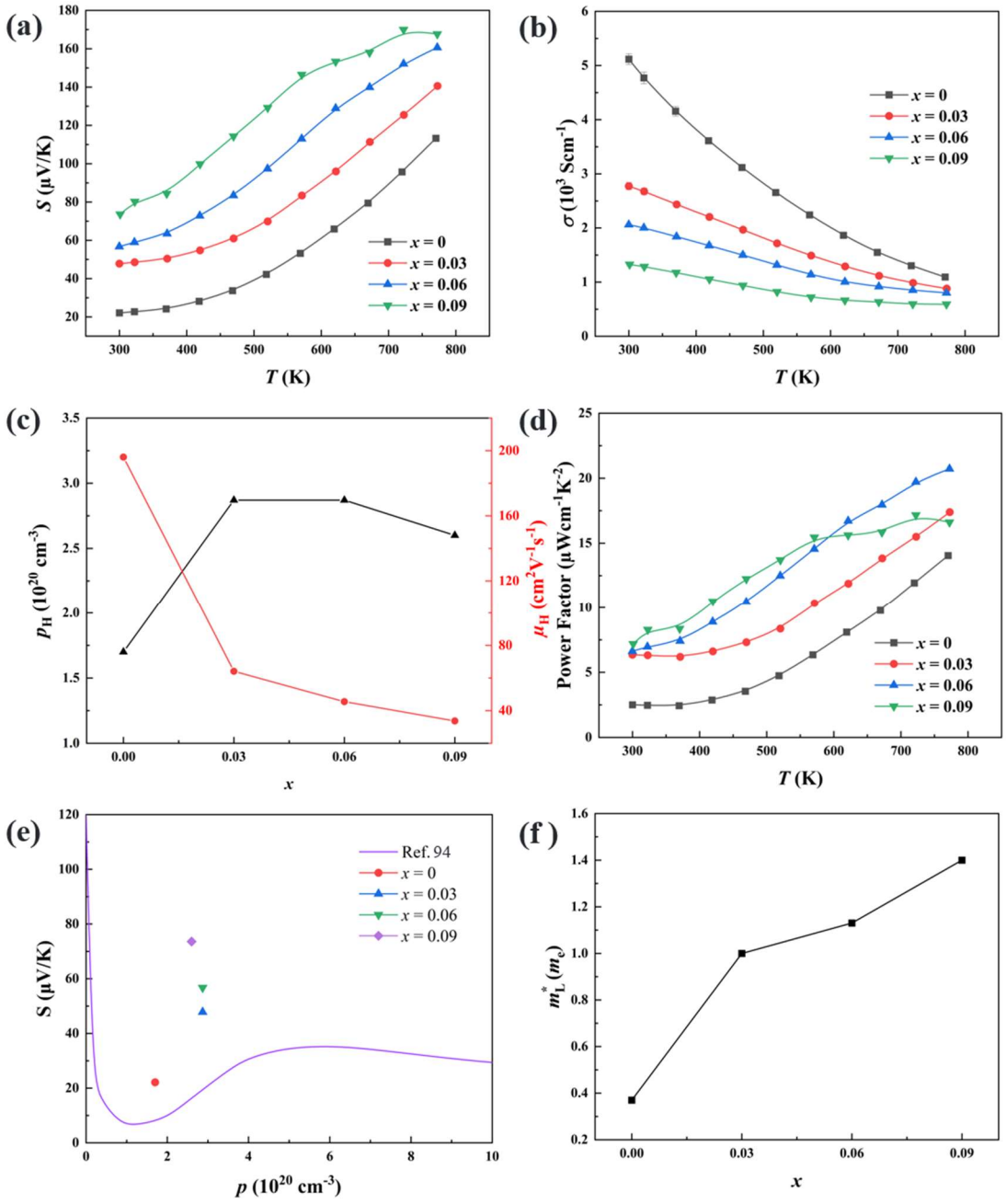

Figure 5.2. (a) Seebeck coefficient, (b) electrical conductivity, (c) power factor, (d) Hall data (e) room-temperature Pisarenko plot[94] and (f) DOS effective mass of $(Sn_{0.98}Ge_{0.05}Te)_{1-x}(Sb_2Te_3)_x$ (x = 0, 0.03, 0.06, 0.09).

The transport properties are presented in **Figure 5.2** (a) ~ (d). As can be seen, both resistivity and Seebeck coefficient were increased systematically upon Sb_2Te_3 alloying, as shown in **Figure 5.2** (a) and (b). Hall measurement revealed that Sb_2Te_3 alloying increased the carrier concentration from 1.69×10^{20} cm^{-3} to 2.6×10^{20} cm^{-3} while the carrier mobility was drastically reduced from 196 $cm^2V^{-1}s^{-1}$ to merely 34 $cm^2V^{-1}s^{-1}$, see **Figure 5.2** (d). Caused by the poor carrier mobility, the power factor saturated at $x = 0.09$, **Figure 5.2** (c). By adapting the data points into the Pisarenko plot (**Figure 5.2** (e)), we found that Sb_2Te_3 doping gradually pushed the data points above the theoretical curve, indicating an improved DOS effective mass. To verify this observation, a temperature-dependent two-band (TD-TB) model was established to simulate transport properties. The detailed calculation procedure can be found in the **Supporting Information**. The simulation result showed that, the DOS effective mass of the L band increased monotonically upon the Sb_2Te_3 doping, as indicated in **Figure 5.2** (f).

The band structures of $Sn_{0.98}Ge_{0.05}Te$ before and after the Sb_2Te_3 alloying were calculated and shown in **Figure 5.3** (a) and (b). Here, to simplify the calculation, the doping effect of Ge element was neglected. A comparison of the band structure and DOS before and after the Ge doping was presented in **Figure S5.1**, the result indicating that Ge doping show neglectable impact on the electronic structure of SnTe. As can be seen, Sb_2Te_3 alloying shift the direct band gap at L point into an indirect band gap between the L and Σ points. As a result, the modified band gap reduces the interaction between the CBM and VBM at the L point, which effectively flattens the L band and increases the DOS effective mass.

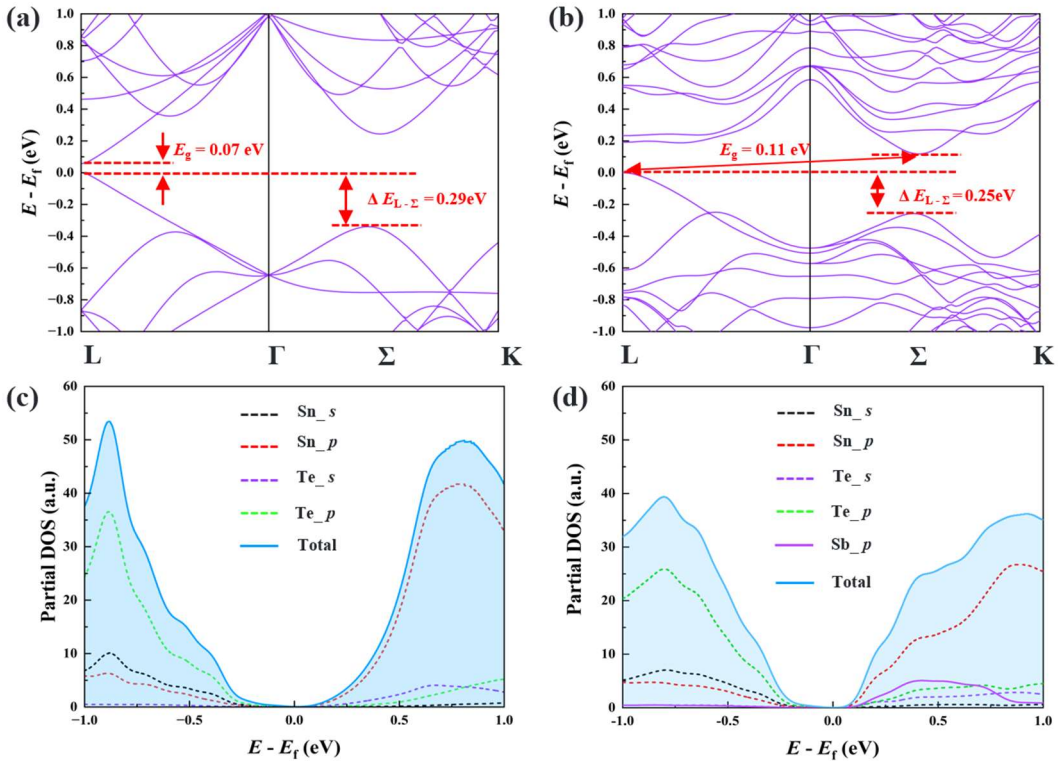

Figure 5.3. (a) Band structure and (c) DOS of $Sn_{27}Te_{27}$. (b) Band structure and (d) DOS of $Sn_{24}Sb_2Te_{27}$. The introduction of the Sb_2Te_3 shift the direct band gap at L point into an indirect band gap between L and Σ points.

5.3.1.3 Thermal Conductivity

Using a two-band model based on the discussion in **Section 2.3.3**, the Lorenz numbers L are calculated, and the electrical thermal conductivity is then calculated using the Wiedemann-Franz law:

$$\kappa_{\mathrm{e}} = L\sigma T \tag{5}$$

Where κ_e is the electrical thermal conductivity. The lattice thermal conductivity κ_l was obtained by subtracting the κ_e from the total thermal conductivity κ, and the result is shown in **Figure 5.4**. The Sb_2Te_3 alloying suppressed κ_e and κ_l simultaneously, as a result, the room temperature thermal conductivity is reduced by 70%. The suppression of the electrical thermal conductivity originated from the significantly reduced carrier mobility (**Figure 5.2** (d)), which was caused by the strong electron-vacancy scattering, while the reduction in the lattice thermal conductivity was attributed to the various crystal defects inside the structure. These defects induced a strong lattice anharmonicity, which contributed to the phonon scattering process. This statement can be proved by the significantly reduced bulk sound velocity, which is given in **Table S5.4**.

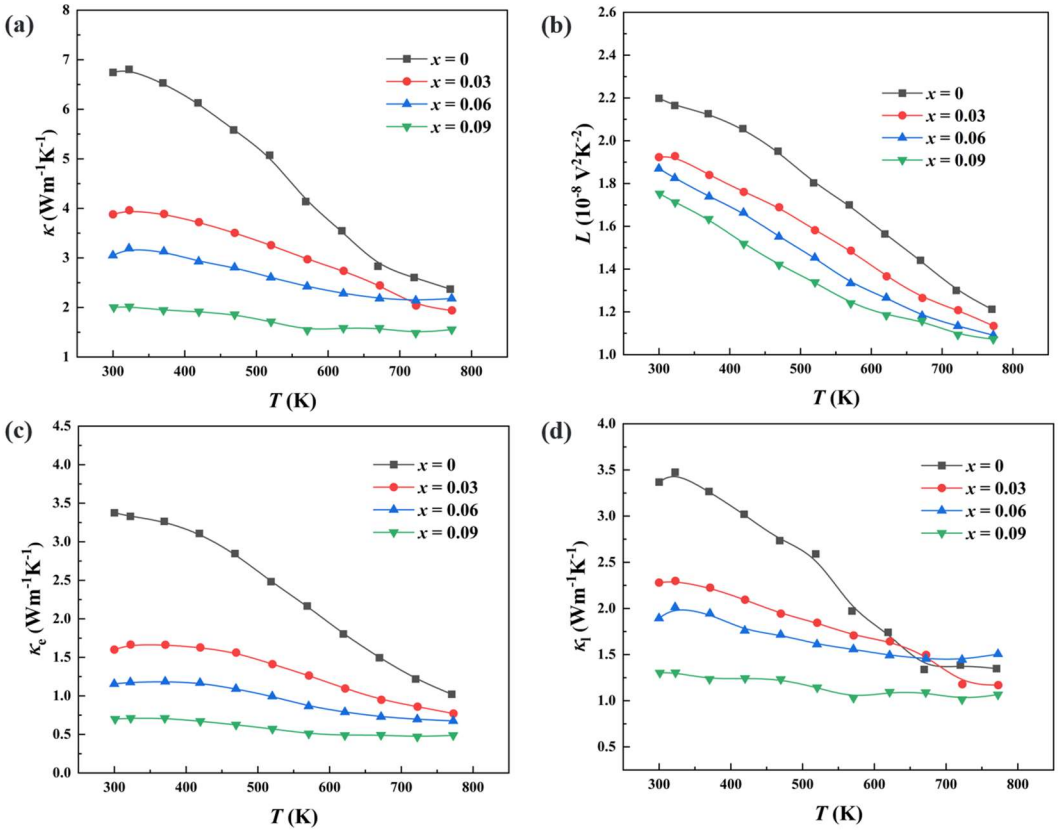

Figure 5.4. (a) Total thermal conductivity, (b) Lorenz number, (c) electrical thermal conductivity, (d) lattice thermal conductivity of $(Sn_{0.98}Ge_{0.05}Te)_{1-x}(Sb_2Te_3)_x$ (x = 0, 0.03, 0.06, 0.09).

5.3.2 Vacancy Engineering via Pb Compensation

5.3.2.1 Proofs of Pb Compensation

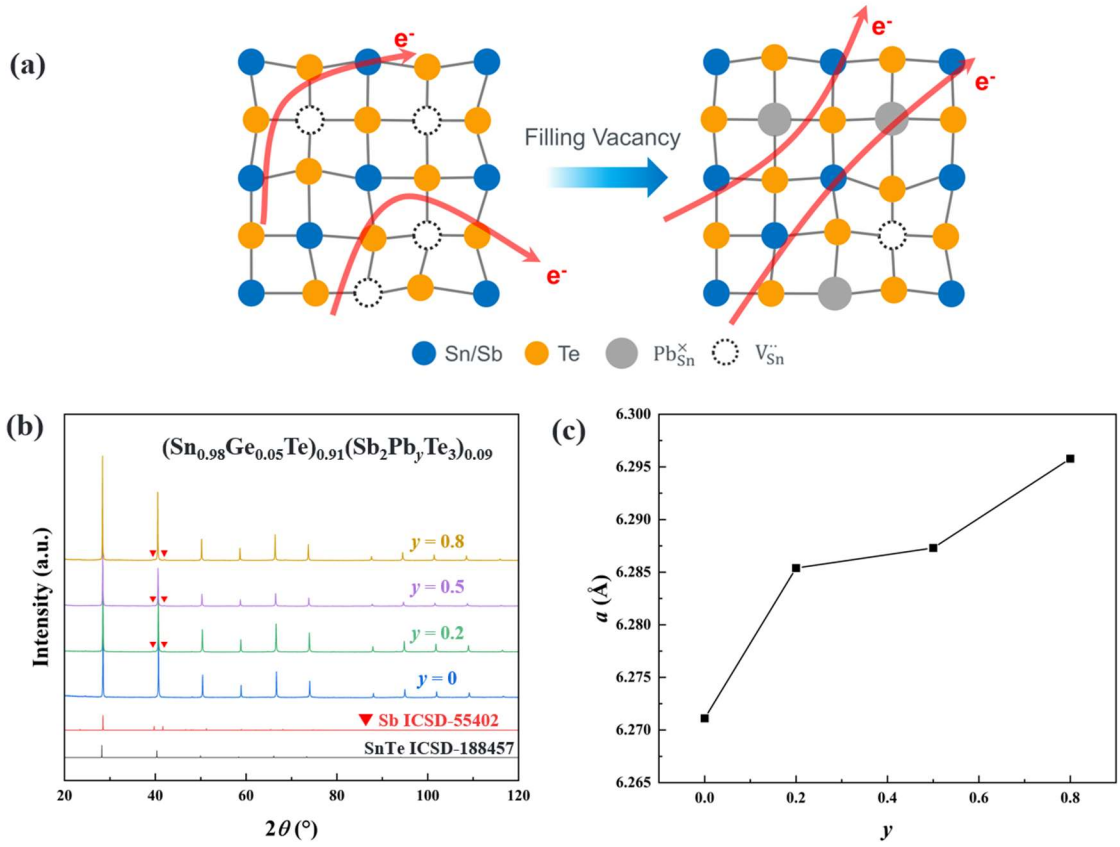

Figure 5.5. (a) A demonstration of Pb compensation. (b) Powder XRD pattern[71,108] and (c) cell parameter of $(Sn_{0.98}Ge_{0.05}Te)_{0.91}(Sb_2Pb_yTe_3)_{0.09}$.

Based on the above discussion, the thermoelectric performance of the SnTe-Sb_2Te_3 system was limited by the poor carrier mobility caused by the cation vacancy scattering. To optimize the carrier mobility, Sn vacancies were partially compensated via Pb doping, as demonstrated in **Figure 5.5** (a). Series of Pb compensated samples, $(Sn_{0.98}Ge_{0.05}Te)_{0.91}(Sb_2Pb_yTe_3)_{0.09}$ (y = 0, 0.02, 0.05, 0.08), were synthesised and their PXRD pattern are given

in **Figure 5.5** (b). All samples adopt the rock-salt structure, and Sb precipitates were found in all Pb-compensated samples, as marked by the red triangles. The crystallographic information extracted via Rietveld refinement is listed in **Table S5.3**. As, shown in **Figure 5.5** (c), the cell parameter increases monotonically, indicating the successful introduction of Pb into the lattice.

Single crystal XRD showed that the occupancy of the cation site rises upon Pb compensation. It should be noted that such result can only indicate that the average electron density at the cation site increases, and this could be caused by two possible processes: Pb compensation process (CP) where $V_{Sn}^{\cdot\cdot}$ defects filled by Pb elements and Pb substitution process (SP) where Sb_{Sn}' substituted by Pb elements.

Here, $V_{Sn}^{\cdot\cdot}$ represents a Sn vacancy with 2 positive charges and Sb_{Sn}' is a Sb atom on the Sn site with one negative charge. CP process will annihilate two holes, while the SP one will generate 1 hole carrier per each Pb atom introduced. The existence of SP can be directly proved by the presence of Sb precipitations, as shown in **Figure 5.5** (b). To also prove the existence of CP process, in the following discussion, we provide three proofs.

ZEM and Hall effect data were presented in **Figure 5.6**. Pb compensation slightly reduced the Seebeck coefficient in the low-temperature range (300 ~ 600K) and effectively reduced the resistivity throughout the whole temperature range. As a result, the power factor was improved by ~ 15% when $y = 0.5$. Room-temperature Hall measurement showed that Pb compensation effectively improved the mobility from 33.40 $cm^2V^{-1}s^{-1}$ to 56.38 $cm^2V^{-1}s^{-1}$, which explains the reduced resistivity. Meanwhile, the carrier concentration is

reduced from 2.60 × 10^{20} cm^{-3} to 1.87 × 10^{20} cm^{-3} (**Figure 5.6** (d)), and this supports the CP. The DOS effective mass was also decreased monotonically upon the Pb doping, as shown in **Figure 5.6** (f). Band structures that corresponding to both CP and SP, are presented in **Figure 5.7** (a) and (b).

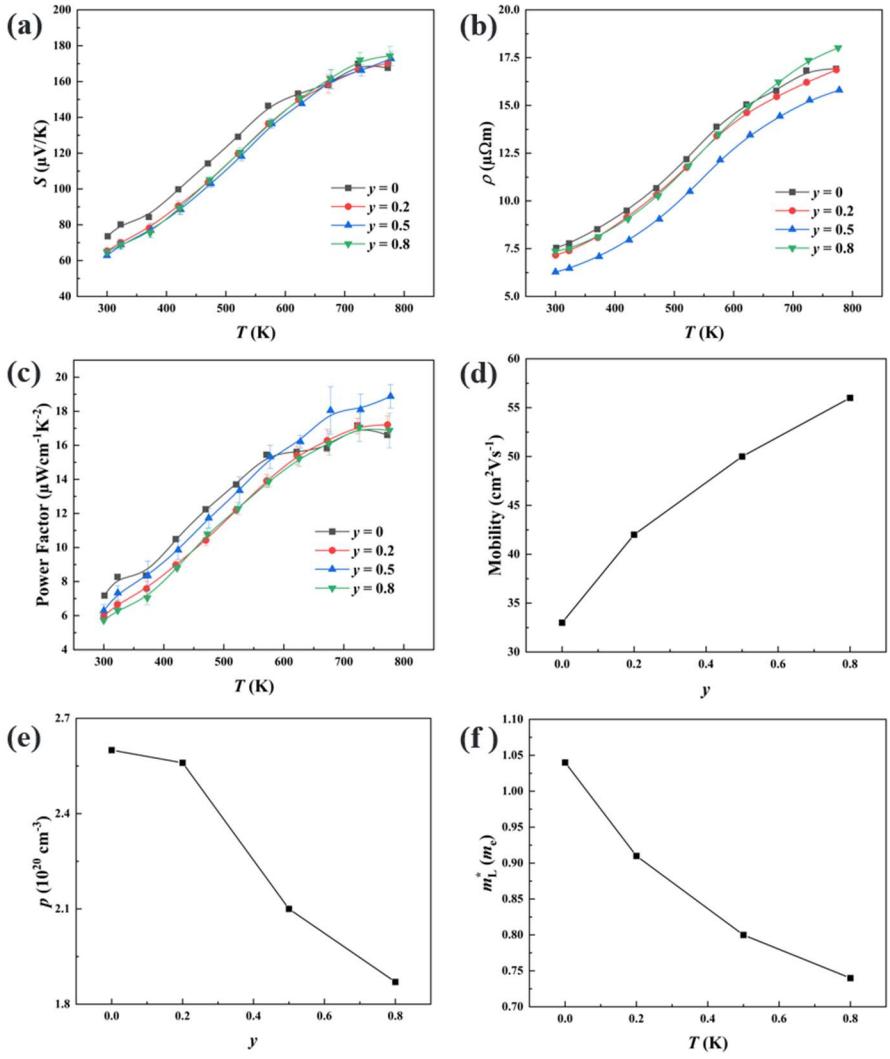

Figure 5.6. (a) Seebeck coefficient, (b) resistivity, (c) power factor, (d) mobility, (e) Hall carrier concentration and (f) DOS effective mass of $(Sn_{0.98}Ge_{0.05}Te)_{0.91}(Sb_2Pb_yTe_3)_{0.09}$.

It was found that when replacing the vacancy with Pb (CP, $Sn_{24}Sb_2PbTe_{27}$), the indirect band gap shifts back into a direct band gap at the L point and the value is even smaller than for the undoped sample. As a result, the interaction between the CBM and VBM is intensified by the Pb compensation, which fits well with the observed reduction of the L band DOS effective mass. In the meantime, replacing one Sb with Pb atom (SP, $Sn_{24}SbPbTe_{27}$) shows neglectable effect on the band morphology which further proves the presence of CP.

The temperature-dependent mobility of base material ($x = 0$, $y = 0$), alloyed sample ($x = 0.09$, $y = 0$) and alloyed + compensated sample ($x = 0.09$, $y = 0.5$) were measured, and the results are presented in **Figure 5.7** (d). As one can see, Sb_2Te_3 alloying drastically reduces the mobility throughout the whole temperature range but shows a weak temperature-dependency. After the introduction of Pb element, the low-temperature mobility was effectively improved, and the temperature-dependency was altered. The scattering factors r ($\mu \sim T^r$) were extracted from the mobility vs. temperature curves to determine the scattering mechanism. The r values of 1.5, -1.5 and 0 indicates ionized impurity (II) scattering, acoustic phonon (AP) scattering and mixed scattering, respectively. The base material shows r = -0.4936 throughout the whole temperature range, suggesting a dominant AP scattering mixed with the II scattering induced by the Ge dopant. The scattering factor of the Sb_2Te_3-alloyed sample is 0.0259, indicating that the II scattering controls the charge transport. Upon the Pb introduction, the AP scattering takes over, and r reduces to -2.123 for $T > 475$K, suggesting that the point defect concentration was effectively reduced. This phenomenon once again supports the occurrence of the CP.

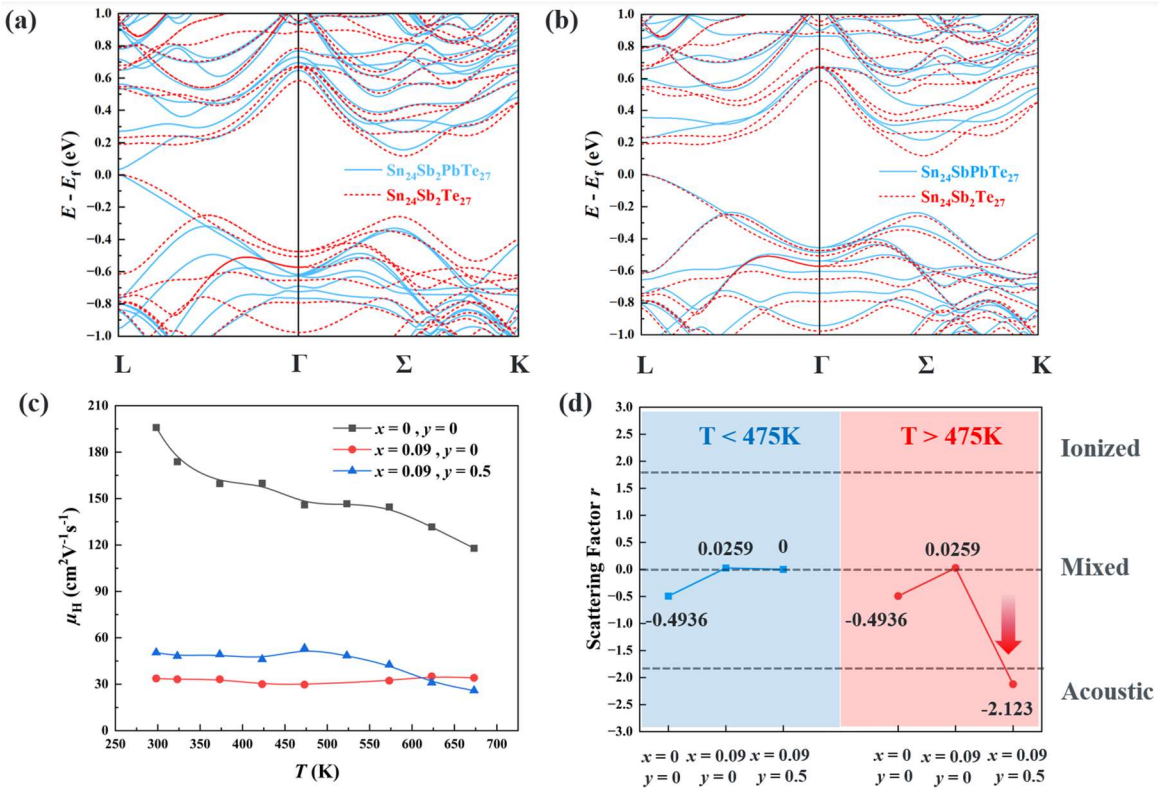

Figure 5.7. Band structure of (a) $Sn_{24}Sb_2PbTe_{27}$ and (b) $Sn_{24}SbPbTe_{27}$ which corresponds to the CP and SP processes, respectively. (c) Temperature-dependent mobility and (d) the fitted scattering factor under both low and high-temperature range.

In summary, we have provided 3 evidences for the existence of CP. First, while CP process annihilates two holes, SP generates one hole. The Hall effect data indicating a reduction on the carrier concentration, indicating the hole concentration reduction process CP exist. Second, the band structures which correspond to CP and SP were presented in **Figure 5.7** (a) and (b). It was found that SP process show neglectable effect on the band structure while CP sharpens the L band edge, which is consistent with the reduced DOS

effective mass. Finally, Pb compensation reduced the II scattering intensity, indicating a reduced cation vacancy concentration, consistence with the CP process.

5.3.2.2 Thermal Conductivity

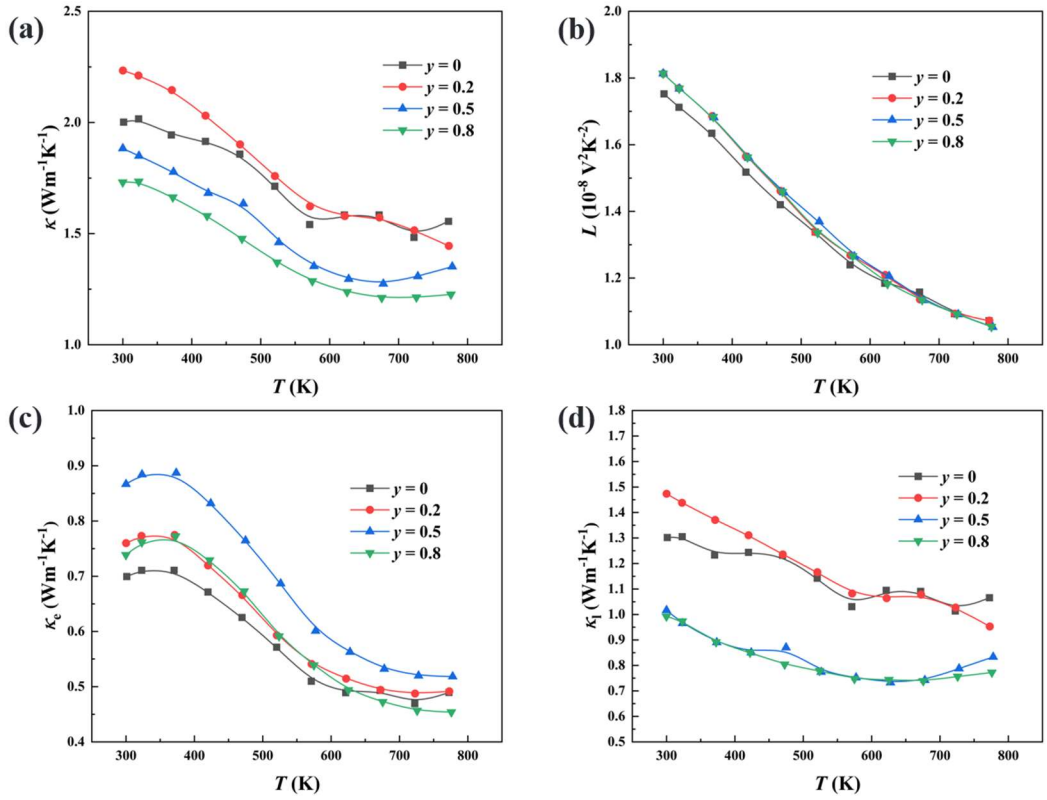

Figure 5.8. (a) Total thermal conductivity, (b) Lorenz number, (c) electrical thermal conductivity and (d) lattice thermal conductivity for $(Sn_{0.98}Ge_{0.05}Te)_{0.91}(Sb_2Pb_yTe_3)_{0.09}$ (y = 0, 0.2, 0.5, 0.8), respectively.

Figure 5.8 showed the LFA data for the Pb-doped samples. Interestingly, Pb doping reduced the total thermal conductivity systematically. While the Lorenz number showed neglectable changes, the electrical thermal conductivity was increased for 25%, which was due to the optimized carrier mobility. Meanwhile, Pb compensation suppressed the lattice

thermal conductivity significantly throughout the whole temperature range. Eventually, the overall total thermal conductivity is effectively suppressed upon the Pb compensation. This can be due to both Pb substitution and Sb precipitation.

5.3.2.3 Microstructure Analysis and Role of Sb Precipitates on Thermal Conductivity

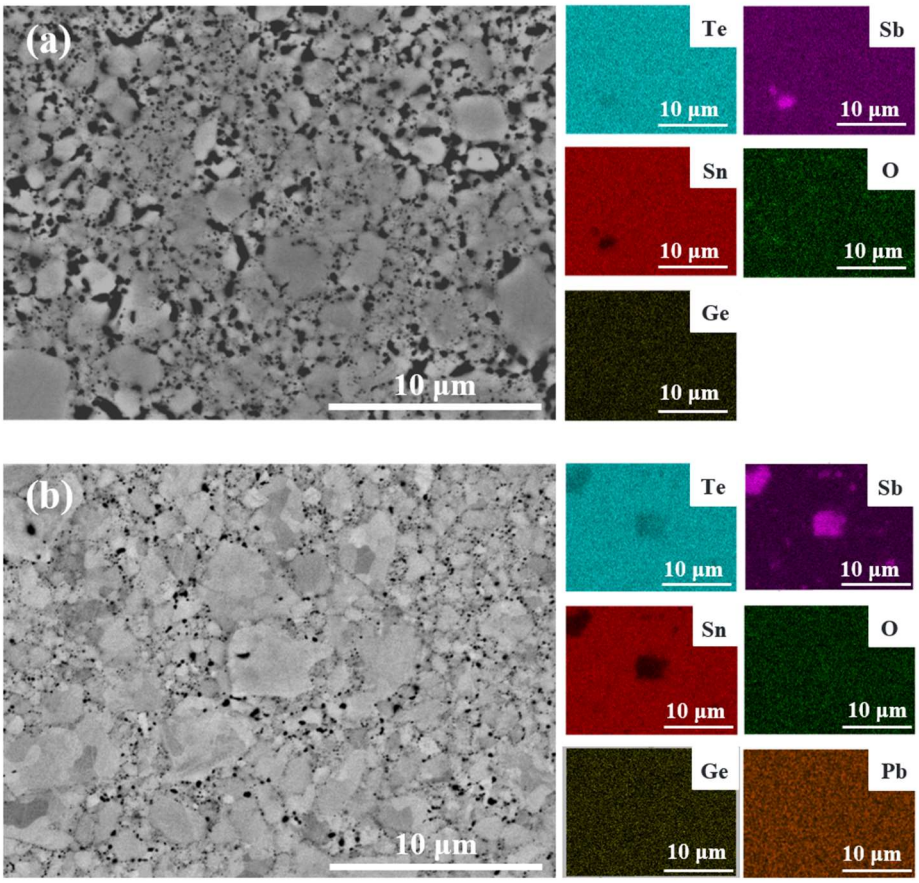

Figure 5.9. Back scattering image and elemental mapping of (a) $(Sn_{0.98}Ge_{0.05}Te)_{0.91}(Sb_2Te_3)_{0.09}$ and (b) $(Sn_{0.98}Ge_{0.05}Te)_{0.91}(Sb_2Pb_{0.5}Te_3)_{0.09}$, respectively.

To gain better understanding of the reduced lattice thermal conductivity, the SEM analysis before and after the Pb compensation was performed (**Figure 5.9)**. It should be noted that the black areas in **Figure 5.9** (a) are pores which were introduced during the

polishing. In agreement with the X-ray results, Sb precipitates are observed upon the Pb compensation.

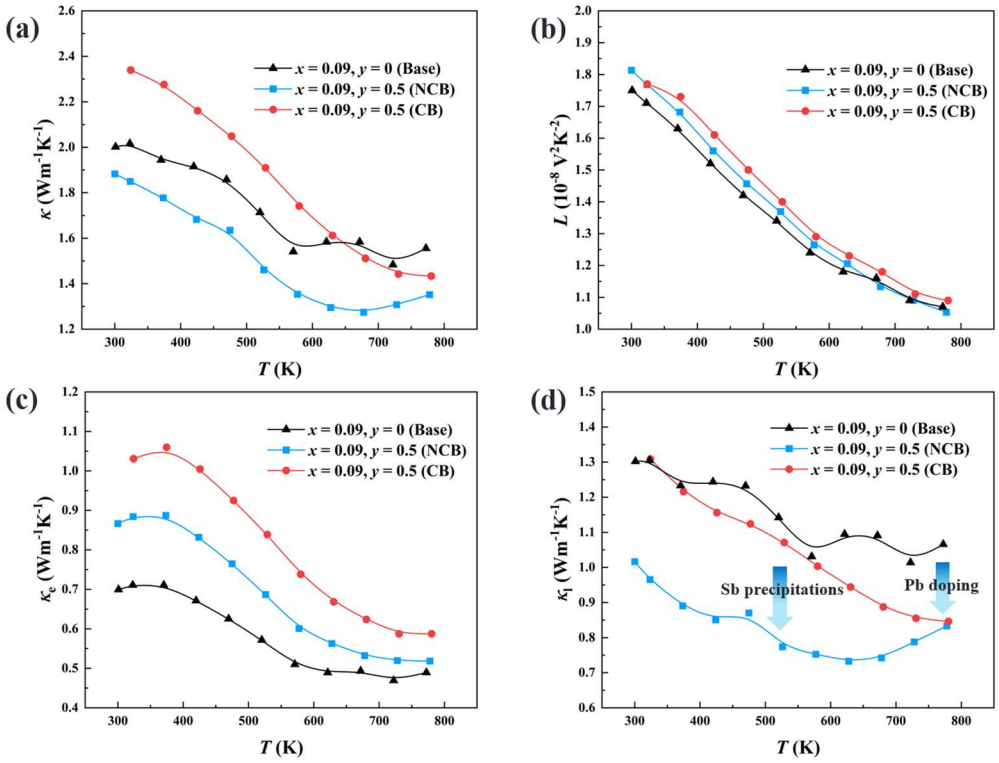

Figure 5.10. A comparison of (a) total thermal conductivity, (b) Lorenz number, (c) electrical conductivity and (d) lattice thermal conductivity between Base, CB and NCB samples.

To elucidate the effect of Sb precipitates and Pb doping on the lattice thermal conductivity, a sample free of Sb precipitates but with the same Pb concentration was synthesised. To prevent Sb precipitation, the sample needed to be charge balanced. The compositions of base material (Base), charge balanced (CB) sample and the non-charge balanced (NCB) sample are $(Sn_{0.98}Ge_{0.05}Te)_{0.91}$ $(Sb_2Te_3)_{0.09}$, $(Sn_{0.98}Ge_{0.05}Te)_{0.91}$ $(Sb_{1.4644}Pb_{0.5}Te_3)_{0.09}$ and $(Sn_{0.98}Ge_{0.05}Te)_{0.91}$ $(Sb_2Pb_{0.5}Te_3)_{0.09}$, respectively. The XRD

patterns are shown in **Figure S5.5**. No secondary phases could be detected in the CB samples, indicating that the Sb precipitates were successfully removed. Electrical properties of the CB and NCB samples are shown in **Figure S5.6**. As can be seen, removing the Sb precipitates reduced the Seebeck coefficient and resistivity, which could be attributed to the increased carrier concentration. The thermal conductivity data are shown in **Figure 5.10**. Comparing Base and CB, it showed that Pb substitution reduced the mid-temperature (500K~800K) part of the lattice thermal conductivity. The subsequent formation of Sb precipitates effectively suppressed the lattice thermal conductivity throughout the whole temperature range, as indicated by comparing CB and NCB samples.

5.3.3 Figure of Merit

Figure 5.11 shows the figure of merit, *zT,* values obtained in this work. Sb_2Te_3 alloying increases the peak and average *zT* from 0.5 and 0.13 to 0.8 and 0.46, which is improvement of 60% and 254%, respectively. Subsequent Pb doping further improves the peak and average *zT* by 21% and 22%. Comparison of the *zT* values of our materials with those of other SnTe-based thermoelectric systems is provided in **Figure 5.11** (c). As one can see, our strategy allowed to effectively optimize the thermoelectric performance throughout the whole temperature range, and the presented materials outperform most of the state-of-the-art SnTe-based thermoelectrics.

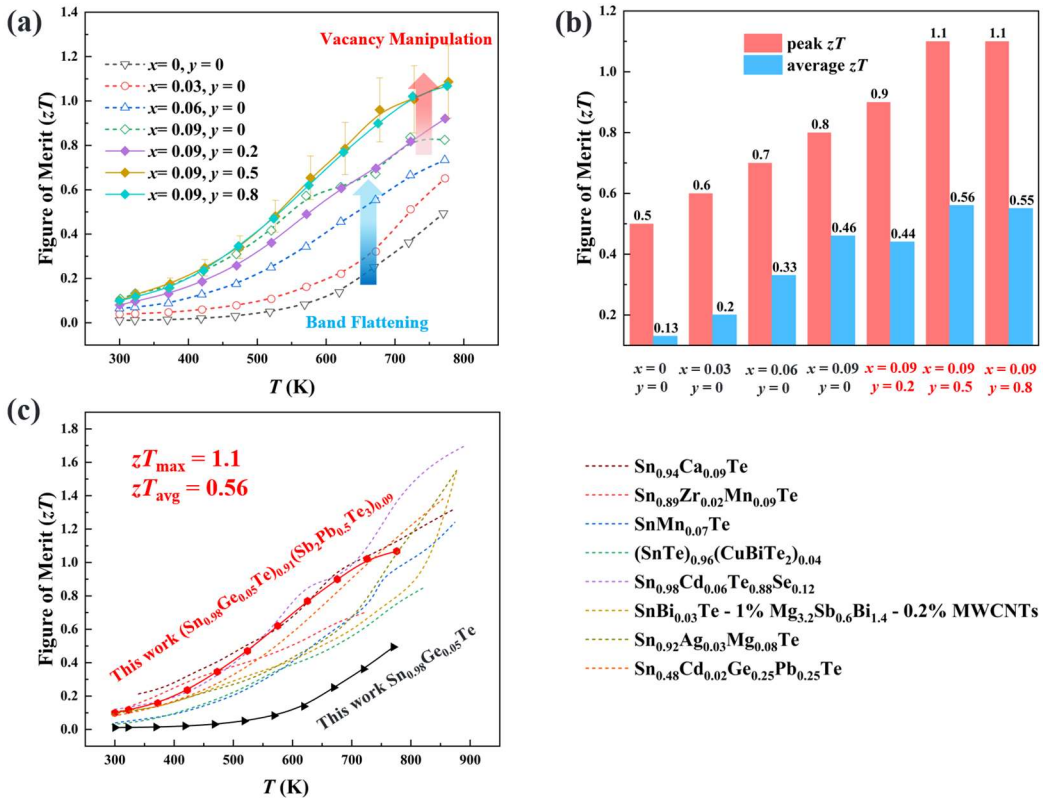

Figure 5.11. (a) Calculated zT values, (b) peak and average zT values for $(Sn_{0.98}Ge_{0.05}Te)_{1-x}(Sn_2Pb_yTe_3)_x$ (c) Comparing the optimal zT value obtained in this work with previous articles [97,98,109–113].

5.4 Conclusion

The TE properties of SnTe-Sb_2Te_3 system were thoroughly investigated. DFT calculations indicate that Sb_2Te_3 doping shifts the direct band gap at the L point to an indirect band gap between the L and Σ points and reduces the CBM – VBM interaction at the L point. Subsequent experimental studies showed that Sb_2Te_3 alloying effectively improves the Seebeck coefficient and suppresses the thermal conductivity. Our TD-TB simulation showed that Sb_2Te_3 alloying effectively improves the DOS effective mass by 225%, which agrees well with the DFT calculations. In the meantime, room-temperature

Hall measurements revealed drastic degradation of the carrier mobility upon the Sb_2Te_3 alloying, which is caused by the strong vacancy scattering. To further improve the thermoelectric performance, cation vacancies were partially compensated via Pb doping, which successfully reduced the resistivity. As a result, the high-temperature power factor was improved by ~ 15% when $y = 0.5$. In the meantime, LFA measurement revealed that Pb doping effectively suppressed the thermal conductivity by 30%, which is attributed to the reduced lattice thermal conductivity. Such reduction is due to the simultaneous contribution from Pb substitution and Sb precipitation upon Pb compensation which contributes to the phonon scattering process. As a result, a peak zT of 1.1 at 778K and an average zT of 0.56 from 300K to 778K is achieved in $(Sn_{0.98}Ge_{0.05}Te)_{0.91}(Sb_2Pb_{0.5}Te)_{0.09}$, which is one of the best SnTe-based thermoelectric systems. This work provides demonstrates that vacancy compensation can effectively optimize the transport properties of the SnTe-Sb_2Te_3 system and secure high thermoelectric performance in the SnTe-based thermoelectric materials.

5.5 Supplementary Materials

5.5.1 Ge Doping Effect

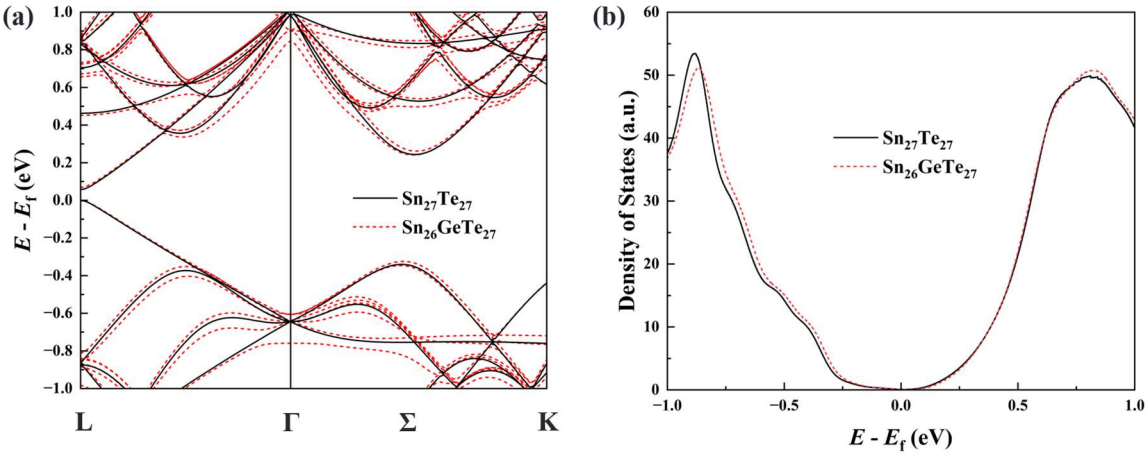

Figure S5.1. Doping effect of Ge. (a) Band structure and (b) density of states. The solid black line and red dash line represent the pristine SnTe and Ge doped SnTe, respectively.

5.5.2 BTE Simulation Results

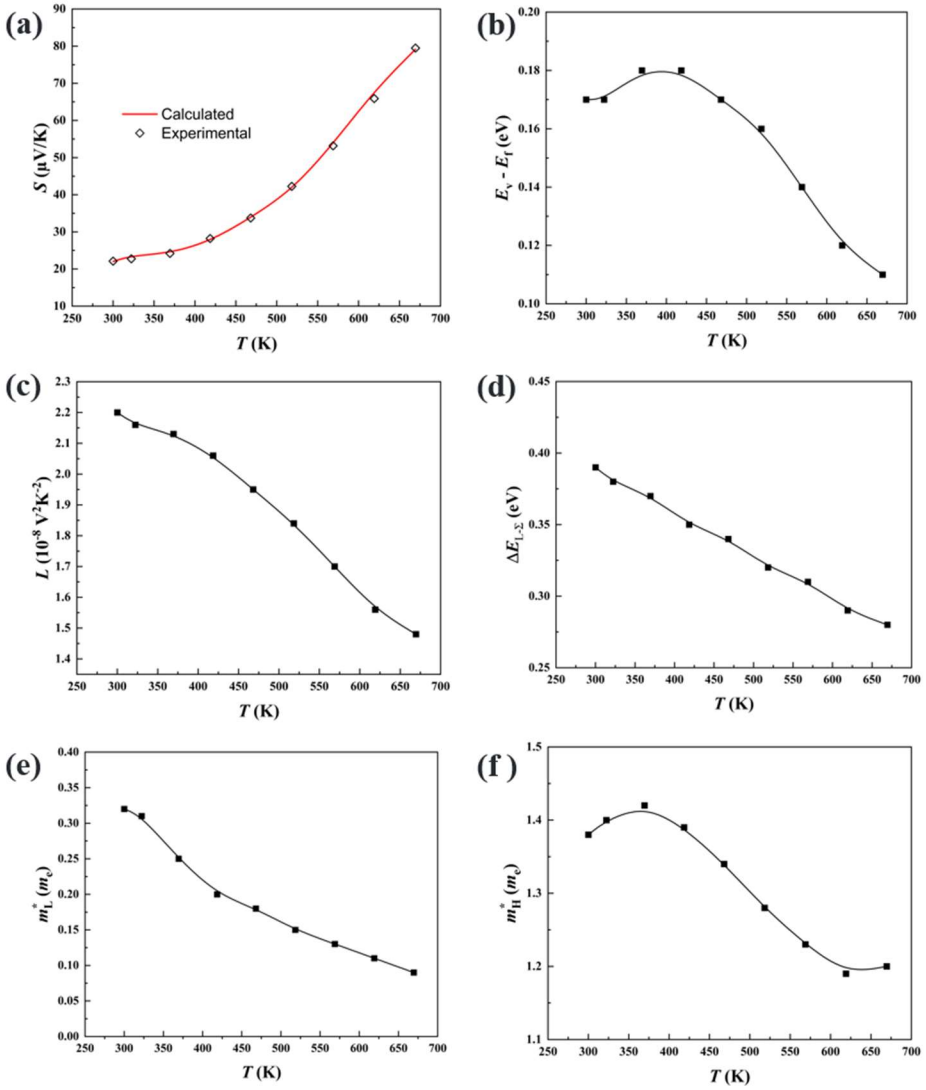

Figure S5.2. TD-TB simulation results for $Sn_{0.98}Ge_{0.05}Te$. (a) Seebeck coefficient, (b) energy separation between top of the valence band E_V and Fermi level E_f, (c) Lorenz number, (d) Energy separation between the L and Σ bands, (e) DOS effective mass of the L band, and (f) DOS effective mass of the Σ band.

As shown in **Figure S5.3** (a), most of the carriers are located at the L band, the contribution of the lower Σ band is neglectable. This was verified by comparing the Lorenz numbers calculated by the two-band model and single-band model. The simulation result shows that Σ band has little impact on the outcome. Therefore, for simplicity, we used the single band model to calculate the Lorenz number for all samples.

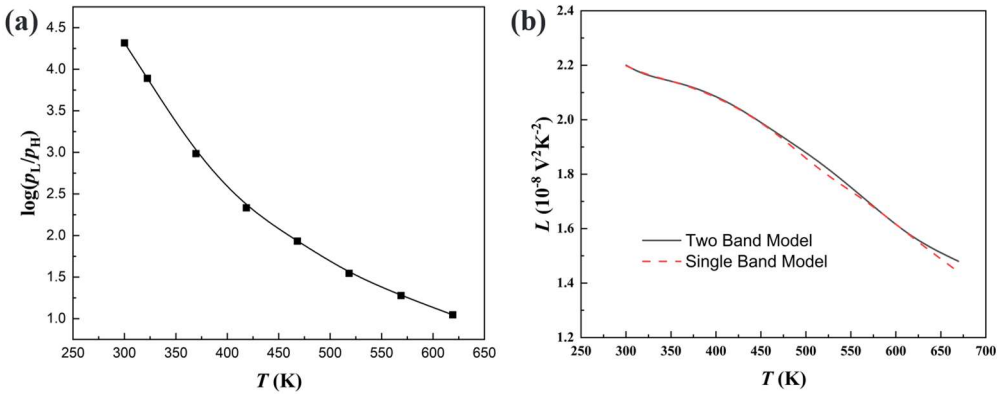

Figure S5.3. (a) log of the ratio between the carrier concentration distributed in the L band and Σ bands. (b) Lorenz number computed by the two-band model and single-band model. A solid black line represents to the two-band model, and a red dosh line represents the single band.

5.5.3 EBSD Analysis

Pb compensation increased the average grain size from 0.6 μm to 1.36 μm. $SnTe_3O_8$ (yellow area in phase maps) could be found along the grain boundaries, which is caused by the inevitable oxidation during the sample synthesis.

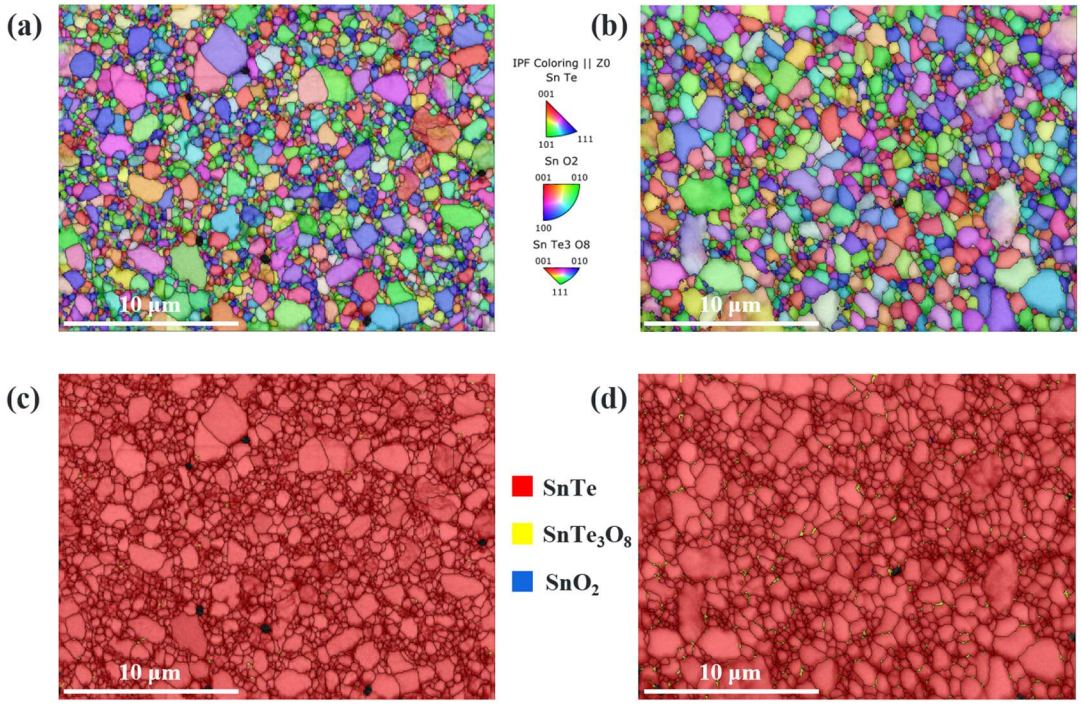

Figure S5.4. (a) and (b) EBSD map and (c) and (d) phase map of $(Sn_{0.98}Ge_{0.05}Te)_{0.91}(Sb_2Te_3)_{0.09}$ and $(Sn_{0.98}Ge_{0.05}Te)_{0.91}(Sb_2Pb_{0.5}Te_3)_{0.09}$, respectively.

5.5.4 Effect of Sb precipitation

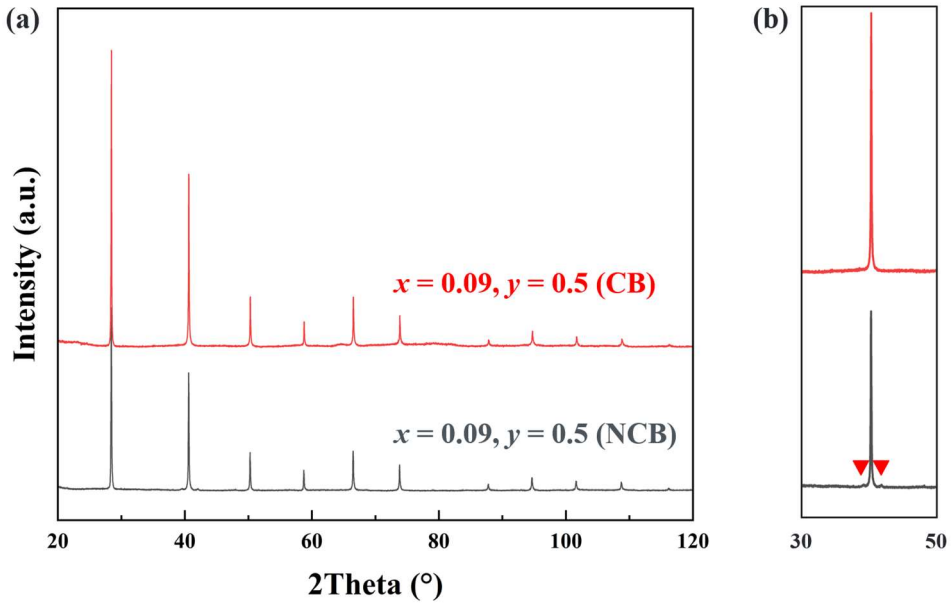

Figure S5.5. (a) Powder XRD pattern of the NCB and CB samples. (b) A zoom-in image of the pattern; the peaks marked by red triangles belong to Sb precipitates.

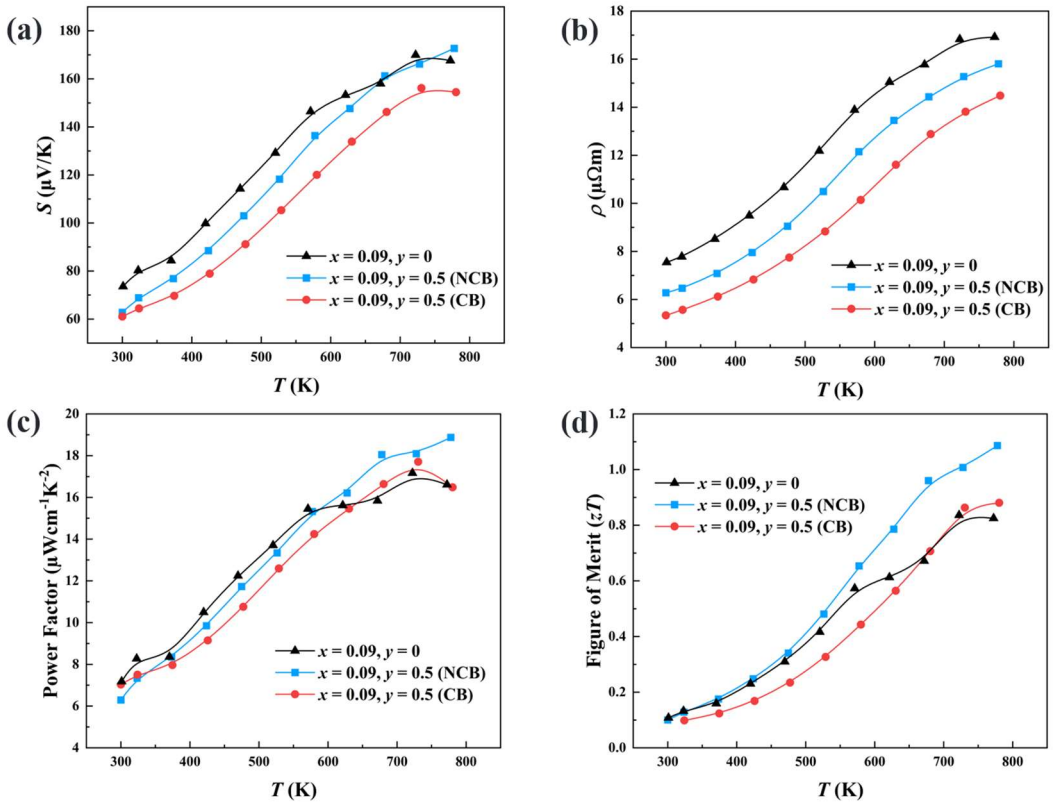

Figure S5.6. A comparison of (a) Seebeck coefficient, (b) resistivity, (c) power factor and (d) *zT* values between Base, CB and NCB samples.

The compositions of base material (Base), charge balanced (CB) sample and the non-charge balanced (NCB) sample are $(Sn_{0.98}Ge_{0.05}Te)_{0.91}$ $(Sb_2Te_3)_{0.09}$, $(Sn_{0.98}Ge_{0.05}Te)_{0.91}$ $(Sb_{1.4644}Pb_{0.5}Te_3)_{0.09}$ and $(Sn_{0.98}Ge_{0.05}Te)_{0.91}$ $(Sb_2Pb_{0.5}Te_3)_{0.09}$, respectively.

Table S5.1. Density of Samples.

Composition	ρ_M (gcm^{-3})	ρ_T (gcm^{-3})	Relative Density (%)
$x = 0, y = 0$	6.16	6.41	96.10
$x = 0.03, y = 0$	6.33	6.43	98.44
$x = 0.06, y = 0$	6.16	6.30	97.78
$x = 0.09, y = 0$	6.09	6.34	96.06
$x = 0.09, y = 0.2$	6.14	6.40	95.94
$x = 0.09, y = 0.5$	6.36	6.53	97.40
$x = 0.09, y = 0.8$	6.31	6.62	95.32

Table S5.2. Room-temperature Hall Data.

Composition	p_{Hall} (10^{20} cm^{-3})	μ_{Hall} ($cm^2V^{-1}s^{-1}$)	m_L^* (m_e)
$x = 0, y = 0$	1.89	195.91	0.32
$x = 0.03, y = 0$	2.87	64.11	0.79
$x = 0.06, y = 0$	2.87	45.51	0.87
$x = 0.09, y = 0$	2.60	33.40	1.04
$x = 0.09, y = 0.2$	2.56	41.83	0.91
$x = 0.09, y = 0.5$	2.10	50.42	0.80
$x = 0.09, y = 0.8$	1.87	56.38	0.74

Table S5.3. Selected crystallographic data, experiment details and refinement results for the $(Sn_{0.98}Ge_{0.05}Te)_{1-x}(Sb_2Pb_yTe_3)_x$ single crystals.

Composition	$x = 0$ $y = 0$	$x = 0.03$ $y = 0$	$x = 0.06$ $y = 0$	$x = 0.09$ $y = 0$	$x = 0.09$ $y = 0.2$	$x = 0.09$ $y = 0.5$	$x = 0.09$ $y = 0.8$
Sn Site Occupancy (%)	97.7(2)	95.7(5)	94.3(4)	92.87(1)	94.1(5)	95.1(3)	97.6(3)
Crystal System	Cubic						
Space Group	$Fm\bar{3}m$						
***a*, Å**	6.3030(7)	6.2879(7)	6.2775(7)	6.2672(7)	6.2751(7)	6.2756(7)	6.2858(7)
***Volume*, Å^3**	250.40(8)	248.61(8)	247.38(8)	246.16(8)	247.09(8)	247.15(8)	248.36(8)
Z	4						
μ/mm^{-1}	20.978	20.933	20.889	20.868	20.987	20.908	21.175
***F*(000)**	404	400	396	394	398	396	404
2Θ Range (°)	5.604 – 34.319	5.618- 34.413	5.627- 34.478	5.636- 32.135	5.629- 34.493	5.629- 34.490	5.619- 32.029
Index Ranges	$-10 \le h \le 10$ $-10 \le k \le 9$ $-10 \le l \le 10$	$-10 \le h \le 10$ $-9 \le k \le 10$ $-10 \le l \le 10$	$-10 \le h \le 10$ $-9 \le k \le 10$ $-10 \le l \le 9$	$-9 \le h \le 8$ $-9 \le k \le 9$ $-9 \le l \le 9$	$-10 \le h \le 9$ $-10 \le k \le 10$ $-8 \le l \le 10$	$-10 \le h \le 9$ $-10 \le k \le 9$ $-10 \le l \le 7$	$-9 \le h \le 9$ $-8 \le k \le 9$ $-7 \le l \le 9$
Reflections Collected	1587	1110	1102	1387	1095	1070	567
Data/Restraints/ Parameters	46/0/4	46/0/5	46/0/4	39/0/4	46/0/5	46/0/4	38/0/4
GOOF	1.240	1.067	0.937	0.908	1.193	1.293	1.139
R_1 (I>2σ (I))	0.0130	0.0109	0.0141	0.0052	0.0107	0.0258	0.0110
Largest diff. peak/hole (e/Å^3)	0.660/ -0.642	0.559/ -0.242	0.380/ -0.434	0.357/ -0.212	0.506/ -0.609	0.882/ -1.359	0.355/ -0.699

Table S5.4. Sound velocity measurement data. v_l is the longitudinal velocity, v_t is the transverse velocity and v is the bulk sound velocity.

Composition	v_l **(m/s)**	v_t **(m/s)**	v **(m/s)**
$x = 0$, $y = 0$	3300.8	1911.7	2121.8
$x = 0.03$, $y = 0$	3293.8	1898.2	2107.7
$x = 0.06$, $y = 0$	3201.2	1836.7	2040.2
$x = 0.09$, $y = 0$	2863.2	1694.0	1876.5
$x = 0.09$, $y = 0.2$	3191.7	1825.5	2028.3
$x = 0.09$, $y = 0.5$	3183.0	1841.7	2044.2
$x = 0.09$, $y = 0.8$	2927.3	1698.5	1884.8

Here v is given by:

$$v = \left[\frac{1}{3}\left(\frac{1}{v_l^3} + \frac{2}{v_t^3}\right)\right]^{-1/3} \quad \text{(S31)}$$

Chapter 6 Conclusion and Future Works

6.1 Conclusion

When applying a temperature gradient through a bulk material, the charge carriers inside the material will drift along (or against) the temperature gradient which is known as Seebeck effect. The thermodynamic driven force of such phenomenon is the difference in Fermi-Dirac distribution caused by the variation of temperature. By taking the first order derivative of the Fermi-Dirac distribution with respect to the temperature, we found two fluxes right above and below the Fermi energy. These fluxes are equal in intensity but point in the opposite direction. For a material with band gap (i.e., semiconductor), when the Fermi level is located near the band edge, one of the fluxes will show lower intensity in comparison with the other one due to the absence of available energy states (density of states). As a result, there will be a net flux induced by the temperature gradient. Utilizing this phenomenon, a generator that harvests thermal energy stored in the temperature gradient can be fabricated (**Figure 6.1** (a)), which currently received extensive attention.

In the aspect of electric properties, a good thermoelectric material should possess a complex Fermi surface morphology where sharp bands with high degeneracy contribute to the conductivity. Therefore, a large density of states and a good carrier mobility could be obtained simultaneously. On the other hand, to minimize the energy losses due to direct heat transfer and to stabilize a large temperature difference between hot side and cold side, it also requires the material to have a low thermal conductivity. The overall performance of a given material is evaluated via a dimensionless figure of merit zT value, which is given

by $zT = \frac{S^2\sigma}{\kappa}T = \frac{PF}{\kappa_e+\kappa_l}T$. These parameters are intrinsically coupled with each other, making thermoelectric material an extremely complex system, as shown in **Figure 6.1** (b).

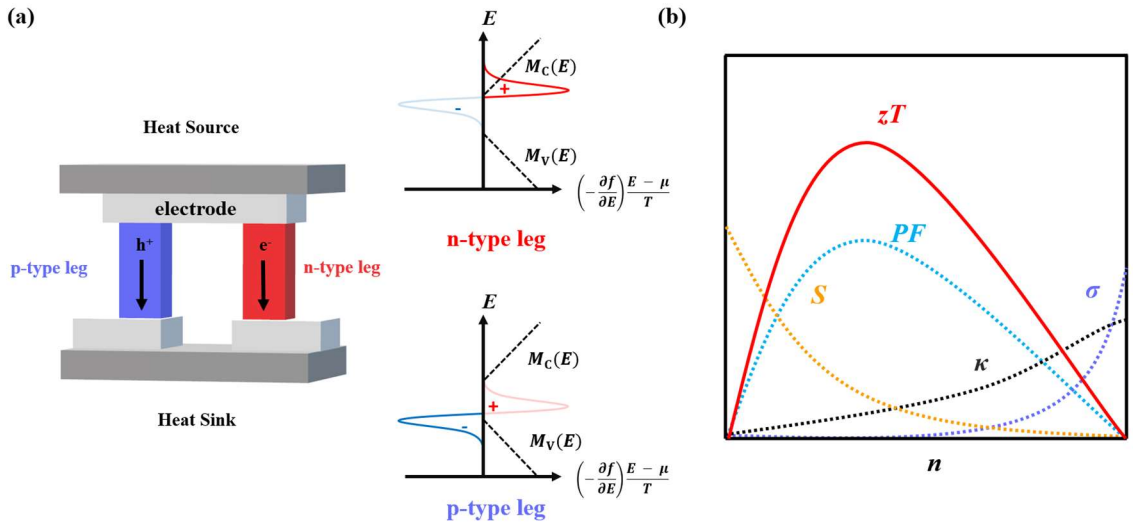

Figure 6.1 (a) two-leg thermoelectric energy generator. (b) A qualitative demonstration of the complex coupling of thermoelectric parameters.

In this thesis, a thorough summarization of our thermoelectrics related research was presented. Firstly, the electrical and thermal transport properties of the material were derived under near-equilibrium condition using Landauer approach. Based on this, multi-band model and Debye-Callaway model were presented which could be used to simulate the transport properties using experimental data. Then, a series of characterization methods used in our experiments were introduced. Finally, two research projects regarding the thermoelectric study of GeTe and SnTe-based materials were presented.

6.2 Future works

6.2.1 GeTe-based thermoelectric materials

Due to the unfavorable band structure of the low-temperature phase, the near-room-temperature *zT* value of GeTe is relatively low, which limits any further improvement on its overall average *zT* value. Segmenting room-temperature TE materials with mid-temperature GeTe-based materials to combine their peak performance within different working temperatures is, by far, the most effective way to optimize the overall device performance across a given temperature gradient[38,114–118]. However, extra interfaces are introduced during the segmentation. Though the device efficiency η is insensitive to the interfacial thermal resistance, it is reported that an interfacial electrical resistance of 10^{-4} Ωcm^2 is enough to reduce the efficiency by 15%[119]. Additionally, Snyder et al. pointed out that the relative current density μ ($\mu = J/\kappa \bigtriangledown T$, the ratio between electric current density and thermal current density) must be balanced between all segments to maximize the efficiency of a segmented TE leg[120]. To determine the optimal segmentation ratio, extensive device simulation is needed during the device fabrication. Based on the above discussion, one can see that although the segmenting method is a promising approach in improving the average *zT* value of GeTe, the associated interface problem drastically increases the system's complexity and limits the improvement. Therefore, there is an urgent need to develop novel segmentation methods which do not introduce any extra interfaces.

The degree of rhombohedral distortion in r-GeTe can be evaluated by the interaxial angle (α) and the Te displacement factor (γ). When the angle between the two primitive unit cell vectors is α and the crystal coordinate of Te is (0.5+γ, 0.5+γ, 0.5+γ), the

rhombohedral distortion can be expressed as (α, γ). For pristine GeTe, α = 58.0309 and γ = 0.0223. To show how α and γ affect the band structure of GeTe, series of band structures under different α and γ values are calculated and the bands energy separation was extracted. Here, the effect of α was determined by fixing γ to 0.0223 while the effect of γ was determined by fixing α to 58.0309°, as shown in **Figure 6.2** (b) and **Figure 6.2** (c), respectively. As can be seen, increasing the value of α significantly reduced the energy separation of L and Ω bands with respect to Σ band, which could potentially boost the band degeneracy. On the other hand, the value of γ also shows strong effect on the band morphology. Reducing γ weakens the Rashba effect which merges the split Z and Ω bands. Meanwhile, reducing γ can also induces band convergence between Z and Σ bands. Therefore, there exist an optimal combination of α and γ which can potentially provide a high band degeneracy of 16 (Σ + L + Z + Ω = 6 + 3 + 1 + 6). It should be noted that the band structure calculated here neglected the interaction between α and γ, therefore, they can only be analyzed qualitatively. A more comprehensive calculation will going need to be performed to accurately predict the optimal combination of α and γ. Although the optimal value of α was experimentally identified to be 59.3° ~ 59.5° [42,121], little attention was given to the optimization of γ. In the meantime, the room-temperature structure of GeTe largely deviates from the optimal one which is why this phenomenon can only be observed near the R to C phase transition (~673K)[42]. As a result, it is almost impossible to induce such phenomenon at near-room-temperature range, as indicated in **Figure 6.2** (a).

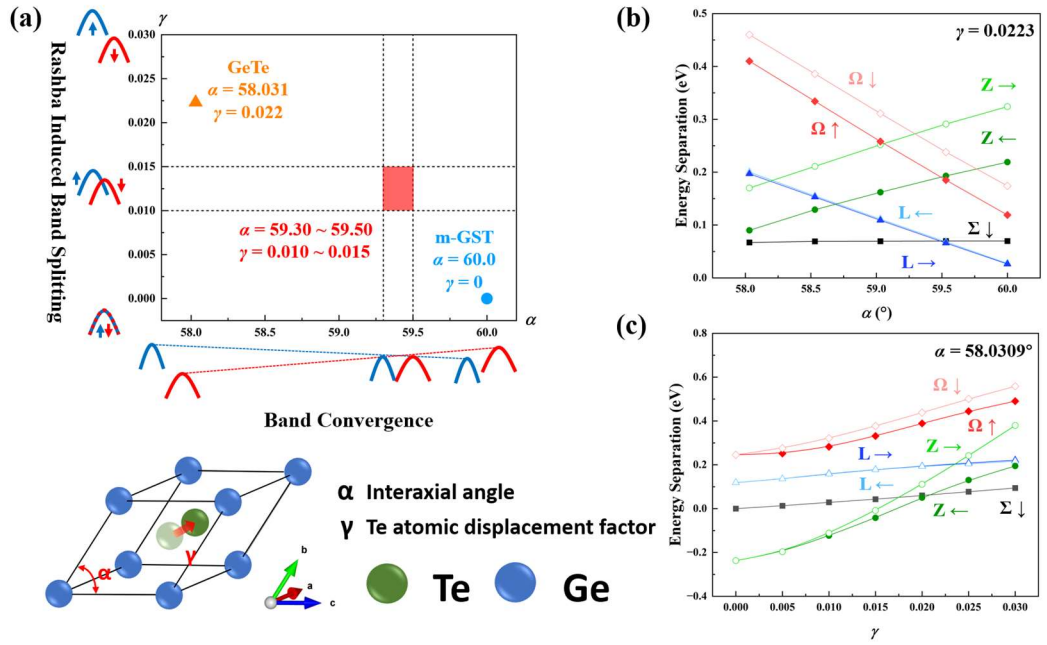

Figure 6.2. (a) Effect of the interaxial angle α and Te displacement factor γ on the band structure. Increasing α results in multiband convergence, while increasing γ enhances the Rashba effect and causes the band splitting. (b) and (c) Energy separation with respect to the top of $\Sigma\uparrow$ band as a function of α and γ, respectively. The negative value means the band is above the $\uparrow$ band.

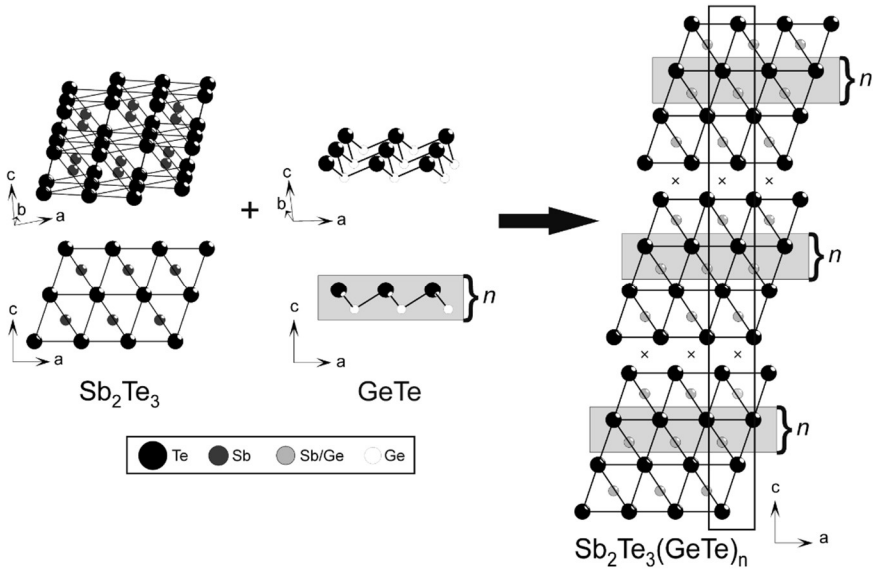

Figure 6.3. Sb_2Te_3 slabs (left) are formally enlarged by inserting GeTe-type layers in the blocks. The resulting structure (right) consists of rhombohedral-type building blocks with a thickness depending on the GeTe content n[100].

It was found that in $(GeTe)_n(Sb_2Te_3)$ (GST) alloys, the C to R phase transition type is changed from displacive phase transition into order-disorder phase transition, which induced by the cation vacancy diffusion[85,122,123]. During the order-disorder transition, the mean cation vacancy diffusion length is controlled by the content of GeTe, as indicated in **Figure 6.3**. Due to these unique features, the high temperature cubic phase could be stabilized to room-temperature by quenching a GeTe-rich GST (for simplicity, the obtained metastable GST will be named as m-GST). As a result, a crystal structure which close to the optimal one could be obtained at room-temperature. In the meantime, it was found that the crystal structure of m-GST is highly sensitive to thermal treatment and chemical composition[100,124]. By exploiting the highly tunable structure of m-GST, the transport properties in the (α, γ) space will be mapped so that an optimal combination will be

determined, and the corresponding synthetic route could be used as a reference for future thermoelectric research. Furthermore, to overcome the poor thermal stability of m-GST, a segmented device will be fabricated by combining m-GST with the conventional mid-temperature GeTe. Benefit from their similar properties, an interface-free segmented thermal leg can be synthesized via facile co-sintering method.

6.2.3 SnTe-based thermoelectric materials

In the work presented in **Chapter 5**, we qualitatively showed the contribution of the Pb substitution and Sb precipitation in reducing the lattice thermal conductivity. To gain more knowledge of the mechanism behind the reduced lattice thermal conductivity, a detailed TEM analysis will be performed to characterize the nanostructure of the samples. The average distance between the vacancy layers, density and sizes of the Sb nanoprecipitations will be directly observed. Using the Debye-Callaway model in **Section 2.4**, we can then determine the individual contributions of the above-mentioned defects to the reduction of the lattice thermal conductivity.

References

(1) Oersted. Notiz von Neuen Electrisch - Magnetischen Versuchen Des Herrn Seebeck in Berlin. *Annalen der Physik* **1823**, *73* (4), 430–432. https://doi.org/10.1002/andp.18230730410.

(2) Peltier, J. C. A. *Nouvelles Expériences Sur La Caloricité Des Courans Électriques*; 1834.

(3) Thomson, W. On a Mechanical Theory of Thermo-Electric Currents. *Proc. R. Soc. Edinb.* **1857**, *3*, 91–98. https://doi.org/10.1017/S0370164600027310.

(4) Lundstrom, M. S.; Jeong, C. *Near-Equilibrium Transport: Fundamentals and Applications*; World Scientific Publishing Company, 2012; Vol. 2.

(5) Datta, S. *Lessons from Nanoelectronics: A New Perspective on Transport—Part B: Quantum Transport*; World Scientific, 2018.

(6) Franz, R.; Wiedemann, G. Ueber die Wärme-Leitungsfähigkeit der Metalle. *Ann. Phys. Chem.* **1853**, *165* (8), 497–531. https://doi.org/10.1002/andp.18531650802.

(7) Callaway, J. Model for Lattice Thermal Conductivity at Low Temperatures. *Phys. Rev.* **1959**, *113* (4), 1046–1051. https://doi.org/10.1103/PhysRev.113.1046.

(8) Holland, M. G. Analysis of Lattice Thermal Conductivity. *Phys. Rev.* **1963**, *132* (6), 2461–2471. https://doi.org/10.1103/PhysRev.132.2461.

(9) Kim, H. S.; Liu, W.; Chen, G.; Chu, C.-W.; Ren, Z. Relationship between Thermoelectric Figure of Merit and Energy Conversion Efficiency. *Proc. Natl. Acad. Sci. U.S.A.* **2015**, *112* (27), 8205–8210. https://doi.org/10.1073/pnas.1510231112.

(10) Ioffe, A. F.; Stil'Bans, L.; Iordanishvili, E.; Stavitskaya, T.; Gelbtuch, A.; Vineyard, G. Semiconductor Thermoelements and Thermoelectric Cooling. *Physics Today* **1959**, *12* (5), 42.

(11) Giustino, F. *Materials Modelling Using Density Functional Theory: Properties and Predictions*; Oxford University Press, 2014.

(12) Slater, J. C. The Theory of Complex Spectra. *Phys. Rev.* **1929**, *34* (10), 1293–1322. https://doi.org/10.1103/PhysRev.34.1293.

(13) Slater, J. C. Note on Hartree's Method. *Phys. Rev.* **1930**, *35* (2), 210–211. https://doi.org/10.1103/PhysRev.35.210.2.

(14) Self-Consistent Field, with Exchange, for Beryllium. *Proc. R. Soc. Lond. A* **1935**, *150* (869), 9–33. https://doi.org/10.1098/rspa.1935.0085.

(15) Kittel, C. *Solid State Physics*; Shell Development Company, 1955; Vol. 3.

(16) Ashcroft, N. W.; Mermin, N. D. *Solid State Physics*; Cengage Learning, 2022.

(17) Slater, J. C. A Simplification of the Hartree-Fock Method. *Physical review* **1951**, *81* (3), 385.

(18) Perdew, J. P.; Wang, Y. Accurate and Simple Analytic Representation of the Electron-Gas Correlation Energy. *Phys. Rev. B* **1992**, *45* (23), 13244–13249. https://doi.org/10.1103/PhysRevB.45.13244.

(19) Perdew, J. P.; Burke, K.; Ernzerhof, M. Generalized Gradient Approximation Made Simple. *Phys. Rev. Lett.* **1996**, *77* (18), 3865–3868. https://doi.org/10.1103/PhysRevLett.77.3865.

(20) Hohenberg, P.; Kohn, W. Inhomogeneous Electron Gas. *Phys. Rev.* **1964**, *136* (3B), B864–B871. https://doi.org/10.1103/PhysRev.136.B864.
(21) Born, M.; Heisenberg, W. Zur Quantentheorie Der Molekeln. In *Original Scientific Papers Wissenschaftliche Originalarbeiten*; Springer, 1985; pp 216–246.
(22) Güttinger, P. Das Verhalten von Atomen Im Magnetischen Drehfeld. *Zeitschrift für Physik* **1932**, *73* (3), 169–184.
(23) Pauli, W. Principles of Wave Mechanics. *Handbuch der Physik* **1933**, *24*, 162.
(24) Hellmann, H. Einfuhrung in Die Quantenchemie. **1937**.
(25) Feynman, R. P. Forces in Molecules. *Physical review* **1939**, *56* (4), 340.
(26) Shen, J.; Chen, Z.; lin, S.; Zheng, L.; Li, W.; Pei, Y. Single Parabolic Band Behavior of Thermoelectric P-Type $CuGaTe_2$. *J. Mater. Chem. C* **2016**, *4* (1), 209–214. https://doi.org/10.1039/C5TC03325J.
(27) Gulyamov, G.; Baymatov, P. J.; Abdulazizov, B. T. Effect of Temperature and Band Nonparabolicity on Density of States of Two-Dimensional Electron Gas. *JAMP* **2016**, *04* (02), 272–278. https://doi.org/10.4236/jamp.2016.42034.
(28) Pei, Y.; LaLonde, A. D.; Wang, H.; Snyder, G. J. Low Effective Mass Leading to High Thermoelectric Performance. *Energy Environ. Sci.* **2012**, *5* (7), 7963. https://doi.org/10.1039/c2ee21536e.
(29) Zhang, H.; Liu, C.-X.; Qi, X.-L.; Dai, X.; Fang, Z.; Zhang, S.-C. Topological Insulators in Bi_2Se_3, Bi_2Te_3 and Sb_2Te_3 with a Single Dirac Cone on the Surface. *Nature Phys* **2009**, *5* (6), 438–442. https://doi.org/10.1038/nphys1270.
(30) Querales-Flores, J. D.; Aguado-Puente, P.; Dangić, Đ.; Cao, J.; Chudzinski, P.; Todorov, T. N.; Grüning, M.; Fahy, S.; Savić, I. Towards Temperature-Induced Topological Phase Transition in SnTe: A First-Principles Study. *Phys. Rev. B* **2020**, *101* (23), 235206. https://doi.org/10.1103/PhysRevB.101.235206.
(31) Muzaffar, M. U.; Zhang, S.; Cui, P.; He, J.; Zhang, Z. Antisite Defect-Enhanced Thermoelectric Performance of Topological Crystalline Insulators. *Adv. Funct. Mater.* **2020**, *30* (35), 2003162. https://doi.org/10.1002/adfm.202003162.
(32) Thesberg, M.; Kosina, H.; Neophytou, N. On the Lorenz Number of Multiband Materials. *Phys. Rev. B* **2017**, *95* (12), 125206. https://doi.org/10.1103/PhysRevB.95.125206.
(33) Debye, P. Zur Theorie Der Spezifischen Wärmen. *Annalen der Physik* **1912**, *344* (14), 789–839.
(34) Pecharsky, V. K.; Zavalij, P. Y. *Fundamentals of Powder Diffraction and Structural Characterization of Materials*; Springer US: Boston, MA, 2003.
(35) Ikeuchi K. Characterization methods for thermoelectricity. *Journal of Japanese Thermoelectric Society* **2018**, *14* (3), 154–157.
(36) Philips'Gloeilampenfabrieken, O. A Method of Measuring Specific Resistivity and Hall Effect of Discs of Arbitrary Shape. *Philips Res. Rep* **1958**, *13* (1), 1–9.
(37) Bird, R. B. Transport Phenomena. *Appl. Mech. Rev.* **2002**, *55* (1), R1–R4.
(38) Cao, J.; Tan, X. Y.; Jia, N.; Zheng, J.; Chien, S. W.; Ng, H. K.; Tan, C. K. I.; Liu, H.; Zhu, Q.; Wang, S.; Zhang, G.; Chen, K.; Li, Z.; Zhang, L.; Xu, J.; Hu, L.; Yan, Q.; Wu, J.; Suwardi, A. Designing Good Compatibility Factor in Segmented

$Bi_{0.5}Sb_{1.5}Te_3$ – GeTe Thermoelectrics for High Power Conversion Efficiency. *Nano Energy* **2022**, *96*, 107147. https://doi.org/10.1016/j.nanoen.2022.107147.

(39) Roychowdhury, S.; Samanta, M.; Perumal, S.; Biswas, K. Germanium Chalcogenide Thermoelectrics: Electronic Structure Modulation and Low Lattice Thermal Conductivity. *Chem. Mater.* **2018**, *30* (17), 5799–5813. https://doi.org/10.1021/acs.chemmater.8b02676.

(40) He, J.; Tritt, T. M. Advances in Thermoelectric Materials Research: Looking Back and Moving Forward. *Science* **2017**, *357* (6358), eaak9997. https://doi.org/10.1126/science.aak9997.

(41) Hong, M.; Zou, J.; Chen, Z. Thermoelectric GeTe with Diverse Degrees of Freedom Having Secured Superhigh Performance. *Adv. Mater.* **2019**, *31* (14), 1807071. https://doi.org/10.1002/adma.201807071.

(42) Li, J.; Zhang, X.; Chen, Z.; Lin, S.; Li, W.; Shen, J.; Witting, I. T.; Faghaninia, A.; Chen, Y.; Jain, A.; Chen, L.; Snyder, G. J.; Pei, Y. Low-Symmetry Rhombohedral GeTe Thermoelectrics. *Joule* **2018**, *2* (5), 976–987. https://doi.org/10.1016/j.joule.2018.02.016.

(43) Man, N.; Cai, J.; Guo, Z.; Liu, G.; Sun, P.; Wang, H.; Zhang, Q.; Tan, X.; Yin, Y.; Jiang, J. Thermoelectric Performance Optimization and Phase Transition of GeTe by Alloying with Orthorhombic $CuSbSe_2$. *ACS Appl. Energy Mater.* **2021**, *4* (4), 4242–4247. https://doi.org/10.1021/acsaem.1c00632.

(44) Liu, Z.; Sato, N.; Guo, Q.; Gao, W.; Mori, T. Shaping the Role of Germanium Vacancies in Germanium Telluride: Metastable Cubic Structure Stabilization, Band Structure Modification, and Stable N-Type Conduction. *NPG Asia Mater* **2020**, *12* (1), 66. https://doi.org/10.1038/s41427-020-00247-y.

(45) Zheng, Z.; Su, X.; Deng, R.; Stoumpos, C.; Xie, H.; Liu, W.; Yan, Y.; Hao, S.; Uher, C.; Wolverton, C.; Kanatzidis, M. G.; Tang, X. Rhombohedral to Cubic Conversion of GeTe via MnTe Alloying Leads to Ultralow Thermal Conductivity, Electronic Band Convergence, and High Thermoelectric Performance. *J. Am. Chem. Soc.* **2018**, *140* (7), 2673–2686. https://doi.org/10.1021/jacs.7b13611.

(46) Liu, Z.; Sun, J.; Mao, J.; Zhu, H.; Ren, W.; Zhou, J.; Wang, Z.; Singh, D. J.; Sui, J.; Chu, C.-W.; Ren, Z. Phase-Transition Temperature Suppression to Achieve Cubic GeTe and High Thermoelectric Performance by Bi and Mn Co-doping. *Proc Natl Acad Sci USA* **2018**, *115* (21), 5332–5337. https://doi.org/10.1073/pnas.1802020115.

(47) Li, J.; Zhang, C.; Feng, Y.; Zhang, C.; Li, Y.; Hu, L.; Ao, W.; Liu, F. Effects on Phase Transition and Thermoelectric Properties in the Pb-Doped GeTe-Bi_2Te_3 Alloys with Thermal Annealing. *Journal of Alloys and Compounds* **2019**, *808*, 151747. https://doi.org/10.1016/j.jallcom.2019.151747.

(48) Nshimyimana, E.; Hao, S.; Su, X.; Zhang, C.; Liu, W.; Yan, Y.; Uher, C.; Wolverton, C.; Kanatzidis, M. G.; Tang, X. Discordant Nature of Cd in GeTe Enhances Phonon Scattering and Improves Band Convergence for High Thermoelectric Performance. *J. Mater. Chem. A* **2020**, *8* (3), 1193–1204. https://doi.org/10.1039/C9TA10436D.

(49) Hong, M.; Wang, Y.; Liu, W.; Matsumura, S.; Wang, H.; Zou, J.; Chen, Z. Arrays of Planar Vacancies in Superior Thermoelectric $Ge_{1-x-y}Cd_xBi_yTe$ with Band

Convergence. *Adv. Energy Mater.* **2018**, *8* (30), 1801837. https://doi.org/10.1002/aenm.201801837.

(50) Damon, D. H.; Lubell, M. S.; Mazelsky, R. Nature of the Defects in Germanium Telluride. *Journal of Physics and Chemistry of Solids* **1967**, *28* (3), 520–522. https://doi.org/10.1016/0022-3697(67)90323-X.

(51) Guo, D.; Li, C.; Qiu, K.; Yang, Q.; Li, K.; Shao, B.; Chen, D.; Ma, Y.; Sun, J.; Cao, X.; Zeng, W.; Wang, Z.; Xie, R. The N- and p-Type Thermoelectricity Property of GeTe by First-Principles Study. *Journal of Alloys and Compounds* **2019**, *810*, 151838. https://doi.org/10.1016/j.jallcom.2019.151838.

(52) Guo, Z.; Zhang, Q.; Wang, H.; Tan, X.; Shi, F.; Xiong, C.; Man, N.; Hu, H.; Liu, G.; Jiang, J. Bi–Zn Codoping in GeTe Synergistically Enhances Band Convergence and Phonon Scattering for High Thermoelectric Performance. *J. Mater. Chem. A* **2020**, 10.1039.D0TA08700A. https://doi.org/10.1039/D0TA08700A.

(53) Tsai, Y.; Wei, P.; Chang, L.; Wang, K.; Yang, C.; Lai, Y.; Hsing, C.; Wei, C.; He, J.; Snyder, G. J.; Wu, H. Compositional Fluctuations Locked by Athermal Transformation Yielding High Thermoelectric Performance in GeTe. *Adv. Mater.* **2021**, *33* (1), 2005612. https://doi.org/10.1002/adma.202005612.

(54) Gelbstein, Y.; Ben-Yehuda, O.; Pinhas, E.; Edrei, T.; Sadia, Y.; Dashevsky, Z.; Dariel, M. P. Thermoelectric Properties of (Pb,Sn,Ge)Te-Based Alloys. *Journal of Elec Materi* **2009**, *38* (7), 1478–1482. https://doi.org/10.1007/s11664-008-0652-8.

(55) Bayikadi, K. S.; Sankar, R.; Wu, C. T.; Xia, C.; Chen, Y.; Chen, L.-C.; Chen, K.-H.; Chou, F.-C. Enhanced Thermoelectric Performance of GeTe through *in Situ* Microdomain and Ge-Vacancy Control. *J. Mater. Chem. A* **2019**, *7* (25), 15181–15189. https://doi.org/10.1039/C9TA03503F.

(56) Liu, Z.; Gao, W.; Zhang, W.; Sato, N.; Guo, Q.; Mori, T. High Power Factor and Enhanced Thermoelectric Performance in Sc and Bi Codoped GeTe: Insights into the Hidden Role of Rhombohedral Distortion Degree. *Adv. Energy Mater.* **2020**, 2002588. https://doi.org/10.1002/aenm.202002588.

(57) Wu, D.; Xie, L.; Xu, X.; He, J. High Thermoelectric Performance Achieved in GeTe–Bi_2Te_3 Pseudo-Binary via Van Der Waals Gap-Induced Hierarchical Ferroelectric Domain Structure. *Adv. Funct. Mater.* **2019**, *29* (18), 1806613. https://doi.org/10.1002/adfm.201806613.

(58) Perumal, S.; Roychowdhury, S.; Negi, D. S.; Datta, R.; Biswas, K. High Thermoelectric Performance and Enhanced Mechanical Stability of *p* -Type $Ge_{1-x}Sb_xTe$. *Chem. Mater.* **2015**, *27* (20), 7171–7178. https://doi.org/10.1021/acs.chemmater.5b03434.

(59) Back, S. Y.; Yun, J. H.; Cho, H.; Byeon, S.; Jin, H.; Rhyee, J.-S. High Thermoelectric Performance by Chemical Potential Tuning and Lattice Anharmonicity in $GeTe_{1-x}I_x$ Compounds. *Inorg. Chem. Front.* **2021**, *8* (5), 1205–1214. https://doi.org/10.1039/D0QI01281E.

(60) Jin, Y.; Xiao, Y.; Wang, D.; Huang, Z.; Qiu, Y.; Zhao, L.-D. Realizing High Thermoelectric Performance in GeTe through Optimizing Ge Vacancies and Manipulating Ge Precipitates. *ACS Appl. Energy Mater.* **2019**, *2* (10), 7594–7601. https://doi.org/10.1021/acsaem.9b01585.

(61) Perumal, S.; Roychowdhury, S.; Biswas, K. Reduction of Thermal Conductivity through Nanostructuring Enhances the Thermoelectric Figure of Merit in $Ge_{1-x}Bi_x$ Te. *Inorg. Chem. Front.* **2016**, *3* (1), 125–132. https://doi.org/10.1039/C5QI00230C.

(62) Borup, K. A.; Toberer, E. S.; Zoltan, L. D.; Nakatsukasa, G.; Errico, M.; Fleurial, J.-P.; Iversen, B. B.; Snyder, G. J. Measurement of the Electrical Resistivity and Hall Coefficient at High Temperatures. *Review of Scientific Instruments* **2012**, *83* (12), 123902. https://doi.org/10.1063/1.4770124.

(63) Giannuzzi, L. A.; Stevie, F. A. A Review of Focused Ion Beam Milling Techniques for TEM Specimen Preparation. *Micron* **1999**, *30* (3), 197–204. https://doi.org/10.1016/S0968-4328(99)00005-0.

(64) Giannozzi, P.; Baroni, S.; Bonini, N.; Calandra, M.; Car, R.; Cavazzoni, C.; Ceresoli, D.; Chiarotti, G. L.; Cococcioni, M.; Dabo, I.; Dal Corso, A.; de Gironcoli, S.; Fabris, S.; Fratesi, G.; Gebauer, R.; Gerstmann, U.; Gougoussis, C.; Kokalj, A.; Lazzeri, M.; Martin-Samos, L.; Marzari, N.; Mauri, F.; Mazzarello, R.; Paolini, S.; Pasquarello, A.; Paulatto, L.; Sbraccia, C.; Scandolo, S.; Sclauzero, G.; Seitsonen, A. P.; Smogunov, A.; Umari, P.; Wentzcovitch, R. M. QUANTUM ESPRESSO: A Modular and Open-Source Software Project for Quantum Simulations of Materials. *J. Phys.: Condens. Matter* **2009**, *21* (39), 395502. https://doi.org/10.1088/0953-8984/21/39/395502.

(65) Giannozzi, P.; Andreussi, O.; Brumme, T.; Bunau, O.; Buongiorno Nardelli, M.; Calandra, M.; Car, R.; Cavazzoni, C.; Ceresoli, D.; Cococcioni, M.; Colonna, N.; Carnimeo, I.; Dal Corso, A.; de Gironcoli, S.; Delugas, P.; DiStasio, R. A.; Ferretti, A.; Floris, A.; Fratesi, G.; Fugallo, G.; Gebauer, R.; Gerstmann, U.; Giustino, F.; Gorni, T.; Jia, J.; Kawamura, M.; Ko, H.-Y.; Kokalj, A.; Küçükbenli, E.; Lazzeri, M.; Marsili, M.; Marzari, N.; Mauri, F.; Nguyen, N. L.; Nguyen, H.-V.; Otero-de-la-Roza, A.; Paulatto, L.; Poncé, S.; Rocca, D.; Sabatini, R.; Santra, B.; Schlipf, M.; Seitsonen, A. P.; Smogunov, A.; Timrov, I.; Thonhauser, T.; Umari, P.; Vast, N.; Wu, X.; Baroni, S. Advanced Capabilities for Materials Modelling with Quantum ESPRESSO. *J. Phys.: Condens. Matter* **2017**, *29* (46), 465901. https://doi.org/10.1088/1361-648X/aa8f79.

(66) Giannozzi, P.; Baseggio, O.; Bonfà, P.; Brunato, D.; Car, R.; Carnimeo, I.; Cavazzoni, C.; de Gironcoli, S.; Delugas, P.; Ferrari Ruffino, F.; Ferretti, A.; Marzari, N.; Timrov, I.; Urru, A.; Baroni, S. Q UANTUM ESPRESSO toward the Exascale. *J. Chem. Phys.* **2020**, *152* (15), 154105. https://doi.org/10.1063/5.0005082.

(67) Dal Corso, A. Pseudopotentials Periodic Table: From H to Pu. *Computational Materials Science* **2014**, *95*, 337–350. https://doi.org/10.1016/j.commatsci.2014.07.043.

(68) Lejaeghere, K.; Bihlmayer, G.; Bjorkman, T.; Blaha, P.; Blugel, S.; Blum, V.; Caliste, D.; Castelli, I. E.; Clark, S. J.; Dal Corso, A.; de Gironcoli, S.; Deutsch, T.; Dewhurst, J. K.; Di Marco, I.; Draxl, C.; Du ak, M.; Eriksson, O.; Flores-Livas, J. A.; Garrity, K. F.; Genovese, L.; Giannozzi, P.; Giantomassi, M.; Goedecker, S.; Gonze, X.; Granas, O.; Gross, E. K. U.; Gulans, A.; Gygi, F.; Hamann, D. R.; Hasnip, P. J.; Holzwarth, N. A. W.; Iu an, D.; Jochym, D. B.; Jollet, F.; Jones, D.; Kresse, G.; Koepernik, K.; Kucukbenli, E.; Kvashnin, Y. O.; Locht, I. L. M.; Lubeck, S.;

Marsman, M.; Marzari, N.; Nitzsche, U.; Nordstrom, L.; Ozaki, T.; Paulatto, L.; Pickard, C. J.; Poelmans, W.; Probert, M. I. J.; Refson, K.; Richter, M.; Rignanese, G.-M.; Saha, S.; Scheffler, M.; Schlipf, M.; Schwarz, K.; Sharma, S.; Tavazza, F.; Thunstrom, P.; Tkatchenko, A.; Torrent, M.; Vanderbilt, D.; van Setten, M. J.; Van Speybroeck, V.; Wills, J. M.; Yates, J. R.; Zhang, G.-X.; Cottenier, S. Reproducibility in Density Functional Theory Calculations of Solids. *Science* **2016**, *351* (6280), aad3000–aad3000. https://doi.org/10.1126/science.aad3000.

(69) Prandini, G.; Marrazzo, A.; Castelli, I. E.; Mounet, N.; Marzari, N. Precision and Efficiency in Solid-State Pseudopotential Calculations. *npj Comput Mater* **2018**, *4* (1), 72. https://doi.org/10.1038/s41524-018-0127-2.

(70) Cooper, A. S. Precise Lattice Constants of Germanium, Aluminum, Gallium Arsenide, Uranium, Sulphur, Quartz and Sapphire. *Acta Cryst* **1962**, *15* (6), 578–582. https://doi.org/10.1107/S0365110X62001474.

(71) Bauer Pereira, P.; Sergueev, I.; Gorsse, S.; Dadda, J.; Müller, E.; Hermann, R. P. Lattice Dynamics and Structure of GeTe, SnTe and PbTe: Lattice Dynamics and Structure of GeTe, SnTe and PbTe. *Phys. Status Solidi B* **2013**, *250* (7), 1300–1307. https://doi.org/10.1002/pssb.201248412.

(72) Baudour, J. L. Compisitonal Dependence of Thermal Vibrations in Hg, Zn, Te Solid Solutions Determined by X-Ray Diffraction. 10.

(73) Hong, M.; Wang, Y.; Feng, T.; Sun, Q.; Xu, S.; Matsumura, S.; Pantelides, S. T.; Zou, J.; Chen, Z.-G. Strong Phonon–Phonon Interactions Securing Extraordinary Thermoelectric $Ge_{1-x}Sb_xTe$ with Zn-Alloying-Induced Band Alignment. *J. Am. Chem. Soc.* **2019**, *141* (4), 1742–1748. https://doi.org/10.1021/jacs.8b12624.

(74) Wu, D.; Zhao, L.-D.; Hao, S.; Jiang, Q.; Zheng, F.; Doak, J. W.; Wu, H.; Chi, H.; Gelbstein, Y.; Uher, C.; Wolverton, C.; Kanatzidis, M.; He, J. Origin of the High Performance in GeTe-Based Thermoelectric Materials upon Bi_2Te_3 Doping. *J. Am. Chem. Soc.* **2014**, *136* (32), 11412–11419. https://doi.org/10.1021/ja504896a.

(75) Zhang, X.; Li, J.; Wang, X.; Chen, Z.; Mao, J.; Chen, Y.; Pei, Y. Vacancy Manipulation for Thermoelectric Enhancements in GeTe Alloys. *Journal of the American Chemical Society* 6.

(76) Xu, X.; Cui, J.; Yu, Y.; Zhu, B.; Huang, Y.; Xie, L.; Wu, D.; He, J. Constructing van Der Waals Gaps in Cubic-Structured SnTe-Based Thermoelectric Materials. *Energy Environ. Sci.* **2020**, *13* (12), 5135–5142. https://doi.org/10.1039/D0EE02638G.

(77) Perumal, S.; Samanta, M.; Ghosh, T.; Shenoy, U. S.; Bohra, A. K.; Bhattacharya, S.; Singh, A.; Waghmare, U. V.; Biswas, K. Realization of High Thermoelectric Figure of Merit in GeTe by Complementary Co-Doping of Bi and In. *Joule* **2019**, *3* (10), 2565–2580. https://doi.org/10.1016/j.joule.2019.08.017.

(78) Madsen, G. K. H.; Singh, D. J. BoltzTraP. A Code for Calculating Band-Structure Dependent Quantities. *Computer Physics Communications* **2006**, *175* (1), 67–71. https://doi.org/10.1016/j.cpc.2006.03.007.

(79) Medeiros, P. V. C.; Tsirkin, S. S.; Stafström, S.; Björk, J. Unfolding Spinor Wavefunctions and Expectation Values of General Operators: Introducing the Unfolding-Density Operator. *Phys. Rev. B* **2015**, *91* (4), 041116. https://doi.org/10.1103/PhysRevB.91.041116.

(80) Medeiros, P. V. C.; Stafström, S.; Björk, J. Effects of Extrinsic and Intrinsic Perturbations on the Electronic Structure of Graphene: Retaining an Effective Primitive Cell Band Structure by Band Unfolding. *Phys. Rev. B* **2014**, *89* (4), 041407. https://doi.org/10.1103/PhysRevB.89.041407.

(81) Lee, H. S.; Kim, B.-S.; Cho, C.-W.; Oh, M.-W.; Min, B.-K.; Park, S.-D.; Lee, H.-W. Herringbone Structure in GeTe-Based Thermoelectric Materials. *Acta Materialia* **2015**, *91*, 83–90. https://doi.org/10.1016/j.actamat.2015.03.015.

(82) Wang, L.; Li, J.; Zhang, C.; Ding, T.; Xie, Y.; Li, Y.; Liu, F.; Ao, W.; Zhang, C. Discovery of Low-Temperature GeTe-Based Thermoelectric Alloys with High Performance Competing with Bi_2Te_3. *J. Mater. Chem. A* **2020**, *8* (4), 1660–1667. https://doi.org/10.1039/C9TA11901A.

(83) Xu, X.; Huang, Y.; Xie, L.; Wu, D.; Ge, Z.; He, J. Realizing Improved Thermoelectric Performance in BiI_3-Doped $Sb_2Te_3(GeTe)_{17}$ via Introducing Dual Vacancy Defects. *Chem. Mater.* **2020**, *32* (4), 1693–1701. https://doi.org/10.1021/acs.chemmater.0c00113.

(84) Chen, S.; Bai, H.; Li, J.; Pan, W.; Jiang, X.; Li, Z.; Chen, Z.; Yan, Y.; Su, X.; Wu, J.; Uher, C.; Tang, X. Vacancy-Based Defect Regulation for High Thermoelectric Performance in $Ge_9Sb_2Te_{12-x}$ Compounds. *ACS Appl. Mater. Interfaces* **2020**, *12* (17), 19664–19673. https://doi.org/10.1021/acsami.0c02155.

(85) Da Silva, J. L. F.; Walsh, A.; Lee, H. Insights into the Structure of the Stable and Metastable $(GeTe)_m(Sb_2Te_3)_n$ Compounds. *Phys. Rev. B* **2008**, *78* (22), 224111. https://doi.org/10.1103/PhysRevB.78.224111.

(86) Hÿtch, M. J.; Snoeck, E.; Kilaas, R. Quantitative Measurement of Displacement and Strain Fields from HREM Micrographs. *Ultramicroscopy* **1998**, *74* (3), 131–146. https://doi.org/10.1016/S0304-3991(98)00035-7.

(87) Jin, Y.; Hong, T.; Wang, D.; Xiao, Y.; He, W.; Gao, X.; Qiu, Y.; Zhao, L.-D. Band Structure and Microstructure Modulations Enable High Quality Factor to Elevate Thermoelectric Performance in $Ge_{0.9}Sb_{0.1}Te$-x%$FeTe_2$. *Materials Today Physics* **2021**, *20*, 100444. https://doi.org/10.1016/j.mtphys.2021.100444.

(88) Xing, T.; Zhu, C.; Song, Q.; Huang, H.; Xiao, J.; Ren, D.; Shi, M.; Qiu, P.; Shi, X.; Xu, F.; Chen, L. Ultralow Lattice Thermal Conductivity and Superhigh Thermoelectric Figure-of-Merit in (Mg, Bi) Co-Doped GeTe. *Adv. Mater.* **2021**, *33* (17), 2008773. https://doi.org/10.1002/adma.202008773.

(89) Yue, L.; Fang, T.; Zheng, S.; Cui, W.; Wu, Y.; Chang, S.; Wang, L.; Bai, P.; Zhao, H. Cu/Sb Co-doping for Tuning Carrier Concentration and Thermoelectric Performance of GeTe-Based Alloys with Ultralow Lattice Thermal Conductivity. *ACS Appl. Energy Mater.* **2019**, *2* (4), 2596–2603. https://doi.org/10.1021/acsaem.8b02213.

(90) Lou, Q.; Xu, X.; Huang, Y.; Zhu, B.; Yu, Y.; He, J. Excellent Thermoelectric Performance Realized in P-Type Pseudolayered $Sb_2Te_3(GeTe)_{12}$ via Rhenium Doping. *ACS Appl. Energy Mater.* **2020**, *3* (3), 2063–2069. https://doi.org/10.1021/acsaem.9b01915.

(91) Vankayala, R. K.; Lan, T.; Parajuli, P.; Liu, F.; Rao, R.; Yu, S. H.; Hung, T.; Lee, C.; Yano, S.; Hsing, C.; Nguyen, D.; Chen, C.; Bhattacharya, S.; Chen, K.; Ou, M.;

Rancu, O.; Rao, A. M.; Chen, Y. High *ZT* and Its Origin in Sb-doped GeTe Single Crystals. *Adv. Sci.* **2020**, *7* (24), 2002494. https://doi.org/10.1002/advs.202002494.

(92) Acharyya, P.; Roychowdhury, S.; Samanta, M.; Biswas, K. Ultralow Thermal Conductivity, Enhanced Mechanical Stability, and High Thermoelectric Performance in $(GeTe)_{1-2x}(SnSe)_x(SnS)_x$. *J. Am. Chem. Soc.* **2020**, *142* (48), 20502–20508. https://doi.org/10.1021/jacs.0c11015.

(93) Snyder, G. J.; Snyder, A. H.; Wood, M.; Gurunathan, R.; Snyder, B. H.; Niu, C. Weighted Mobility. *Adv. Mater.* **2020**, *32* (25), 2001537. https://doi.org/10.1002/adma.202001537.

(94) Rogers, L. M. Valence Band Structure of SnTe. *J. Phys. D: Appl. Phys.* **1968**, *1* (7), 845–852. https://doi.org/10.1088/0022-3727/1/7/304.

(95) Tan, G.; Shi, F.; Hao, S.; Chi, H.; Zhao, L.-D.; Uher, C.; Wolverton, C.; Dravid, V. P.; Kanatzidis, M. G. Codoping in SnTe: Enhancement of Thermoelectric Performance through Synergy of Resonance Levels and Band Convergence. *J. Am. Chem. Soc.* **2015**, *137* (15), 5100–5112. https://doi.org/10.1021/jacs.5b00837.

(96) Tan, G.; Hao, S.; Hanus, R. C.; Zhang, X.; Anand, S.; Bailey, T. P.; Rettie, A. J. E.; Su, X.; Uher, C.; Dravid, V. P.; Snyder, G. J.; Wolverton, C.; Kanatzidis, M. G. High Thermoelectric Performance in SnTe–$AgSbTe_2$ Alloys from Lattice Softening, Giant Phonon–Vacancy Scattering, and Valence Band Convergence. *ACS Energy Lett.* **2018**, *3* (3), 705–712. https://doi.org/10.1021/acsenergylett.8b00137.

(97) Pathak, R.; Sarkar, D.; Biswas, K. Enhanced Band Convergence and Ultra-Low Thermal Conductivity Lead to High Thermoelectric Performance in SnTe. *Angew. Chem.* **2021**, *133* (32), 17827–17833. https://doi.org/10.1002/ange.202105953.

(98) Xie, G.; Li, Z.; Luo, T.; Bai, H.; Sun, J.; Xiao, Y.; Zhao, L.-D.; Wu, J.; Tan, G.; Tang, X. Band Inversion Induced Multiple Electronic Valleys for High Thermoelectric Performance of SnTe with Strong Lattice Softening. *Nano Energy* **2020**, *69*, 104395. https://doi.org/10.1016/j.nanoen.2019.104395.

(99) Hong, M.; Wang, Y.; Feng, T.; Sun, Q.; Xu, S.; Matsumura, S.; Pantelides, S. T.; Zou, J.; Chen, Z.-G. Strong Phonon–Phonon Interactions Securing Extraordinary Thermoelectric $Ge_{1-x}Sb_xTe$ with Zn-Alloying-Induced Band Alignment. *J. Am. Chem. Soc.* **2019**, *141* (4), 1742–1748. https://doi.org/10.1021/jacs.8b12624.

(100) Rosenthal, T.; Schneider, M. N.; Stiewe, C.; Döblinger, M.; Oeckler, O. Real Structure and Thermoelectric Properties of GeTe-Rich Germanium Antimony Tellurides. *Chem. Mater.* **2011**, *23* (19), 4349–4356. https://doi.org/10.1021/cm201717z.

(101) Zhou, C.; Lee, Y. K.; Yu, Y.; Byun, S.; Luo, Z.-Z.; Lee, H.; Ge, B.; Lee, Y.-L.; Chen, X.; Lee, J. Y.; Cojocaru-Mirédin, O.; Chang, H.; Im, J.; Cho, S.-P.; Wuttig, M.; Dravid, V. P.; Kanatzidis, M. G.; Chung, I. Polycrystalline SnSe with a Thermoelectric Figure of Merit Greater than the Single Crystal. *Nat. Mater.* **2021**, *20* (10), 1378–1384. https://doi.org/10.1038/s41563-021-01064-6.

(102) Stoe & Cie. X-AREA (Version 1.31), X-RED32 (Version 1.28b) and X-SHAPE (Version 2.05). *Stoe & Cie, Darmstadt, Germany* **2005**.

(103) Sheldrick, G. M. SHELXT – Integrated Space-Group and Crystal-Structure Determination. *Acta Cryst A* **2015**, *71* (1), 3–8. https://doi.org/10.1107/S2053273314026370.
(104) Sheldrick, G. M. Crystal Structure Refinement with SHELXL. *Acta Cryst C* **2015**, *71* (1), 3–8. https://doi.org/10.1107/S2053229614024218.
(105) Dolomanov, O. V.; Bourhis, L. J.; Gildea, R. J.; Howard, J. a. K.; Puschmann, H. OLEX2: A Complete Structure Solution, Refinement and Analysis Program. *J Appl Cryst* **2009**, *42* (2), 339–341. https://doi.org/10.1107/S0021889808042726.
(106) Tran, F.; Blaha, P. Accurate Band Gaps of Semiconductors and Insulators with a Semilocal Exchange-Correlation Potential. *Phys. Rev. Lett.* **2009**, *102* (22), 226401. https://doi.org/10.1103/PhysRevLett.102.226401.
(107) Hunter, B. A. Rietica - a Visual Rietveld Program; Australia, 2000; p 24.
(108) Mozharivskyj, Y.; Pecharsky, A. O.; Bud'ko, S.; Miller, G. J. A Promising Thermoelectric Material: Zn_4Sb_3 or $Zn_{6-\delta}Sb_5$. Its Composition, Structure, Stability, and Polymorphs. Structure and Stability of $Zn_{1-\delta}Sb$. *Chem. Mater.* **2004**, *16* (8), 1580–1589. https://doi.org/10.1021/cm035274a.
(109) Guo, F.; Cui, B.; Liu, Y.; Meng, X.; Cao, J.; Zhang, Y.; He, R.; Liu, W.; Wu, H.; Pennycook, S. J.; Cai, W.; Sui, J. Thermoelectric SnTe with Band Convergence, Dense Dislocations, and Interstitials through Sn Self-Compensation and Mn Alloying. *Small* **2018**, *14* (37), 1802615. https://doi.org/10.1002/smll.201802615.
(110) Al Rahal Al Orabi, R.; Mecholsky, N. A.; Hwang, J.; Kim, W.; Rhyee, J.-S.; Wee, D.; Fornari, M. Band Degeneracy, Low Thermal Conductivity, and High Thermoelectric Figure of Merit in SnTe–CaTe Alloys. *Chem. Mater.* **2016**, *28* (1), 376–384. https://doi.org/10.1021/acs.chemmater.5b04365.
(111) He, W.; Li, N.; Wang, H.; Wang, G.; Wang, G.; Lu, X.; Zhou, X. Multiple Effects Promoting the Thermoelectric Performance of SnTe by Alloying with $CuSbTe_2$ and $CuBiTe_2$. *ACS Appl. Mater. Interfaces* **2021**, *13* (44), 52775–52782. https://doi.org/10.1021/acsami.1c15614.
(112) Hong, M.; Wang, Y.; Xu, S.; Shi, X.; Chen, L.; Zou, J.; Chen, Z.-G. Nanoscale Pores plus Precipitates Rendering High-Performance Thermoelectric $SnTe_{1-x}Se_x$ with Refined Band Structures. *Nano Energy* **2019**, *60*, 1–7. https://doi.org/10.1016/j.nanoen.2019.03.031.
(113) Muchtar, A. R.; Srinivasan, B.; Tonquesse, S. L.; Singh, S.; Soelami, N.; Yuliarto, B.; Berthebaud, D.; Mori, T. Physical Insights on the Lattice Softening Driven Mid-Temperature Range Thermoelectrics of Ti/Zr-Inserted SnTe—An Outlook Beyond the Horizons of Conventional Phonon Scattering and Excavation of Heikes' Equation for Estimating Carrier Properties. *Adv. Energy Mater.* **2021**, *11* (28), 2101122. https://doi.org/10.1002/aenm.202101122.
(114) Ying, P.; He, R.; Mao, J.; Zhang, Q.; Reith, H.; Sui, J.; Ren, Z.; Nielsch, K.; Schierning, G. Towards Tellurium-Free Thermoelectric Modules for Power Generation from Low-Grade Heat. *Nat Commun* **2021**, *12* (1), 1121. https://doi.org/10.1038/s41467-021-21391-1.
(115) Qin, H.; Zhu, J.; Cui, B.; Xie, L.; Wang, W.; Yin, L.; Qin, D.; Cai, W.; Zhang, Q.; Sui, J. Achieving a High Average *ZT* Value in Sb_2Te_3-Based Segmented

Thermoelectric Materials. *ACS Appl. Mater. Interfaces* **2020**, *12* (1), 945–952. https://doi.org/10.1021/acsami.9b19798.

(116) Qin, H.; Sun, S.; Liu, Y.; Yin, L.; Zhang, Y.; Sun, Y.; Xie, L.; Qin, D.; Guo, M.; Guo, F.; Qu, W.; Liu, Z.; Zhang, Q.; Cai, W.; Wu, H.; Sui, J. Constructing Multi-Type Defects in $In_{0.1}Sb_{1.9}Te_3$-(MgB_2) Composites: Simultaneously Enhancing the Thermoelectric and Mechanical Properties. *Nano Energy* **2021**, *90*, 106530. https://doi.org/10.1016/j.nanoen.2021.106530.

(117) Hazan, E.; Ben-Yehuda, O.; Madar, N.; Gelbstein, Y. Functional Graded Germanium-Lead Chalcogenide-Based Thermoelectric Module for Renewable Energy Applications. *Adv. Energy Mater.* **2015**, *5* (11), 1500272. https://doi.org/10.1002/aenm.201500272.

(118) Hedegaard, E. M. J.; Mamakhel, A. A. H.; Reardon, H.; Iversen, B. B. Functionally Graded $(PbTe)_{1-x}(SnTe)_x$ Thermoelectrics. *Chem. Mater.* **2018**, *30* (1), 280–287. https://doi.org/10.1021/acs.chemmater.7b04473.

(119) Yan, Z.; Song, K.; Xu, L.; Tan, X.; Hu, H.; Sun, P.; Liu, G.; Pan, C.; Jiang, J. Effects of Interfacial Properties on Conversion Efficiency of Bi_2Te_3-Based Segmented Thermoelectric Devices. *Appl. Phys. Lett.* **2021**, *119* (23), 233902. https://doi.org/10.1063/5.0076843.

(120) Snyder, G. J.; Ursell, T. S. Thermoelectric Efficiency and Compatibility. *Phys. Rev. Lett.* **2003**, *91* (14), 148301. https://doi.org/10.1103/PhysRevLett.91.148301.

(121) Bu, Z.; Chen, Z.; Zhang, X.; Lin, S.; Mao, J.; Li, W.; Chen, Y.; Pei, Y. Near-Room-Temperature Rhombohedral Ge1-Pb Te Thermoelectrics. *Materials Today Physics* **2020**, *15*, 100260. https://doi.org/10.1016/j.mtphys.2020.100260.

(122) Matsunaga, T.; Morita, H.; Kojima, R.; Yamada, N.; Kifune, K.; Kubota, Y.; Tabata, Y.; Kim, J.-J.; Kobata, M.; Ikenaga, E.; Kobayashi, K. Structural Characteristics of GeTe-Rich GeTe–Sb_2Te_3 Pseudobinary Metastable Crystals. *Journal of Applied Physics* **2008**, *103* (9), 093511. https://doi.org/10.1063/1.2901187.

(123) Williams, J. B.; Morelli, D. T. Understanding the Superior Thermoelectric Performance of Sb Precipitated $Ge_{17}Sb_2Te_{20}$. *J. Mater. Chem. C* **2016**, *4* (42), 10011–10017. https://doi.org/10.1039/C6TC03789E.

(124) Jost, P.; Volker, H.; Poitz, A.; Poltorak, C.; Zalden, P.; Schäfer, T.; Lange, F. R.; Schmidt, R. M.; Holländer, B.; Wirtssohn, M. R. Disorder-Induced Localization in Crystalline Pseudo-Binary GeTe–Sb2Te3 Alloys between Ge3Sb2Te6 and GeTe. *Advanced functional materials* **2015**, *25* (40), 6399–6406.